# PREPARATION AND CHARACTERISATION OF INORGANIC NANOSTRUCTURED SUPPORT MATERIALS FOR POLYMER ELECTROLYTE FUEL CELLS

**Dissertation**

Submitted in partial fulfilment of the requirements for the degree of Master of Science in Chemical Engineering


**Prepared by:**

Caelin September

**Prepared for:**

Dr Pieter B. J. Levecque

Dr Bernhard W. Schwanitz

HySA/Catalysis Centre of Competence

Department of Chemical Engineering

University of Cape Town


August 2015


The financial assistance of the National Research Foundation (NRF) towards this research is hereby acknowledged. Opinions expressed and conclusions arrived at, are those of the author and are not necessarily to be attributed to the NRF.

# PLAGIARISM DECLARATION

I know the meaning of plagiarism and declare that all the work in the document, save for that which is properly acknowledged, is my own.

Signed by candidate Signature Removed

**Caelin September**

# SYNOPSIS

Polymer electrolyte fuel cells (PEFCs) have been identified as a safe, clean and reliable alternative energy conversion technology to conventional, fossil fuel based, ones. However, the hindrance to worldwide commercialisation of this technology lies in the poor durability and high costs associated with the current carbon supported platinum (Pt/C) catalysts. Carbon support corrosion and Pt dissolution/aggregation on the catalyst layer within the fuel cell have been confirmed as the major contributors to the degradation of the Pt/C (Shao, et al., 2007). Attention needs to be paid to the improvement of catalyst components to produce an electrocatalyst with better degradation resistance and low Pt loading in order to overcome these two major commercialisation barriers. The physico-chemical and electronic interaction between the Pt catalyst and the support material play a crucial role in the catalytic activity and stability of the electrocatalysts (Wang, et al., 2011). A comprehensive understanding of the effects of catalyst support material and morphology on the mechanism and kinetics of the oxygen reduction reaction (ORR) needs to be developed.

This study investigated alternative, novel catalyst support materials and structures for the catalyst layer as opposed to carbon for PEFC applications. This material consisted of $TiB_2$ electrospun nanofibers, powder and crushed electrospun nanofibers. Methods used to reliably and accurately deposit Pt onto these materials were identified, developed and analysed. These methods include platinum deposited onto $TiB_2$ powder, electrospun crushed nanofibers and nanofiber mats via DC magnetron sputter deposition and thermally induced chemical deposition (TICD). The synthesised catalysts were physically characterised using X-ray diffraction (XRD), Transmission Electron Microscopy (TEM), Scanning Electron Microscopy (SEM) and Inductively Coupled Plasma Optical emission spectrometry (ICP-OES). Platinum effectively deposited on the $TiB_2$ support structures via these deposition techniques within two standard deviations of the desired Pt loadings.

Electrochemical characterisation techniques were identified and adapted where needed to reliably analyse the $TiB_2$ structures. These catalysts were electrochemically characterised by Cyclic Voltammetry (CV) and CO stripping to determine the electrochemical surface area (ECSA) of the catalysts. It was found that these techniques fail to correctly identify the ECSA for these inorganic materials. A CV recorded in CO was used as the baseline for the integration of $H_{upd}$ associated charges and effectively generated reproducible and consistent values for ECSA.

Rotating (ring) Disk Electrode R(R)DE analysis was used to determine the activity of these catalysts to the ORR. An interesting result was found when measuring the activity of $TiB_2$ powder materials. These materials displayed high ohmic losses as a result of its low conductivity. This issue was addressed by adding acetylene black (AB) to the support material which significantly improved its activity confirming the poor conductivity of this material. RDE results showed that the electrospun nanofiber mat displayed the highest mass specific activity of 42.0 $mA/g_{Pt}$ for 16 wt% loaded Pt/NF catalyst with AB added. Hydrogen Peroxide ($H_2O_2$) formation was found to be insignificant on these catalysts indicating a $4e^-$ reaction pathway.

Furthermore, the durability of the catalysts supported using $TiB_2$ powder, crushed nanofiber and nanofiber mats was evaluated using accelerated durability tests/protocols (ADT). Nanofiber mats displayed superior electrochemical durability when subjected to support corrosion and Pt dissolution ADTs. The rate of oxidation was 10 times less than that calculated for $TiB_2$ powder.

These findings proved that $TiB_2$ nanofiber mats, when compared to crushed nanofiber and powders, displayed overall superior electrochemical performance and durability due to their continuous fiber strands improving the morphology, Pt deposition and distribution. The inter fiber and intra fiber pores increased the electrochemical available Pt and improved ionomer dispersion in the nanofibers. This in-depth investigation into this novel material adds knowledge and insight into the preparation and characterisation of $TiB_2$ nanofibers which could assist in the improvement of the nanofiber material, its influence to enhance the catalyst layer and overall improvement to PEFC technology.

# ACKNOWLEDGMENTS

First and foremost praise and appreciations need to go to God for sparing me during this time of my postgraduate study. There is no greater gift one can get than the gift of knowledge and God has bestowed this upon me for which I am truly grateful.

I cannot explain how fortunate I feel to have had a supervisor like Dr Pieter Levecque. His support, guidance and unfailing humour lead me to not only complete my Masters project but also made that I enjoyed the experience. Thank you for never failing to believe in me and my abilities and pushing me when you felt I could do more. Your patience and approachable nature lead me to feel comfortable when dealing with issues and external stress. My growth and passion for this field is directly linked to your influence and extensive knowledge, so I sincerely thank you.

A special thank you also goes out to Dr Sharon Blair as the competence centre director for HySA/Catalysis. Thank you for always stopping to find out about my project and showing genuine interest in my development. I have nothing but respect for you and how you have developed HySA/Catalysis. I look forward in seeing the heights this group will reach.

I would like to thank Dr Bernhard Schwanitz for your assistance in my project and especially your help with writing up my thesis. Another contributor I wish to thank is Dr Shiro Tenaka for your invaluable input towards the development of the novel materials I have investigated. You were always willing to listen and assist me when I needed guidance and technical advice. I admire the way you come up with solutions which speaks volumes about your intelligence. Thank you to Nabeel Hussain for your invaluable support and advice especially through my presentation.

I had the opportunity to conduct research in Potchefstroom for two months. Within that time I was able to learn about techniques we do not have in Cape Town. For that I would like to thank Dr Cobus Kriek and Anzel Falch for your guidance and support in the time I was there.

Thank you to Miranda Waldron, Muhammed Jaffer and Innocent Shuro in the Microscopy unit at UCT as well as Hong Su in Chemistry at UCT for all my physical characterisation.

Furthermore I would not have been able to complete these past months without the support of the students in the electrocatalysis group, Archie, Colleen, Rhiyaad as well as Thulile. A special thank you is dedicated to Ntando for all your help throughout these 18 months. There were many days I was prepared to give up on EC-lab, but somehow your presence always seemed to make everything work. Thank you for supporting me throughout and looking after me in Potchefstroom.

To my friends Simone, Ayesha, Zaheera, Riddhi, Sibongile and Wesley, thank you all for being my break-away from the lab. My experience would not have been the same without you all. Most importantly I would like to thank my father, mother and sister for your unfailing words of encouragement and love throughout this journey.

The financial assistance of the National Research Foundation (NRF) towards this research is hereby acknowledged. Opinions expressed and conclusions arrived at, are those of the author and are not necessarily to be attributed to the NRF

*"When you have a great and difficult task, something perhaps almost impossible, if you only work a little at a time, every day a little, suddenly the work will finish itself."* ***Isak Dinesen***

# TABLE OF CONTENTS

# LIST OF FIGURES

# LIST OF TABLES

# NOMENCLATURE

| Symbols | Unit | Description |
|---|---|---|
| i | $mA/cm^2$ | Current Density |
| $I_d$ | $mA/cm^2$ | Diffusion limiting current density |
| $i_k$ | $mA/cm^2$ | Kinetic current density |
| $i_{k0.9}$ | $mA/cm^2$ | Kinetic current density at 0.9 V vs RHE/SHE |
| $i_{disk}$ | $mA/cm^2$ | Disk current density |
| $i_{ring}$ | $mA/cm^2$ | Ring current density |
| $i_{kmass}$ | $mA/cm^2$ | Mass specific activity |
| $i_{kspec}$ | $mA/cm^2$ | Area specific activity |
| n | - | Number of electrons |
| N | % | Collection efficiency |
| C | $mol/cm^3$ | Reactant concentration |
| D | $cm^2/s$ | Diffusion coefficient |
| $A_E$ | $cm^2$ | Area of electrode |
| $XH_2O_2$ | % | Percentage hydrogen peroxide ($H_2O_2$) formed on the ring |
| ω | rpm | Rotation speed of electrode |
| ν | $cm^2/s$ | Kinematic viscosity |
| β | - | Peak width |
| θ | radians | Bragg angle |
| K | ≈0.9 | Dimensionless crystallite shape factor |
| rf | 1.8 | Roughness factor of Pt |
| F | 96 485 C/mol | Faraday's Constant |

# GLOSSARY

| | |
|---|---|
| Ads | Adsorption |
| ADT | Accelerated Durability Test |
| CFM | Carbon Fibrous /mats |
| CNT | Carbon Nanotubes |
| CL | Catalyst Layer |
| CNF | Crushed Nanofiber |
| CV | Cyclic Voltammetry |
| DC | Direct current |
| ECSA | Electrochemical Surface Area |
| GDL | Gas Diffusion Layer |
| GC | Glassy Carbon |
| HySA | Hydrogen South Africa |
| HOR | Hydrogen Oxidation Reaction |
| LSV | Linear Sweep Voltammetry |
| MPL | Microporous Layer |
| NF | Nanofiber mat |
| NSTF | Nanostructured Thin Film |
| ORR | Oxygen Reduction Reaction |
| PAA | Poly(acrylic) acid |
| PEFC | Polymer Electrolyte Fuel Cells |
| PGM | Platinum Group Metals |

| | |
|---|---|
| PEFC | Polymer Electrolyte Membrane Fuel Cell |
| PTFE | Polytetrafluoroethylene |
| PVD | Physical Vapour Deposition |
| Pt/C | Platinum supported on Carbon |
| Pt/CNF | Platinum supported on Crushed Nanofiber |
| Pt/NF | Platinum supported on Nanofiber Mat |
| RDE | Rotating Disk Electrode |
| RRDE | Rotating Ring Disk Electrode |
| SEM | Scanning Electron Microscopy |
| SHE | Standard Hydrogen Electrode |
| TEM | Transmission Electron Microscopy |
| TGA | Thermogravimetric Analysis |
| TICD | Thermally Induced Chemical Deposition |
| Upd | Under potential deposition |
| XRD | X-ray Diffraction |

# 1. INTRODUCTION

The need to develop benign energy technologies has for years been one of the main drivers of fuel cell research and development. The South African Department of Science and Technology launched a Research and Development (R&D) strategy for hydrogen fuel cell technology in 2005. This programme is known as Hydrogen South Africa (HySA). Their aims are to diversify the economy by creating jobs through the introduction of a hydrogen fuel cell based industry in South Africa. The development of such industry poses as a viable and attractive option in South Africa since it is home to 75% of the world's known platinum reserves (The South African Agency for Science and Technology Advancement, 2010). At the same time, the platinum reserves can also alleviate socio-economic challenges by adding value to these resources through fuel cell production and capitalise on the global interest in our reserves for this technology.

A fuel cell is an electrochemical energy conversion device which converts chemical energy directly into electrical energy. Fuel cells are distinguished or classified according to the electrolyte used. The five most commonly used fuel cells include polymer electrolyte fuel cell (PEFC), alkaline fuel cells (AFC), phosphoric acid fuel cells (PAFC), molten carbonate fuel cell (MCFC) and solid oxide fuel cells (SOFC). Today PEFCs are the most popular and widely used type of fuel cells. At present, more than 80% of fuel cells produced today are PEFCs (Babir, 2012). Therefore more research has been devoted to the development of this type of fuel cell. Fuel cells are used in a number of applications both portable and stationary. This type of technology is favoured due to their lightweight, efficiency, low temperature start-up and operation, high power density, compact system design and ease in handling (Babir, 2012).

World-wide commercialisation is not yet where it should be. The two main issues influencing this is poor durability and high cost. For a fuel cell to be commercially viable it needs a lifespan of 5000 operating hours for a vehicle and greater than 40000 operating hours for a stationary system station (U.S. DRIVE, 2013). In both applications in order to be

commercially practical a fuel cell needs to retain its performance with less than 10% decay over its lifespan. However, the performance of fuel cells today shows degradation occurring within 1000 hours of operation. At the same time, the slow kinetics of the cathode oxygen reduction reaction (ORR) play a key role in limiting hydrogen fuelled PEFC performance. Therefore, improving the catalytic activity for the ORR has drawn most of the research attention in catalysis studies (Gasteiger, et al., 2005).

Carbon support corrosion has been regarded as a major contributor to the degradation of the overall PEFC catalyst layer. The scope of this investigation is the improvement of the catalyst support material and catalyst layer structure specifically. This will be addressed in twofold. Alternative support materials to carbon will be investigated according to results reviewed in literature and more specifically novel alternative support structures of this material will be investigated. The influence of nanostructuring the support material will be investigated as an improvement to the catalyst structure and furthermore its influence on the catalyst durability and activity of the catalyst layer.

# 2. REVIEW OF LITERATURE AND THEORY

In this section a critical literature review of the key aspects of this project is presented. It includes a summary of PEFC technology, an in depth look into the catalyst layer support materials, catalyst deposition methods and an overview of the fuel cell diagnostic tools that will be used in the study.

## 2.1.Polymer Electrolyte Fuel Cell (PEFC)

### 2.1.1. General Description

A fuel cell is an electrochemical device which converts stored chemical energy in fuels, such as hydrogen ($H_2$), to electrical energy in a clean and efficient way. The conversion from chemical to electrical energy occurs as a result of an electrochemical reaction. A schematic of a single fuel cell is given in Figure 1. The fuel and oxidant used as reagents in the electrochemical reaction are supplied to the cell by an external source.

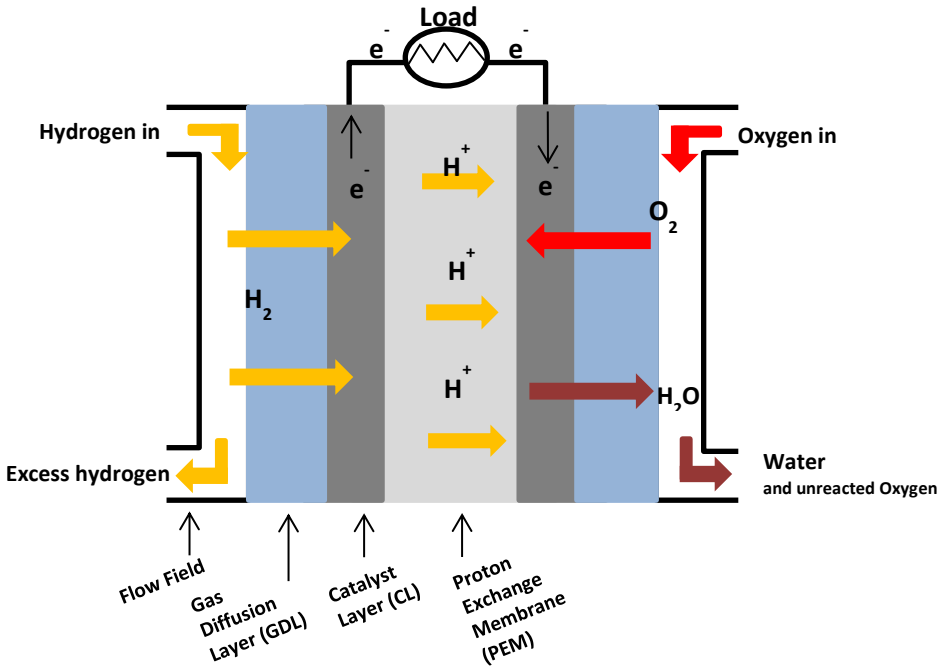


**Figure 1: Schematic illustration of a single proton exchange membrane fuel cell (Adapted from Baker & Zhang, 2011)**

Hydrogen fuel enters the fuel cell through the flow field channels on the anode side while the oxidant namely $O_2$, usually as air, is fed to the cathode side of the fuel cell. Hydrogen at the anode oxidises to form protons and electrons according to the oxidation reaction in equation 1. The electrons released in the oxidation of hydrogen are directed through an external circuit to the cathode thus generating an electrical current. The protons however, are conducted through the proton permeable membrane to the cathode.

$$H_2 \rightarrow 2H^+ + 2e^- \quad (1)$$

Simultaneously throughout the process, oxygen is reduced according to the oxygen reduction reaction (ORR) in equation 2 at the cathode. The formation of water occurs and is expelled from the system by the flow of unused oxygen (Barbir, 2006).

$$\frac{1}{2} O_2 + 2H^+ + 2e^- \rightarrow H_2O + \text{heat} \quad (2)$$

The overall reaction which takes place across the fuel cell system can be seen in equation 3.

$$H_2 + \frac{1}{2} O_2 \rightarrow H_2O \quad (3)$$

Thermodynamically, a single hydrogen fuel cell has the capacity to achieve a maximum theoretical potential of 1.23 V at 25°C and atmospheric pressure (Barbir, 2006). The efficiency of the electrochemical conversion can reach 83%. The difference between the theoretical and operating voltage is due to activation, ohmic and mass transfer losses (Baker & Zhang, 2011).

### 2.1.2. Membrane Electrode Assembly (MEA)

The heart of a PEFC is the membrane electrode assembly (MEA). The main components in the MEA are the membrane, the catalyst layer (CL) and the gas diffusion layers (GDL) seen in Figure 2.

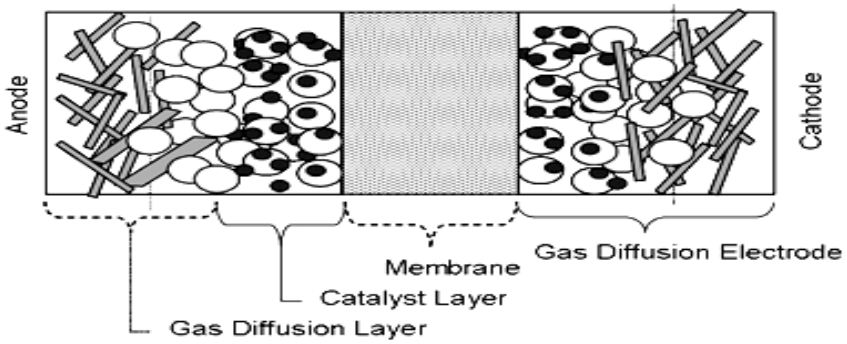


**Figure 2: MEA components (National Research Council Canada, 2010)**

The membrane in a PEFC transports protons from the anode to cathode (Zhang, 2008). The most commonly used membrane today is Nafion. This membrane is a co-polymer of tetrafluoroethylene and sulfonyl fluoride vinyl ether. The sulfonic groups in the membrane facilitate the transport of protons. The GDL also shown in Figure 2 provides an effective diffusion pathway for the reactant gas between the flow field and the catalyst layer. The GDL is also an electrical connection between the carbon supported catalyst and the current collectors. Currently the most widely used materials are carbon based porous substrates namely carbon paper or carbon cloth. The porous nature of these materials assists gas transport to the catalyst layer. The catalyst layer is where the electrochemical reactions take place. The ORR takes place at the cathode and the HOR at the anode. The best catalyst to use for these reactions, at present, is platinum since it displays the highest exchange current density for hydrogen evolution as shown in the volcano plot in Figure 3. (Zhang, 2008).

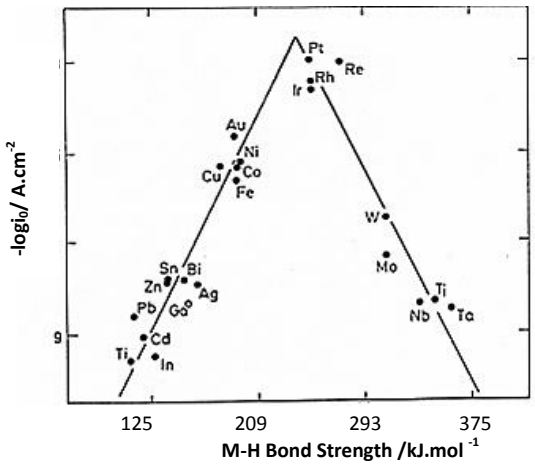


**Figure 3: Volcano plot of the electrocatalysis of the hydrogen reaction in terms of the logarithm of exchange current density (logi$_0$) for the cathodic hydrogen evolution as a function of the bonding adsorption strength (ΔE M-H) of the metal-hydrogen bond formed during the electrode reaction on various catalysts (adapted from Zhang (2008)**

### 2.1.3. The Catalyst Layer and Three Phase Boundary

As mentioned above, the catalyst layer is where the electrochemical reactions take place. Effective reaction processes require proton flow via electrolyte, supply of reactant gases via open pores and flow of electrons through the GDL. The zone in which these areas namely the open pores, electrolyte and electrocatalyst are in contact is called the Three Phase Boundary (TPB). Contact between these phases needs to be optimised in order to optimise the design of the catalyst, improve ORR and performance of the fuel cell. Figure 4 provides a schematic overview of the three phase boundary.

The sluggish kinetics of the ORR as a result of high reaction over potentials (0.3-0.4 V) results in the need for high Pt loadings on the cathode side of the fuel cell (Gasteiger, et al., 2005). Activity losses on the cathode side form a large hindrance in commercialisation of fuel cells (Shao, et al., 2007). A great deal of research is being devoted towards the development of this catalyst layer to reduce the high cost and improve its overall activity and stability. A lot of the efforts are focused on improving the catalyst support material and its structure. This will be discussed in more detail in sections to follow.

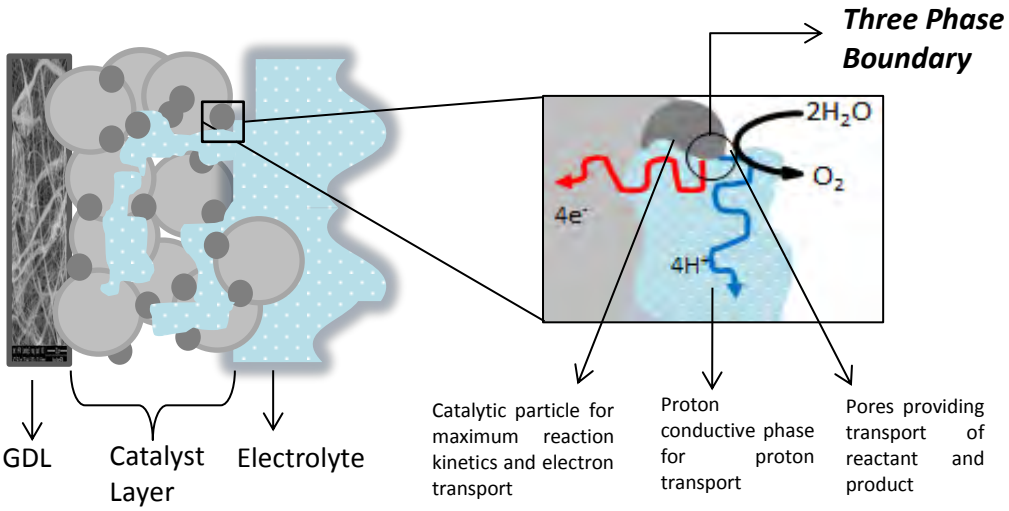


**Figure 4: Schematic overview of the three phase boundary involving the catalyst layer, electrolyte, reactant and product gases (adapted from (Bladergroen, et al., 2012)**

## 2.2. Current Pt Catalyst Support Materials

### 2.2.1. General Support Requirements

According to Dicks (2006), an ideal catalyst support for a PEFC embodies a combination of high electrical conductivity, surface area and resistance to corrosion. In addition they need to possess a pore structure able to fill with ionomer or polymer electrolyte to bring about close contact between catalyst particles and reactants therefore maximising the three-phase-boundary. The support strongly affects the electrocatalysts performance, durability and efficiency by modifying both electronic character and shape of the catalyst (Sharma & Pollet, 2012). The need for supported electrocatalysts has led to the ongoing research into various materials and structures of the support which will be further reviewed in the following chapters.

### 2.2.2. Carbon

Activated carbon, carbon black, graphite and graphitised materials have all been used as a support for various industrial catalysts. In low temperature PEFCs with hydrogen as the fuel, carbon black is currently the support material of choice to support Pt-based catalysts for both the anode and cathode.

Carbon has unique electrical and structural properties which make them ideal for fuel cell application. When compared to other typical support materials like Alumina or MgO, the most attractive features of carbon include their high electrical conductivity, reasonably acceptable stability and low cost. Carbon is a good electrical conductor because it possesses pi (π) bonds in which these π electrons are free to move. Carbon is also unique in that it can exist in various structural forms or allotropes. These structural forms include carbon black, diamond, fullerenes, carbon nanotubes and carbon fibres. Carbon black is the most widely used form of carbon as a catalyst support with nanotubes and nanofibers slowly gaining interest. These structures will be discussed in more detail in Section 2.4. The high electrical conductivity of carbon is favoured in fuel cell structures as they result in the three-phase-

boundary extending to the electrode, with the addition of the proton-conducting electrolyte (Nafion), which has a significantly positive influence on its performance.

### 2.2.3. Stability of carbon and its influence on the stability of carbon-supported catalyst

The lifetime of a PEFC is a function of operating conditions, component materials and degradation mechanisms. Performance loss in a PEFC is mainly driven by Pt catalyst degradation and carbon support corrosion. Under typical cathode operating conditions carbon black is thermodynamically unstable (Franco et al., 2008). Research shows that using highly dispersed Pt on carbon black supports in a PEFC is subject to degradation and loss of active support due to electrochemical oxidation (Dicks, 2006). Pt nanoparticles usually agglomerate or detach from carbon support resulting in a reduced electrochemical surface area (ECSA) and deterioration of the PEFC performance (Shao, et al., 2007). Figure 5 illustrates catalyst agglomeration and detachment.

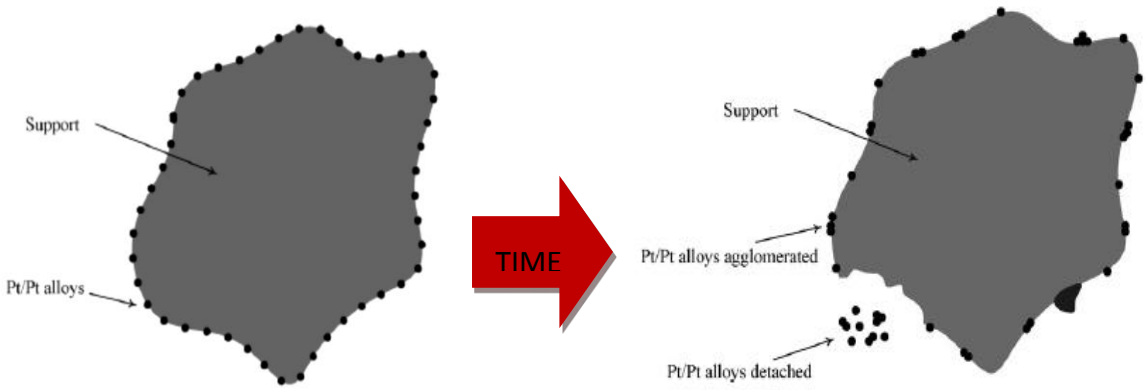


**Figure 5: Schematic representation of Pt catalyst agglomeration on and detachment from carbon support material in PEFC (Adapted from Shao *et al.* (2007)**

These phenomena occur as a result of the harsh operating conditions of a PEFC namely strong reducing $H_2$ atmosphere at the anode and strong oxidizing conditions at the cathode (Savych, et al., 2014). In addition both anode and cathode experience high temperature (80° and above), low pH (<1) and significantly high humidity which accelerate the corrosion and fuel cell degradation (Shao, et al., 2007).

The degradation mechanism of PEFC catalysts involves two aspects which influence one another. The Pt metal catalyses electrochemical oxidation of carbon and the oxidation of carbon speeds up Pt sintering. Electrochemical oxidation of the carbon support occurs along the following reaction pathway:

$$C + 2H_2O \rightarrow CO_2 + 4H^+ + 4e^- \quad (4)$$

Thermodynamically, electrochemical oxidation can occur at potentials above 0.2 V since the thermodynamic potential ($E^0$) of this reaction under standard conditions is 0.207 V (Maass, et al., 2008). Another mechanism of carbon support degradation is through the water-gas reaction in the presence of Pt. The consumption of carbon support follows this reaction pathway:

$$C + H_2O \rightarrow CO + H_2 \quad (5)$$

The presence of Pt catalyses this reaction because as Pt loading increases the greater the interfacial area between Pt and carbon becomes resulting in more carbon being exposed to the reaction. Stevens et al (2005) states that the greater the degree of graphitization of the carbon support the less the degradation will be. Another mechanism for carbon support degradation is through the presence of oxygen containing groups namely hydroxyl, phenol or carboxyl formed under oxidative conditions. These groups reduce catalyst conductivity, weaken the catalyst metal-support interaction and accelerate Pt sintering (Shao, et al., 2007)

The different modes which induce carbon corrosion include (1) fuel starvation, (2) transitioning between start-up and shutdown, (3) cold start-up at sub-zero temperatures and (4) potential control.

The most direct cause of support degradation is due to the carbon corrosion reaction given in equation 4 which occurs as a result of fuel starvation at the electrode. Fuel starvation occurs as a result of the blockage of $H_2$ from a portion of the anode. Due to the insufficient amount of fuel at the electrode necessary to produce a current, the cell potential will drop

to a value substantially below normal and drive the cell into reverse operation. During reverse operation, water electrolysis (equation 6) and carbon oxidation (equation 4) will occur to provide sufficient protons and electrons for the ORR to occur at the cathode.

$$2H_2O \rightarrow O_2 + 4H^+ \quad (6)$$

Taniguchi et al. (2004) characterized electrocatalyst degradation caused by fuel starvation using TEM, EDX and electrochemical methods. They found severe reduction in fuel cell performance and surface area loss of the electrocatalyst as a result of carbon corrosion after fuel cell reverse operation. Fuel cell reversal, as a result of fuel starvation, negatively impacts the durability of the catalyst layer by reducing the number of sites on carbon available for the catalyst as a result of corrosion. This causes metal sintering and could lead to structural collapse of the electrode (Zhang, et al., 2009).

When cycling between start-up and shutdown carbon corrosion arises from the non-uniform distribution of the fuel to the anode and the crossover of oxygen gas through the membrane (Wu, et al., 2008). Reiser et al. (2005) saw that under start-up/shutdown conditions an air/fuel boundary (also described as partial hydrogen coverage) develops at the anode causing rapid carbon corrosion (Tang, et al., 2006). This phenomenon was investigated by both Reiser et al. (2005) and Tang et al. (2006) and found to explain the reduction in anode and cathode layer thicknesses.

Degradation of PEFCs induced by carbon corrosion could also be as a result of the hazards sub-zero temperatures have on electrode durability. Start-up under sub-zero environments results in the water produced in the fuel cell to freeze instantaneously causing physical damage to the electrode structure and MEA integrity (Hishinuma, et al., 2004).

The final mode inducing carbon corrosion is potential control. Carbon corrosion is highly dependent on the potential of a cell. The highest potential a fuel cell can operate under is the open circuit voltage (OCV) of 1V or slightly lower (Zhang, et al., 2009). It was observed by Makharia et al. (2006) that carbon corrosion increased as the potential increased when exposed to potential cycles of 0.1 V to 0.96 V, 1.0 V, 1.2 V, and 1.5 V. The influence of Pt

metal on the potential at which carbon corrosion occurs was studies by (Roen, et al., 2004). They observed through cyclic voltammetry at temperatures under 50°C that when Pt was not present, carbon corrosion was suppressed up until a potential of 1.1V and higher. These results indicate carbon corrosion is accelerated in the presence of Pt metal on the carbon support material (Zhang, et al., 2009).

Stevens et al. (2005) investigated the behaviour of Pt/C catalyst at elevated temperatures under dry air conditions. The weight loss was measured and it was found that a significant loss was experienced under these conditions. TEM images confirmed that the weight loss was due to the combustion of carbon with oxygen since no Pt particles sintered or agglomerated during the exposure. Changes in the operating conditions namely thermal, as illustrated by Stevens et al. (2005), and humidity influence the stability of Pt/C catalysts. Under these conditions carbon undergoes electrochemical corrosion which, too, is exacerbated by the presence of platinum. Corrosion of carbon leads to the irreversible detachment of Pt metal which reduces the electrochemical activity of conventional Pt/C catalysts. Figure 6 below illustrates the effect of carbon corrosion on the overall support morphology and catalyst nanoparticles. This study was presented in Meier et al (2011) where they used a 20 wt.% loading of platinum supported on Vulcan XC72 support in their study.

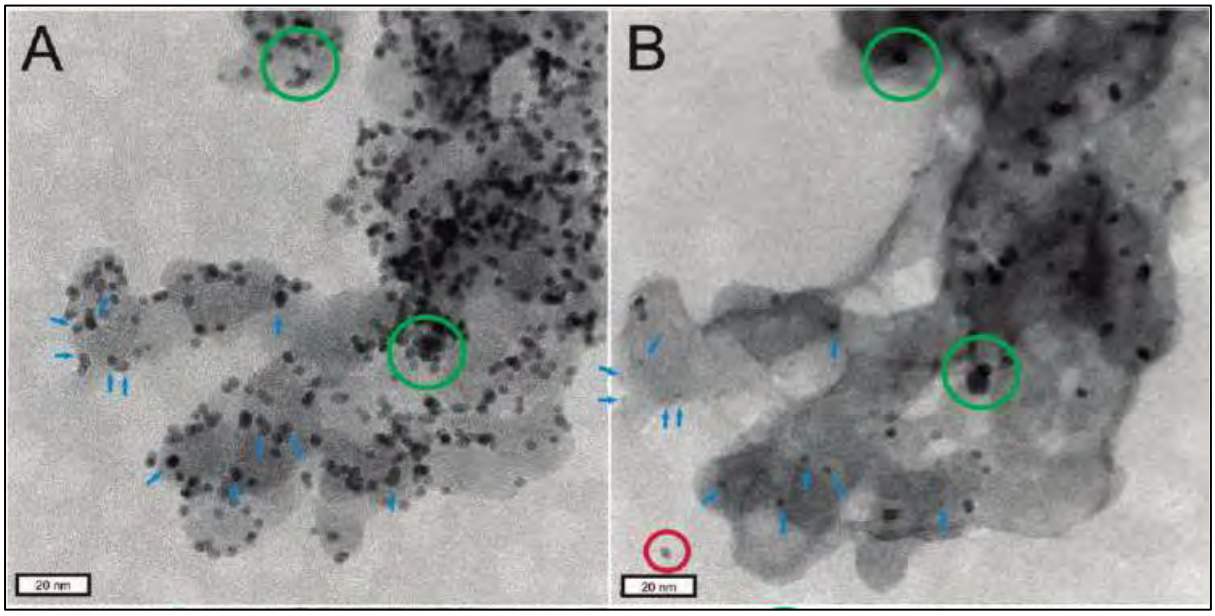


**Figure 6: Changes in catalyst layer before (A) and after 3600 cycles (B), showing detached Pt particles (red circles), reduction of Pt particle size due to dissolution (blue arrows) and agglomeration of particles (green circles) (Meier et al., 2012).**

The authors showed that severe carbon corrosion was observed after 3600 degradation cycles. This degradation led to significant changes in the support morphology and to catalyst particles detaching from the support (red circles). The green circles before and after the degradation cycles show catalyst particle agglomeration as the average size of the Pt particles increased.

The support and catalyst degradation highlighted in Figure 6 will result in catalysts not being able to maintain their structure throughout the lifespan of the fuel cell. Although carbon provides favourable characteristics, it displays severe structural limitations. Therefore alternative support materials need to be explored to improve electrochemical activity and stability of the catalysts. For the purpose of this study, focus will be paid on investigating both alternative support materials to carbon as well as alternative support structures.

## 2.3. Alternative, inorganic support materials

Numerous alternative, more stable support materials have been investigated over the years including various non-carbonaceous and inorganic oxide/carbide supports. Among these

include Ti-based compounds, tin oxides, indium tin oxide, tungsten oxide/carbides and sulphated zirconia.

However, no ceramics, besides Ti-based compounds, have yet been reported to possess good stability and, simultaneously, excellent conductivity at room temperature in acidic electrolyte (Sharma & Pollet, 2012). In an attempt to improve the activity or stability of these supports, techniques such as modification with either carbon or metals were used however failed to produce competitively stronger supports. The shortcomings of most inorganic supports are their inability to react with the metal oxide solutions i.e. inert nature.

For the purpose of this review, focus will be aimed on major reported support materials including titanium oxide, titanium nitride, titanium diboride and doped tin oxides.

### 2.3.1. Titanium Oxide ($TiO_2$)

$TiO_2$, compared to other titanium based compounds, has gained more interest as a photocatalyst due to its high efficiency, non-toxicity, stability both chemically and biologically, and low cost. $TiO_2$ exists in three crystalline forms namely anatase (tetragonal), rutile (tetragonal) and brookite (orthorhombic) (Di Paola, et al., 2013). Anatase is widely used as it is more efficient as a photocatalyst.

Research on $TiO_2$ nanoparticles as an alternative catalyst support was conducted and presented in Rajalakshmi et al. (2008). The electrocatalyst was prepared by impregnation of $TiO_2$ with chloroplatinic acid solution ($H_2PtCl_6.6H_2O$) and was then reduced with sodium borohydride ($NaBH_4$) and sodium hydroxide (NaOH) solutions. XRD showed $TiO_2$ to have the anatase structure while SEM analysis indicated a Pt loading of 17.79 wt%. Thermal gravimetric analysis (TGA) was used to study the thermal stability of these catalysts. It was found that when compared to conventional Pt/C catalysts with 20 wt% and 40 wt%, the $Pt/TiO_2$ catalyst displayed a higher thermal stability and resistance to thermal degradation. Studies into the influence of the support material on the properties of Pt catalyst were conducted by measuring the pseudo-capacitance properties and electrocatalytic activity by cyclic voltammetry (CV) experiments in an electrochemical cell (Rajalakshmi, et al., 2008).

The electrocatalytic activity of $TiO_2$ supported Pt catalysts were found to be high which, according to the authors, were as a result of the hypo-d-electronic titanium ions promoting the electrocatalytic properties of hyper-d-electronic noble platinum metal surface atoms. However, the resistance of the $Pt/TiO_2$ electrode was higher when compared to Pt/C based electrodes. It was suggested that the loss in performance in the ohmic region can be as a result of the transition of titanium oxidation state from a conducting $Ti^{2+}$ to an insulating Ti. They then concluded that although the resistance of $Pt/TiO_2$ catalysts was higher than Pt/C catalysts, they still provide higher thermal stability, electrocatalytic activity and corrosion resistance than conventional carbon supported catalysts.

$TiO_2$ supported Pt catalysts were prepared by Huang et al. (2011) for application in PEFCs in a similar manner to Rajalakshmi et al. (2008). TEM studies indicated uniformly distributed Pt nanoparticles (3-5 nm) on the $TiO_2$ surface. Both 40 and 60 wt% $Pt/TiO_2$ electrocatalyst were prepared and tested under accelerated degradation tests (ADT). It was observed that the ORR activity was ten times greater for the $Pt/TiO_2$ catalyst compared to the commercial Pt/C (45.9 wt% Tanaka TKK). $Pt/TiO_2$ displayed high durability with small voltage loss after 4000 potential cycles. Under the same tests, the Pt/C catalyst suffered corrosion losses and lost all activity after 2000 potential cycles. In studying the influence on Pt particles, no noticeable changes were seen for $Pt/TiO_2$ catalysts as opposed to a 3-fold increase in size due to agglomeration in Pt/C catalyst. Huang et al. (2011) then concluded that $Pt/TiO_2$ catalysts display a highly durable and stable alternative to Pt/C catalysts for PEFC (Huang, et al., 2011).

To address the issue of poor electron conductivity of $TiO_2$ electrocatalysts, $TiO_2$/C composite supports were incorporated into the fuel cell cathodes. Von Kraemer et al. (2008) showed that combining $TiO_2$ and carbon to form a catalyst support performed comparably to Pt/C catalysts in a PEFC. When the carbon fraction and the amount of Pt deposited on $TiO_2$ was increased, the composite electrodes possessed improved fuel cell cathode performance (Von Kraemer, et al., 2008). It was proposed that the improved performance was as a result of a permeating electron-conducting network and increased local electronic conductivity. Bauer et al. (2010) demonstrated an improved stability of Pt supported on $TiO_2$ modified

mesoporous carbon. Conventional mesoporous carbon supports coated with 20 wt% $TiO_2$ retained ~53% of the electrochemically active surface area (ECSA) compared to ~33% retained without $TiO_2$ after 1000 cycles in the potential range 0.05-1.25 V vs RHE.

Another method used to improve the poor electron conductivity involves doping the titanium oxide (TiOx, x>1) with hypervalent species such as $Sb^{5+}$ and $Nb^{5+}$ just like $SnO_2$. Pt deposited on, rutile-phase $Nb_xTi(1-x)O_2$ supports showed comparable ORR activity to conventional Pt/C electrocatalysts as a result of improved metal dispersion on the oxide along with higher durability (Huang, et al., 2010).

An issue with titanium oxides as a support material is that titanium may form oxides with homologous series $Ti_nO_{2n-1}$ ($4 \leq n \leq 10$), known as Magneli phases. $Ti_4O_7$ is the most common form and exhibits exceptional electrical conductivity <103 S $cm^{-1}$ and oxidation resistance in 1 M sulphuric acid up to 2 V vs. RHE. However, Loroi et al. (2005) found that $Pt/Ti_4O_7$ has a low mass activity compared to Pt/C.

### 2.3.2. Titanium Nitride (TiN)

When compared to carbon black, TiN, much like the other Ti-based compounds, is inert, has high electrical conductivity and mechanical hardness (Oyama, 1996). These characteristics make TiN a suitable candidate for a highly durable electrocatalyst support. Research into this material was presented by Avasarala & Haldar (2011). TiN nanoparticles were prepared and used as support for Pt nanoparticles synthesised by the polyol process. The electrochemical activity of the TiN supported Pt catalyst was evaluated and compared to that of conventional carbon black supports under fuel cell conditions. These tests showed that optimal active behaviour of Pt/TiN was observed at conditions of 0.5 M sulphuric acid ($H_2SO_4$) at 60°C. However at increasing temperatures of the $H_2SO_4$ electrolyte, faster oxynitride dissolution occurred on the surface of the TiN particles and thus increasing the direct exposure of the nitride surface to the acid solution. Formation of these positively charged corrosion products led to the adsorption of negatively charged ions present in the $H_2SO_4$ acid. As a result the TiN surface area becomes covered with a layer of negatively

charged ions making the electrode passive. This active/passive behaviour was further confirmed by accelerated durability tests performed on Pt/TiN in $H_2SO_4$ at 60°C (Avasarala & Haldar, 2011). Furthermore the formation of TiO on the TiN particles leads to a reduced conductivity of the support and as a result needs to be doped.

### 2.3.3. Titanium Diboride ($TiB_2$)

Metal diborides consist of stretched, covalently bonded boron (B) atom networks stabilized through donation of electrons from the metal atoms. The most distinctive properties of metal borides include their extremely high melting points, high hardness, and in many cases high electrical and thermal conductivities, reasonable corrosion resistance, and thermal shock resistance superior to that of oxide ceramics (Greim & Schwetz, 2006). Titanium diboride ($TiB_2$) is the most stable titanium-boron compound (Wani, et al., 2010) and is therefore considered a viable option as electrocatalyst support material owing to their high conductivity and thermal stability as well as excellent corrosion resistance in acidic media (Yin, et al., 2010).

This type of titanium based support has recently gained a great deal of interest with the first tests on these electrocatalytic support alternatives in PEFCs presented by Yin et al. (2010). $Pt/TiB_2$ catalysts were prepared via a colloid route with Nafion functional polymer stabilisation. A highly dispersed Pt loading of 18.6 wt% was achieved with an average particle size of 3.4 nm. In this study they investigated the activity of $Pt/TiB_2$ compared to commercially used Pt/C and found that the $TiB_2$ support provided 4-fold greater electrochemical stability under electrochemical oxidation cycles between the potential range 0.6-1.2 V vs RHE. Cyclic voltammetry studies revealed no oxide formation as opposed to the surface oxidation experience by carbon black. This validated the high electrochemical stability of $Pt/TiB_2$. The electrochemical surface area loss for $Pt/TiB_2$ after accelerated durability tests (ADT) shown in Figure 7 was 3.8 times slower than that of Pt/C (Yin, et al., 2010).

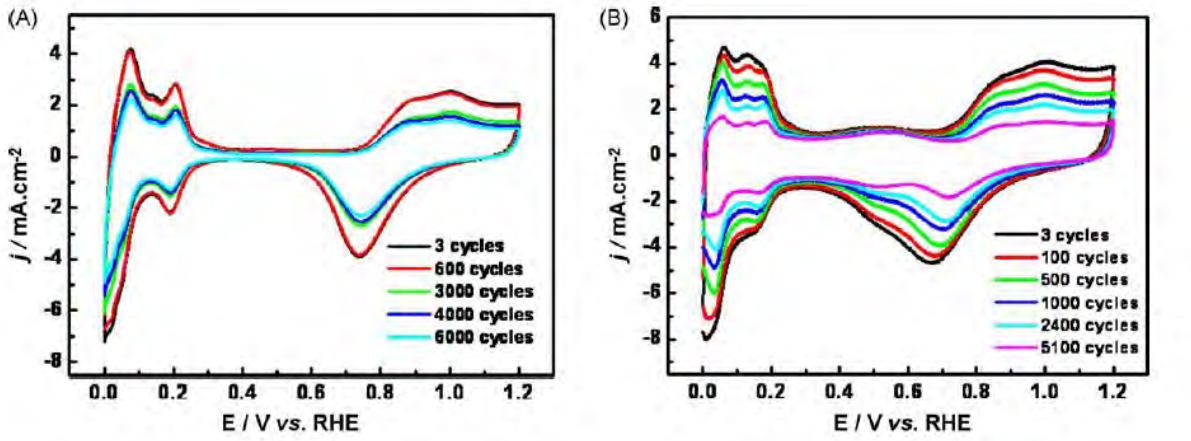


**Figure 7: Cyclic Voltammetry of $Pt/TiB_2$ (A) and commercial 20 wt% Pt/C (B) by ADT (0.5 M $H_2SO_4$, scan rate: 20 $mV.s^{-1}$, temperature: 25 °C) (Yin, et al., 2010).**

The initial ECSA of $Pt/TiB_2$ (34.7 $m^2.g^{-1}$) was lower than that of the commercial 20 wt% Pt/C (61.4$m^2.g^{-1}$). Yin et al (2010) attributed the reduced ECSA to the poor Pt utilisation efficiency on account of the larger particle size and density of $TiB_2$ compared to C supports as well as a possibility of Pt being occupied by Nafion. Further studies, however, revealed the ORR performance of $Pt/TiB_2$ catalyst in Figure 8 to be comparable to that of Pt/C catalysts. A similar conclusion was noted above for TiN supports presented in Avasarala et al. (2011) thus indicating the potential in alternative support materials towards improving the activity of Pt.

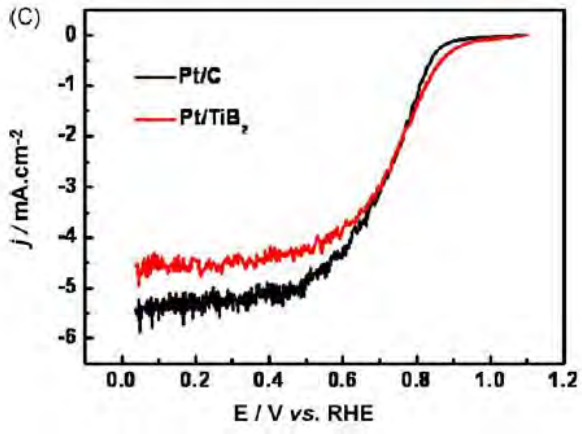


**Figure 8: Oxygen reduction reaction on the prepared $TiB_2$ and commercial 20 wt% Pt/C catalysts (Yin, et al., 2010).**

A recent study into the stability of $TiB_2$ as an alternative support material under fuel cell tests conditions was conducted by Roth et al. (2014). Model studies of $TiB_2$ in an aqueous electrochemical cell indicate that this measurement technique was not a sufficient enough measure in determining the stability of this material for fuel cell applications as $TiB_2$ rapidly oxidized in the MEA. Roth et al. (2014) synthesised the cathode using the method presented in Tin et al. (2010) and tested that in a $H_2/O_2$ PEM fuel cell. The non-oxide support converted into titanium oxide through the MEA preparation steps due to contact with Nafion at elevated temperatures. After conditioning the cell's power output declines steadily owing to the structural changes of the electrode (such as oxidation) to form sub-oxides which significantly lowers the electron conductivity compared to $TiB_2$.

### 2.3.4. Doped Tin Oxide ($SnO_2$)

Besides Ti based supports, $SnO_2$ supported catalysts have also been investigated. This transition-metal dioxide with a rutile structure is regarded as deficient n-type semi-conductor. Favourable chemical properties of this material including adsorption of OH species at low potentials, its CO tolerance and its ability to induce electronic effect with Pt has promoted this material as an effective electrocatalyst support (Sharma & Pollet, 2012). Many research groups including Okanishi et al., (2006), Matsui et al., (2006), Masao et al, (2009) ad Zhang et al., (2010) prepared Pt catalysts supported by $SnO_2$ for fuel cell application. The catalysts were heat treated at various temperatures and exposed to oxidizing or reducing environments to further understand their catalyst stability and activity. It was found that the catalytic activity towards electrochemical oxidation of CO was enhanced as a result of the microstructure and metal-support interactions. It was also reported by Masao et al., (2009) that these electrocatalysts displayed significant tolerance to potential cycling up to 1.3 V vs RHE after 10 000 cycles.

However, Nakada et al., (2007) and Kim et al., (2010) identified that there existed major issue regarding instability of these support materials and as a result it was often doped or alloyed with other metals. Lee et al., (2008) synthesised catalysts with Pt deposited on antimony doped tin oxide (Pt/ATO). The electrochemical activity and stability towards

methanol and ethanol oxidation was investigated. CO stripping experiments found the catalyst to be highly tolerant to CO. These doped tin oxide catalysts were also found to be more effective than Pt/C for electro-oxidation of both weak and strong adsorbed CO. The rough surface of this oxide support led to stronger interactions with the catalyst and higher corrosion resistance.

## 2.4. Alternative Catalyst Layer Support Structures

The hindrance in commercialisation of PEM fuel cell technology can be attributed to structural and economic issues associated with the platinum catalyst electrode. Instead of eliminating the platinum-group metal (PGM) catalysts completely or changing the catalyst support material, it has been proposed and investigated in literature that catalyst loading can be lowered by altering the morphology of the electrode. This alteration will maximise the catalyst contact with reactant gases while still maintaining the required proton and electron conduction (Zhang & Pintauro, 2011).

### 2.4.1. Nanostructured Thin Film Catalysts (NSTF)

Debe et al., (2006) emphasised the idea that by reducing the diameter of polymer fiber materials from micrometres to nanometres, several favourable characteristics arise. These characteristics include: large surface to volume ratios, flexibility in surface structure functionalities and superior mechanical performance. 3M Inc. developed a fuel cell electrode structure by replacing conventional carbon-supported dispersed Pt catalyst (Pt/C) with a nanostructured thin film (NSTF) catalyst to enhance fuel cell performance. The NSTF catalyst consists of highly-orientated platinum sputtered organic crystalline whiskers as illustrated in Figure 9. These whiskers do not contain carbon particles nor additional ionomer (Nafion) in the electrode thus resulting in a very thin electrode (< 0.3µm) seen in Figure 10. The thin nature of the electrode resulted in the mass transfer losses under pressurised $H_2$/air, leading to linear Tafel slopes for the IR-corrected polarization curve (Debe, et al., 2006). It was then concluded in Debe et al., (2006) that the NSTF catalysts provide a highly active catalyst structure with a corrosion resistant, inert support.

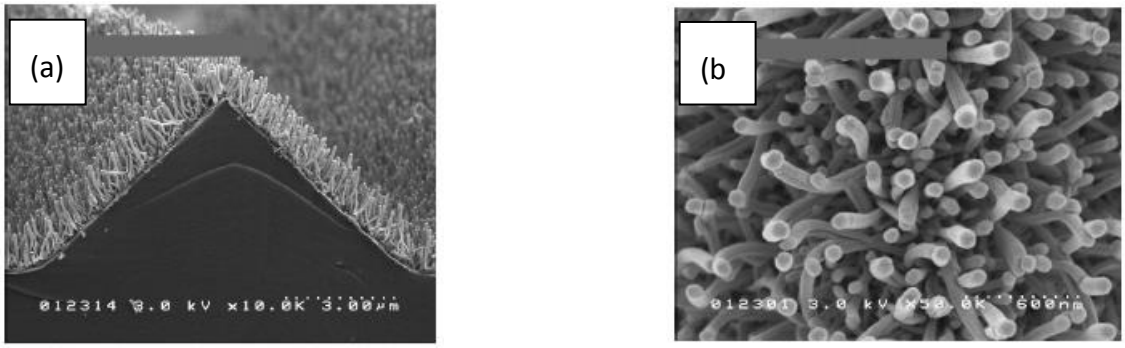


**Figure 9: Scanning electron micrograph (SEM) of NSTF catalysts as fabricated on a microstructured catalyst substrate. In (a) cross section with magnification x105 and (b) seen in plain view with magnification of x505. (Debe, et al., 2006)**

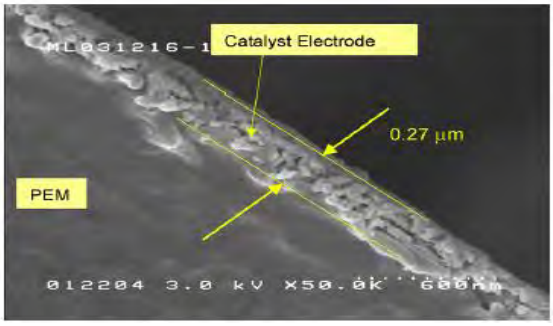


**Figure 10: SEM of the cross-sectional view of the NSTF catalyst at a magnification of x105 (Debe et al., 2006)**

Upon further research however, some operational limitations were found for the NSTF catalysts. The study by Kongkanand et al. (2012) highlighted the poor proton conduction of NSTF catalysts in PEM fuel cells under dry conditions. These catalysts required additional pre-conditioning phases before operation. Furthermore Sinha et al. (2011) compared the performance of NSTF (Pt loading 0.15 $mg_{Pt}/cm^2$) against conventional Pt/C catalysts (loading 0.4 $mg_{Pt}/cm^2$) under partially humidified conditions at 80°C. It was found that NSTF displayed comparable performance to Pt/C catalyst in wet conditions (60% inlet humidity). However, at lower humidity, poorer performance was achieved, therefore highlighting the strong dependence of the NSTF electrode's proton conductivity on relative humidity.

### 2.4.2. Platinum Nanowires

The idea of applying nanostructures to fuel cell electrodes was confirmed by the work presented in Kim et al. (2009). Their work indicated that Pt nanowire electrocatalysts used for cyclohexane fuelled PEFCs produced higher catalytic activities when compared to conventional Pt/C catalysts. The nanowire structures are illustrated in Figure 11. The nanowire catalysts of Pt with 30 nm diameters were fabricated and used as the anode electrocatalysts for the dehydrogenative oxidation of cyclohexane to benzene over the PEFC (Kim, et al., 2009). Better performances in the iE polarization curves was observed for the Pt nanowires along with greater power densities when compared to commercial nanoparticle catalysts such as Pt/C and Pt black. These results were rationalized by the enhanced electrical properties and maximised interface formation with nanowire catalysts.

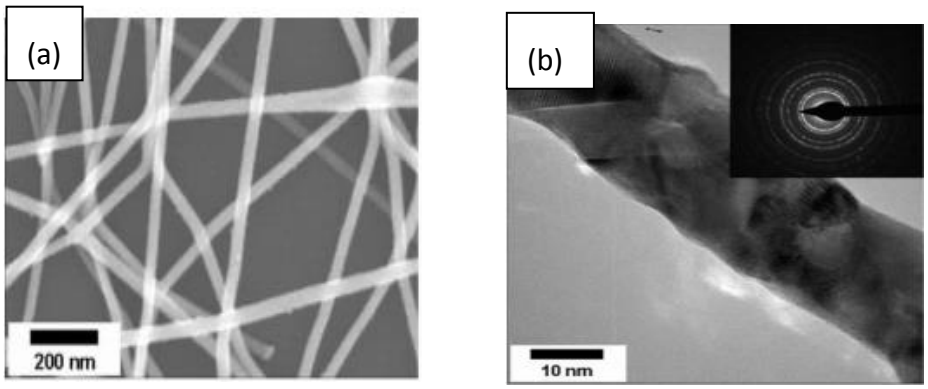


**Figure 11: (a) Field-emission scanning electron microscopy (FESEM) and (b) High-resolution transmission electron microscopy (HRTEM) of a single Pt nanowire (Kim et al., 2009)**

### 2.4.3. Nanotubes

Further research into alternative nanostructured fuel cell electrodes indicated that the use of carbon nanotubes (CNTs) as a support for catalytic materials was promising (Shao, et al., 2007). The structure of a CNT can be seen in the transmission electron microscopy (TEM) image in Figure 12. Jiang & Jiang (2011) have reported on this technology and concluded that the performance of a CNT-based MEA is superior to that of conventional metal/support MEAs. These conclusions were rationalized by the well dispersed metal nanoparticles on CNT, faster transfer of charge resulting in higher electrocatalytic activity, high surface to

volume ratio and favourable porous structure of CNTs. Yet, on the other hand the most important drawback of CNT is that the inert nature of this structure causes challenges in the attachment of the metal catalyst. Surface functionalization is required to allow for homogeneous and uniform deposition of metal nanoparticles onto the CNT which might lead to structural destruction of the CNTs (Jiang & Jiang, 2011). This is detrimental when aiming to prepare metal/CNT catalysts which are cost effective and highly efficient.

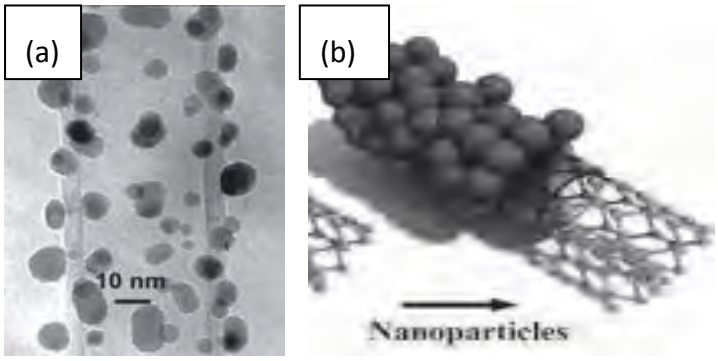


**Figure 12: (a) Transmission electron microscopy (TEM) of Pt nano-particles deposited on a CNT (b) Schematic illustration of CNT surface functionalisation including Pt nanoparticles deposition. (Jiang & Jiang, 2011)**

Several research groups (Wang, et al., 2006) (Li, et al., 2002) (Su, et al., 2010) ( Xuyen, et al., 2009)) have concluded that CNT are more resistant to electrochemical oxidation than carbon black. They suggest that this is due to the higher durability and the specific interaction between Pt nanoparticles and the CNT support.

### 2.4.4. Electrospun Nanofiber Applications

The fabricated nanostructured electrodes which include the three previously explained examples, however, do not lead to substantial reduction in Pt catalyst loading for the cathode while still maintaining maximum fuel cell power output and long-term electrode durability.

Recently electrospinning techniques, used to manufacture nanoscale polymer fiber structures, have been recognised as a potential method to create nanostructured fuel cell electrodes. Electrospinning is a low cost method of producing nanofibers by charging a viscous liquid in a syringe and discharging it onto a collector. If a high enough voltage is

applied the liquid is drawn into a jet, depositing fibers on the grounded collector (Fang et al. 2011).

Zhang & Pintauro (2011) successfully fabricated a nanofiber mat electrode (illustrated in Figure 13) by electrospinning a solution containing Pt/C catalyst powder (40 wt% Pt on carbon black) in an isopropyl alcohol/water solvent containing dissolved Nafion, used as the ionomer component, and poly(acrylic) acid (PAA), selected as the carrier component to provide sufficient chain entanglements required for effective nanofiber electrospinning. The nanofiber mat electrode was used as the cathode in the membrane electrode assembly (MEA) of a $H_2$/air fuel cell and was observed to perform superior to that of a decal cathode MEA. The experimental procedure used to fabricate this mat is illustrated in Figure 13.

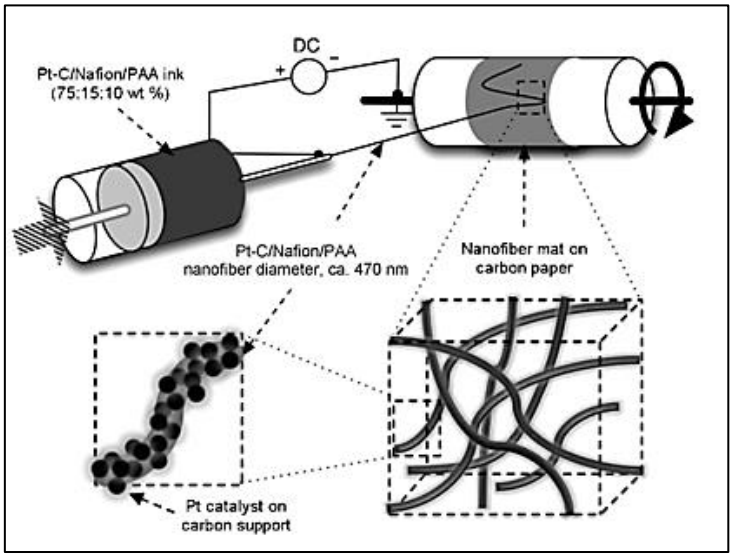


**Figure 13: Experimental design for electrospinning a nanofiber catalyst mat. A network of Pt/C particles is contained within a nanofiber by a proton conducting polymer binder. The nanofibers are collected as a mat on the collector drum. (Zhang & Pintauro, 2011)**

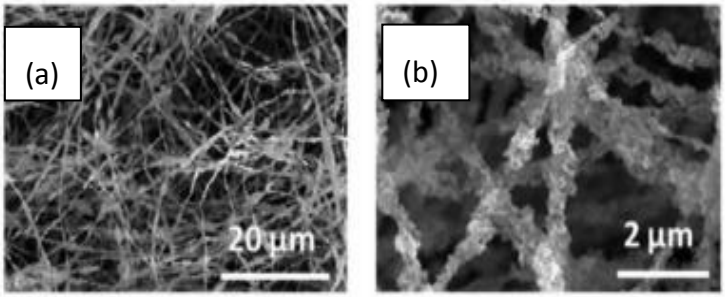


**Figure 14: Low and high magnification SEM images (a,b) of electrospun Pt-C/Nafion/PAA nanofibers. (Zhang &Pintauro, 2011)**

By means of polarisation curve evaluation seen in Figure 15, it was observed that the electrospun nanofiber cathode MEA with a Pt loading of 0.1 $mg_{Pt}/cm^2$ produced a comparable current density (873 $mA/cm^2$) and power density (524 $mW/cm^2$) when compared to the decal cathode MEA with a Pt loading of 0.4 $mg/cm^2$ (Zhang & Pintauro, 2011). The electrochemical surface area (ECSA) of the electrospun nanofiber cathode MEA was found to be 114 $m^2/g_{Pt}$ whereas the decal cathode MEA had an ECSA of 60 $m^2/g_{Pt}$. It was also noted that the mass activity at 0.9V of the electrospun nanofiber electrode was $0.23A/mg_{Pt}$ which was twice as large as the mass activity found for the decal electrode (Zhang & Pintauro, 2011). The authors concluded that the higher ECSA and mass activity attained by the electrospun nanofiber cathode were attributed to a more uniform distribution of Pt/C particles and Nafion polymer in the nanofiber mat which provided better proton transport and oxygen diffusion to the catalyst layer. Zhang and Pintauro (2011) also found that in an accelerated voltage cycling durability test, electrospun Pt-C/Nafion/PAA cathodes exhibited less degradation than decal Pt/C-Nafion cathodes.

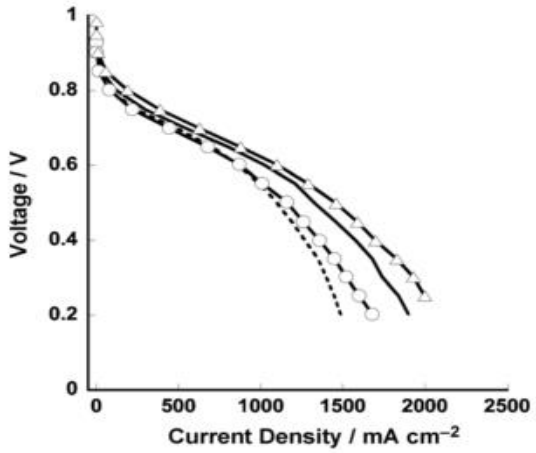


| | Pt loading ($mg/cm^2$) |
|---|---|
| ES01 | 0.1 |
| ES02 | 0.2 |
| ES04 | 0.4 |
| Decal | 0.4 |

(○: ES01, ——: ES02, and △: ES04)

(- - - - Decal04).

**Figure 15: Polarisation curves for a $H_2$/air fuel cell employing MEAs with electrospun and decal cathodes.**

The results presented by above were later extended by the same group (Brodt et al., 2013). The superior performance observed when replacing conventional decal cathode MEAs with electrospun nanofiber cathode MEAs in PEM fuel cells was verified. Brodt et al., (2013), extended the original reports by investigating the effects of fuel cell temperature, pressure and feed gas flow rates on the electrospun nanofiber cathode MEA's performance and compared that to conventional decal cathode MEAs. The results indicated a significant performance increase with electrospun cathodes generating 360 $mW/cm^2$ as opposed to 280 $mW/cm^2$ for the decal cathode. The best performing MEA with cathode loading of 0.055 $mg_{Pt}/cm^2$ and anode loading of 0.059 $mg/cm^2$ tested at 80°C with a 100% humidified air inlet flow of 200 sccm at 3 atm produced 906 $mW/cm^2$ power. Figure 16 shows the resultant nanofiber mats fabricated in these tests.

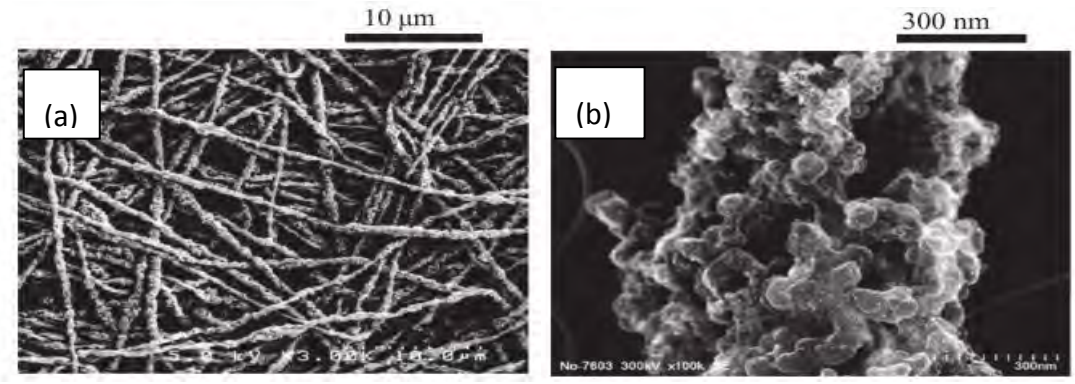


**Figure 16: a) 3000x SEM image of electrospun nanofiber mat b) 100000x SEM image of an electrospun Pt-C/Nafion/PAA nanofiber (Brodt et al., 2013)**

Catalytic electrodes fabricated from electrospun nanofibers have been applied, not only to $H_2$/air fuel cells, but also to alkaline fuel cells and direct methanol fuel cells (DMFC). Li et al., (2008) successfully fabricated Pt/carbon fibrous mats (CFM) for application in direct methanol fuel cells. This was done by thermally treating electrospun polyacrylonitrile fibers to produce the CFM and electrodepositing platinum clusters onto these CFMs by multi-cycle CV methods. The catalytic peak current of methanol oxidation on commercial catalysts (185 $mA/mg_{Pt}$) was compared to that of the Pt/CFM electrodes (420 mA/mgPt) and it was concluded that Pt supported on CFMs exhibit high performance in terms of electrocatalytic activity and stability towards methanol oxidation. The result confirmed that carbon fibrous mats are favourable alternative supporting materials to improve catalyst performance (Li, et al., 2008).

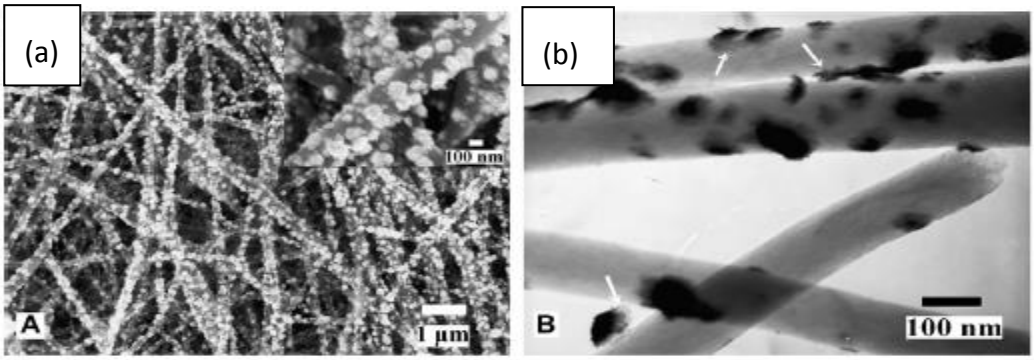


**Figure 17: a) The SEM image of a prepared Pt/CFM electrode and b) the TEM image of the same electrode (Li et al., 2008)**

### 2.4.5. Electrospun Inorganic Nanofibers as Catalyst Supports

$TiO_2$ supported electrocatalysts have displayed poor electrical conductivity in PEM fuel cells as discussed in Section 2.3.1. In order to successfully implement $TiO_2$ as a viable alternative support material there needs to be a clear improvement in the electrical catalyst activity of Pt nanoparticles/$TiO_2$ catalysts. This can be achieved by improving the dispersion of Pt on $TiO_2$ support materials (Long, et al., 2011). As discussed in Section 2.4.1, Debe et al. (2006) proved that nanostructuring of the support material introduced favourable characteristics between the metal catalysts and support materials. Therefore alternative structuring of the $TiO_2$ support materials have been investigated to improve the interaction between metal catalysts, electrical conductivity, Pt dispersion and Pt utilisation.

Savych et al. (2014) recently presented an investigation on the effects of non-carbon nanostructured support materials on the stability of Pt nanoparticles for PEFCs. They investigated both changing the morphology of the support structure and replacing the carbon with alternative support materials. This lead to the replacement of carbon black catalyst support structures with both electrospun carbon nanofibers and Nb-doped $TiO_2$ nanofibers as the electrocatalyst support. Earlier research presented by Chhina et al. (2009), Huang et al. (2010) and Chevallier et al. (2012) concluded that $TiO_2$ displayed ORR activity comparable to that of Pt/C catalysts but with greater stability and activity retention compared to Pt/C. Therefore $TiO_2$ is a promising alternative support material to carbon. A challenge encountered using semi-conducting oxides as a support material was to enhance the electronic conductivity to match that of carbon. They found that by doping with donor-type ions $Nb^{5+}$ to modify the electrical structure and improve its electron transport properties.

Savych et al. (2014) synthesised the platinum nanoparticles by the microwave polyol method and deposited it on the fibrous electrospun supports. Through both physical and electrochemical characterisation they concluded that titanium dioxide based material has a smaller corrosion charge (as can be seen in Figure 18) and thus higher electrochemical stability than both carbon nanofibers and carbon black at high potential. The enhanced

corrosion resistance of the TNF support was speculated to be ascribed to the high chemical and electrochemical stability of the ceramic material and to the support-metal interaction experienced between Pt and $TiO_2$.

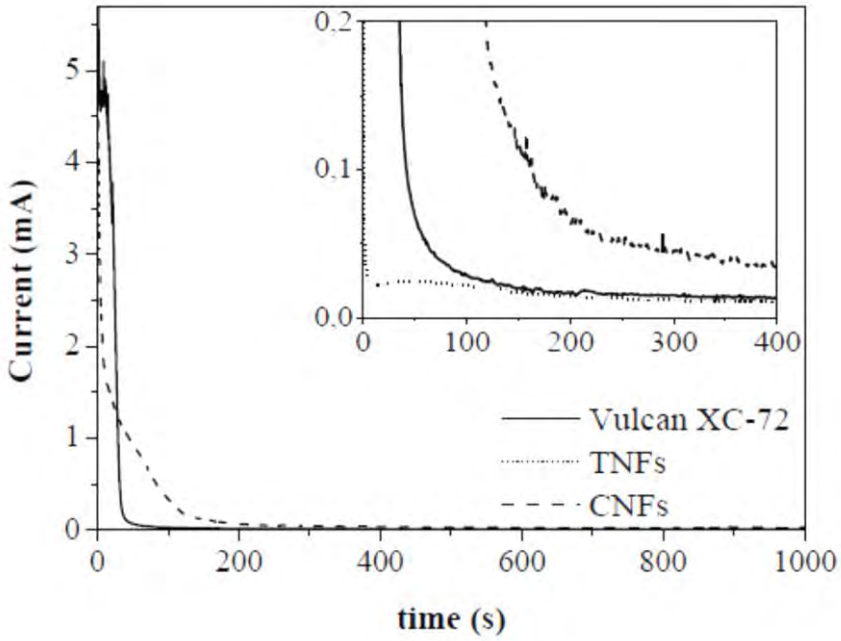


**Figure 18: Oxidation characteristics of electrospun carbon (CNF), titanium dioxide nanofibers (TNFs) and Vulcan XC-72R at 1.4V vs RHE** (Savych, et al., 2014)

## 2.5.Pt Catalyst Deposition Methods

### 2.5.1. Overview

Catalysts exist in different forms and the preparation of these requires different protocols to achieve the desired properties of the final catalyst. In this study the goal in catalyst preparation is to produce and reproduce a stable, active and selective catalyst to be applied in a fuel cell system. This is typically achieved by depositing Pt on a high surface area support (which has been discussed in preceding sections).

Supported metal catalysts are usually prepared from metal salts and porous supports along the routes including impregnation of support with an aqueous solution of metal salts. Although usually straightforward, wet chemical methods do include filtration and washing steps and sometimes produce non-uniform materials (Gates, 2008). Although this method of catalyst metal deposition is widely used, it will not be applied in this study as it involved vigorous treatment of the support materials and this would damage the brittle support materials under investigation.

The discussion to follow will provide catalyst preparation procedures particularly pertaining to the technology available and applied in this study. The material used in this study are fragile and costly therefore the physical and vapour deposition techniques chosen were based on their availability and intrinsic advantages and disadvantages for this specific project. TICD and sputtering of PEFC electrodes seems attractive, because they are dry processes where the Pt loading is easily adjusted by metal precursors in TICD or the sputter parameters (time, power *etc*.) (Schwanitz, et al., 2012).

### 2.5.2. DC Magnetron Sputter Deposition

This physical vapour deposition (PVD) method has become one of the most common ways of depositing thin films (Micro Magnetics, 2013) and are frequently applied to create Pt based catalysts (Bock, et al., 2008). It has a variety of applications in industry today namely

semiconductors, disk drives, CDs and optical device industries. Sputter deposition involves generating plasma between the substrate (surface onto which the metal film deposits) and the target (source material that is to be deposited) through the bombardment of the target by high energy particles. The target emits atoms to the substrate. The emitted atoms then condense on the substrate under high vacuum environments. This deposition technique is a dry technique which permits an accurate and reliable deposition of materials on an atomic scale. Figure 19 shows a schematic of the basic sputtering process and mechanism.

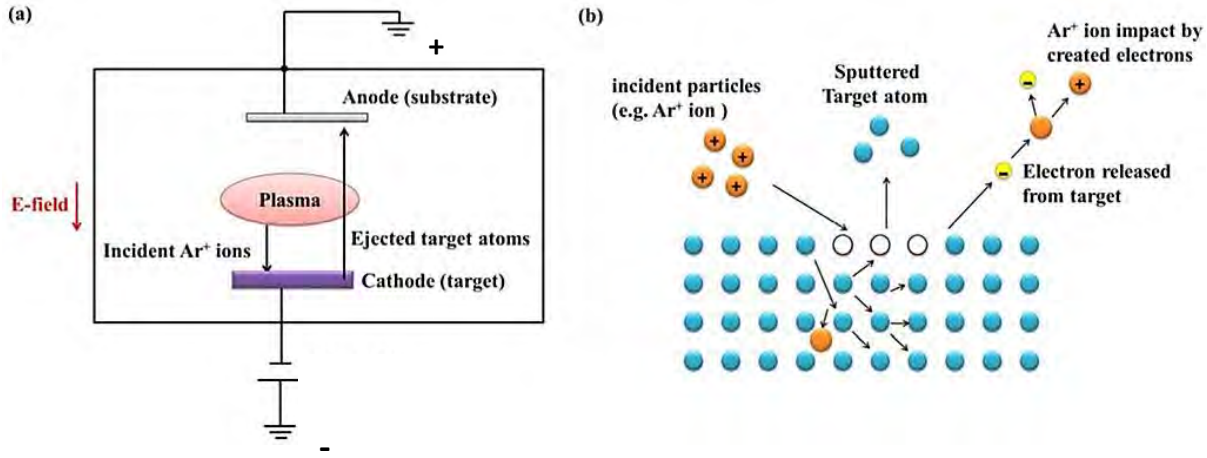


**Figure 19: Schematic diagram of the basic sputtering system (a) and sputtering mechanism (b). (Wang, et al., 2014)**

Sputter deposition has been researched as a means to reduce catalyst loadings by improving catalyst utilisation with minimum loadings while maintaining proton access and electronic contunuity (Alvisi, et al., 2005). Sputter deposition used to deposit Pt onto uncatalysed GDEs have proved to allow control over Pt cluster size and ensure a uniform distribution of nanosized Pt clusters on the support surface (Alvisi, et al., 2005). The advantages of sputter deposition include:

1. Easy preparation of the catalyst (no pre or post treatment is necessary)

2. Ultra low Pt loading allowing for cost reduction of the fuel cell

3. Easy industrial transfer of the process for the fabrication of uniform and reproducible catalyst layers since sputter deposition is already a commercial thin film deposition technique (Alvisi, et al., 2005).

#### *2.5.2.1. Magnetron Sputter Deposition for Cathode Preparation*

Magnetron sputter deposition has in recent years gained interest in the fields of electrocatalysis and as a viable catalyst preparation method for PEFC applicaions. Experimental data reported have shown that sputter parameters including dc or rf power, gas flow, partial pressure, temperature, distance between the target and substrate, etc. can modify film composition, structure and morphology. These parameters directly affect the specific surface and electrochemical reactivity of the electrocatalyst (Slavcheva, et al., 2009). A parametric study of sputtered Pt was conducted via surface analysis and electrochemical behaviour and activity towards ORR. It was found that a highly efficeint catalyst was achieved at the optimal sputter parameters of 68 mTorr pressure, 100 W DC power and film thickness of 120-130 nm.

In Schwanitz et al., (2012) the performance of sputtered and ink based electrodes of different platinum loadings were compared. A significantly reduced Pt loading of 100 $\mu g/cm^2$ was achieved using sputter deposition however suffered performance losses as a result. The sputtered electrodes could achieve relatively high current densities of 0.46 $A/cm^2$ at 0.6V. Electrochemical analysis of sputtered Pt on carbon electrodes for various platinum loadings was conducted and the results are illustrated in Figure 20. These results indicate that care needs to be taken when calculating ECSA for loadings lower than 10 $\mu g/cm^2$. The total charge under the CV is dominated by the double layer charging of the carbon support.

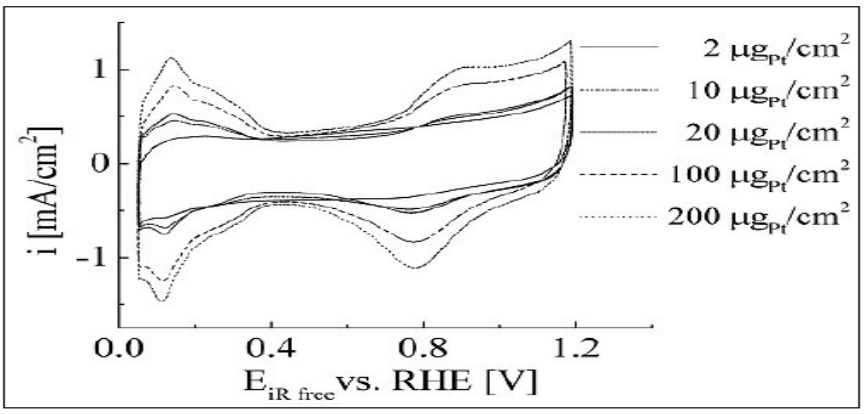


**Figure 20: Cyclic voltammetry for sputtered electrodes with Pt loadings from 2-200μg/cm$^2$ in Ar saturated 0.1 M $HClO_4$ solution. Sweep rate 50 mV/s at room temperature and ambient pressure. (Schwanitz, et al., 2012)**

### 2.5.3. Thermally Induced Chemical Deposition (TICD)

Thermally Induced Chemical Deposition (TICD) is a chemical vapour deposition method used to deposit a metallic film on a substrate surface. TICD utilises metal-organic precursors which allows this method to deposit pure metal particles at lower temperatures (<150°C) (Hierso, et al., 1998). The principle behind the TICD process involves forming a liquid of metal-containing precursor, known as an organometallic complex. This complex thermally decomposes and deposit onto a substrate layer forming a metal film (Thurier & Doppelt, 2008).

#### *2.5.3.1. TICD vs Wet chemistry*

The choice of a metal deposition method to use lies in the properties of the product one desires to achieve. TICD has many advantages over wet chemistry as this technique avoids lengthy synthesis steps such as impregnation, washing, drying and calcination. TICD technique is also conducted in a closed system therefore the surface is protected from poisoning and material transformations during the drying stages required when using wet chemistry. TICD is fast and economic because it eliminates time consuming stages when compared to wet chemistry methods (Thurier & Doppelt, 2008).

#### *2.5.3.2. Main components and their requirements*

In order to form a highly dispersed, reproducible thin film via TICD, the volatility of the precursor compound is of great importance. The method is performed at the pressure and temperature conditions needed for the compound to pushed beyond its stability range, decomposing the organometallic species and forming the metallic particles. According to Thurier & Doppelt (2008) the ideal precursor needs to possess the following characteristics:

1. High volatility
2. Adequate thermal stability range
3. Low toxicity
4. Fast nucleation and low handling risk
5. Stability towards oxygen and moisture
6. Low production cost

For the purpose of application in fuel cells, organometallic platinum compounds have been investigated as precursors. These complexes contain platinum and organic ligands. The most widely used platinum precursors include $Pt(acac)_2$, $Pt(PF_3)_4$, $(cod)PtMe_2$, $MeCpPtMe_3$ or $EtCpPtMe_3$ (Doppelt & Thurier, 2011). These precursors have the following structural formulae:

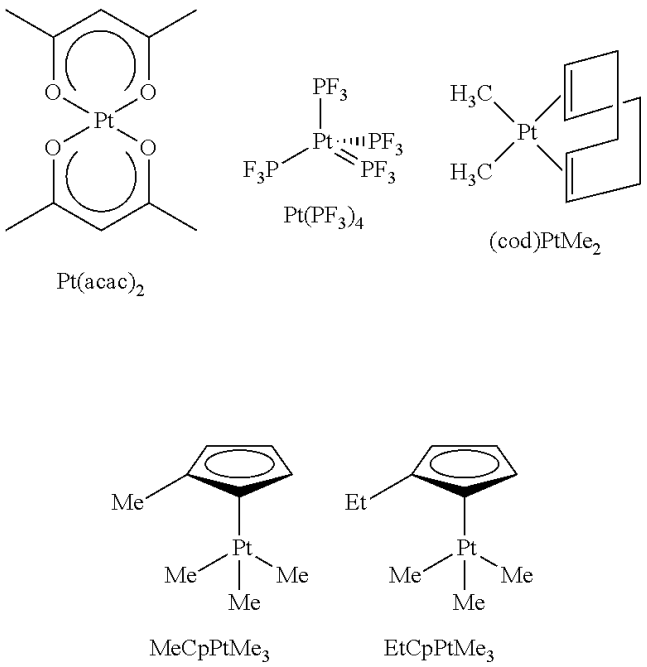


**Figure 21: Structural formulae of widely used platinum precursors(Doppelt & Thurier, 2011)**

Studies have indicated that $Pt(acac)_2$, although the ligand may decompose without metal deco-ordination resulting in an impure film, is still the preferred precursor. $Pt(PF_3)_4$ leads to a deposit containing fluorine which is undesired in fuel cells (Martin, et al., 2005), $(cod)PtMe_2$ has moderate volatility while -$CpPtMe_3$, -$MeCpPtMe_3$ and -$EtCpPtMe_3$ are sensitive to air and moisture, and are not cost effective to be applied in fuel cell technology (Doppelt & Thurier, 2011).

## 2.6.Electrochemical diagnostic techniques

Electrochemical diagnostic techniques all involve the use of electricity as either an input or an output signal. The instruments used for electrochemical techniques will measure the output electrical signal corresponding to a generated input electrical signal. The three fundamental electrochemical signals are voltage (V), current (i) and time (t). The input signal will cause an electrochemical reaction to occur at the working and counter electrodes. The amplitude of the input signal will control the rate of the reactions which is represented by the amplitude of the output signal (Barbir, 2013).

### 2.6.1. Cyclic Voltammetry (CV)

Voltammetry studies the resultant current (I) as a function of an applied potential (E). Cyclic voltammetry refers to cycling or sweeping the input potential on the working electrode between two limits and recording the current response in that potential region (Qui, 2008). The potential is swept linearly between the two limits. As the potential is swept forward towards the positive potential region it will become high enough to cause oxidation of the electrochemically active species which will result in an anodic current to appear. As the potential goes higher, the anodic current will increase as a result of the reaction kinetics speeding up. The point where all the reduced form of the electrochemically active species at the electrode is consumed is where the highest anodic current will appear and an anodic peak will form. After that point, the current will decrease as a result of mass transport limitations. When the potential reaches the set high limit, the scan reverses and scans towards the lower limit. Reduction will occur on the reverse sweep causing a negative, cathodic current. The cathodic peak occurs at a slightly lower potential than the anodic peak (Qui, 2008).These peaks are indicative of the potentials at which electrochemical reactions occur. An example of a Pt electrode cyclic voltammogram can be seen in Figure 22 below.

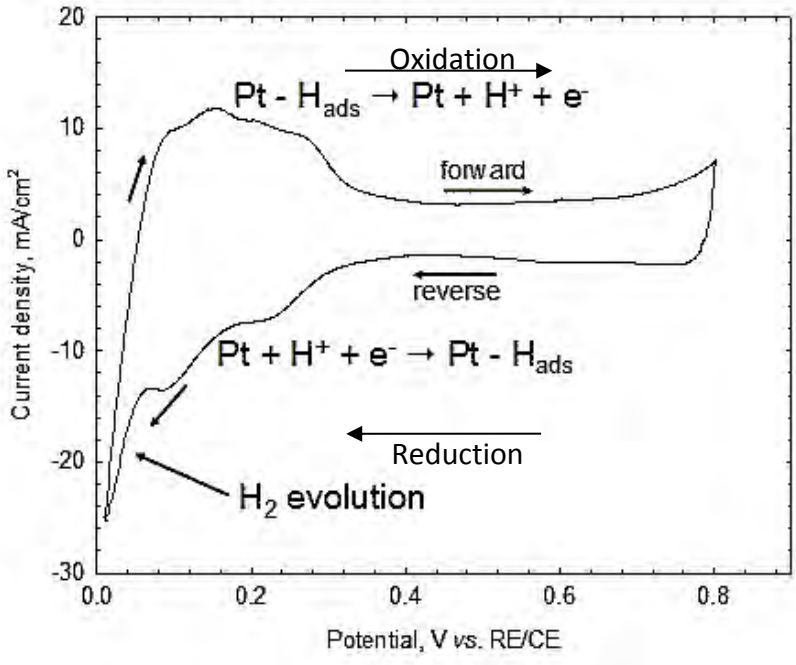


**Figure 22: Cyclic voltammogram of the hydrogen adsorption and desorption reaction for Pt electrode in 0.5M $H_2SO_4$ with a scan rate of 40 mV/s; 35°C; 100% relative humidity anode/cathode; 1 atm. (Cooper, 2014)**

The oxidation reaction is as follows:

$$Pt - H_{ads} \rightarrow Pt + H^+ + e^- \quad (7)$$

The reduction reaction is as follows:

$$Pt + H^+ + e^- \rightarrow Pt - H_{ads} \quad (8)$$

Hydrogen adsorption peaks occur between 0V and 0.4V vs RHE and are assigned as hydrogen underpotential deposition ($H_{upd}$) of a monolayer of hydrogen in the reverse sweep while in the positive sweep it is the release of $H^+$ ions (Zhang, 2008).

Multiple peaks in the region 0- 0.4 V vs SHE are attributed to hydrogen adsorption onto different Pt surfaces. Hydrogen adsorption onto three main Pt faces (100), (111) and (110) was investigated through single crystal studies by Will (1965). These faces can be seen in Figure 23. Will (1965) observed stronger hydrogen adsorption relating to Pt(100) and Pt (110) while more weakly adsorbed hydrogen related to Pt(111). Therefore Hydrogen desorption peaks occur at different potentials. Hydrogen desorption relating to Pt(111)

surface are found in the potential region of ≈0.2 V vs RHE, Pt(110) are related to peaks found at ≈0.22 V vs RHE and Pt(100) surfaces are found at higher potentials of ≈0.27 V vs RHE (Zhang, 2008)

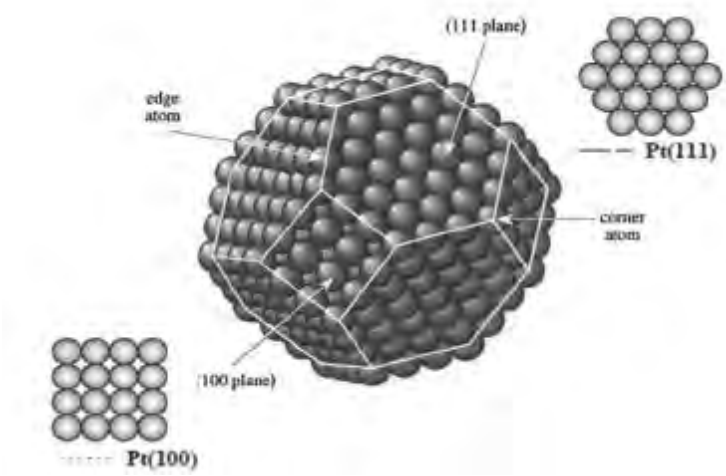


**Figure 23: Model cubo-octahedral platinum particle proposed by Kinoshita (1990) showing Pt atom (111) and (100) crystal faces connected by edges and corner atoms.**

CV is widely used as an electrochemical technique to analyse redox reactions in an electrochemical cell as well as the catalytic activity and electrochemical surface area (ECSA) of the electrocatalyst on the working electrode. For platinum this can be done via the following equation:

$$\text{ECSA}\left(\frac{\text{cm}^2\text{Pt}}{\text{gPt}}\right) = \frac{\text{charge}\left(\frac{\mu\text{C}}{\text{cm}^2}\right)}{210\left(\frac{\mu\text{C}}{\text{cm}^2\text{Pt}}\right) \text{ x catalyst loading}\left(\frac{\text{gPt}}{\text{cm}^2}\right)} \quad (9)$$

$210\left(\frac{\mu\text{C}}{\text{cm}^2}\right)$ is the adsorption charge for an atomically smooth Pt catalyst surface (Babir, 2012).

A recent study into the determination of the electrochemically active surface area of metal-oxide supported Pt catalysts conducted by Binninger et al. (2014) proposed that the standard manner in which ECSA is determine for Pt/C catalyst namely $H_{upd}$ and CO stripping analysis was insufficient for high surface area supported Pt catalysts. It was found that under these methods the standard baselines failed which they suggested was as a result of the contribution of the metal oxide support to the overall CV current as seen in Figure 24(a).

They adopted the baseline methods by using the CV recorded in a CO saturated electrolyte as the baseline for the $H_{upd}$ signal see in Figure 24 (b).

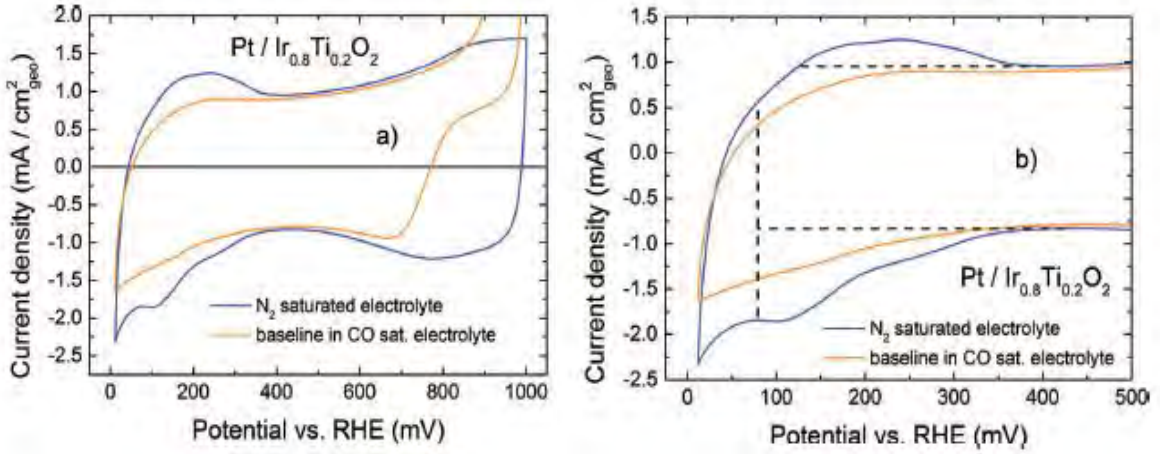


**Figure 24: (a) The CV of $Pt/Ir_{0.8}Ti_{0.2}O_2$ in $N_2$ saturated (blue line) and in CO saturated (orange line) 0.1 M $HClO_4$ at 50 mV/s. Baseline correction CV recorded in CO saturated electrolyte was recorded with rotating electrode at 1600 rpm. (b) $H_{upd}$ region of CV from (a). Horizontal dashed lines indicated the capacitive double layer current used as the standard baseline. The vertical dashed line indicated the lower limit of $H_{upd}$ region. This indicates the underestimation of the $H_{upd}$ region estimated using this standard baseline (Binninger, et al., 2014).**

For the CO stripping method, an alternative method which they termed COSS (CO stripping simulation) was applied to determine the baseline. Here the baseline was taken after adsorbing CO on the Pt electrode in $N_2$ saturated electrolyte (Binninger, et al., 2014). This study indicates the influence of support materials on the methods used to determine the ECSA.

### 2.6.2. CO stripping techniques

Another method commonly used to determine the ECSA of a platinum catalyst system for fuel cells is CO stripping voltammetry. The technique of CO stripping voltammetry and the principles behind it are similar to that of CV. The difference between the two methods is that with CO stripping voltammetry a monolayer of CO is adsorbed on to the Pt surface on the working electrode instead of $H_2$ as in CV. The CO stripping technique with adsorbed CO is preferred over the CV technique with adsorbed $H_2$ because the $H_2$ adsorption/desorption on Pt is difficult to distinguish since there is not always a well-defined baseline for this redox

reaction. On the other hand, adsorbed CO on a Pt catalyst surface oxidises at a well behaved and well-defined peak and baseline. (Barbir, 2013)

The same principle of CV measurement is applied. An example of a CO stripping voltammogram can be seen in Figure 25. The resulting oxidation peak indicates that CO oxidation in the presence of a Pt electrocatalyst occurs between 0.7 V and 0.87 V, depending on the Pt crystalline surfaces. The stripping potential on Pt electrocatalyst surfaces is 0.87V on Pt(111), 0.79V on Pt(100) and 0.70V on Pt(110) (Zhang, 2008).

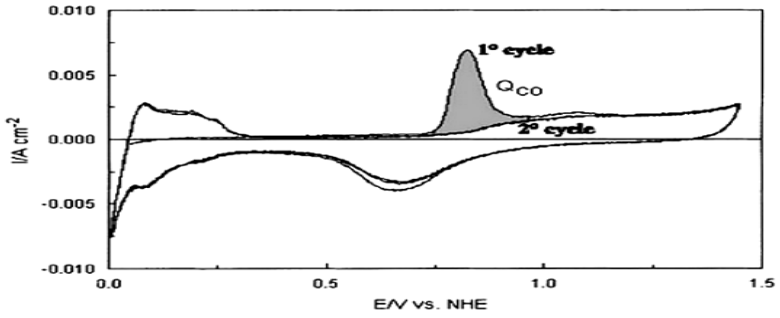


**Figure 25: Cyclic voltammogram at 10mV/s and 25°C on Pt/C (E-TEK) taken in the potential range of 0-1400mV with a CO adsorbed adlayer on the first cycle and without a CO adsorbed adlayer on the second cycle. The shaded area indicates the charge relating to the CO oxidation reaction. (Barbir, 2013)**

The electrochemical reaction of CO on Pt surface is assumed to follow the sequence below.

$$\mathrm{Pt-CO+\ H_2O \rightarrow Pt + CO_2 + 2H^+ + 2e^-} \quad (10)$$

$$\mathrm{[Pt]_2-CO+\ H_2O \rightarrow 2Pt + CO_2 + 2H^+ + 2e^-} \quad (11)$$

To calculate the ECSA based on CO stripping voltammetry, the same equation used for CV given in equation 9 can be applied however the charge to adsorb a monolayer of CO on smooth Pt is 420 μC/cm$^2$Pt (Zhang, 2008) or 484 μC/cm$^2$Pt for polycrystalline Pt (Barbir, 2013).

The loss in catalyst surface area as a result of Pt agglomeration or dissolution can also be determined through the use of CO stripping voltammetry since the CO monolayer oxidation reaction is strongly size dependent.

The influence of particle agglomeration on the catalytic activity of the CO monolayer oxidation on a Pt/C catalyst was studied by Maillard et al. (2005) found that Pt agglomerates show enhanced catalytic activity in comparison to isolated Pt nanoparticles.

The contribution of support material to the surface area determined through CO stripping voltammetry lead to a surface area greater than that found through CV. The capacity of the carbon support material for high surface area catalysts increased the surface area determined by CO stripping by 1.4 times. Thus the surface area determined through $H_{upd}$ method is underestimated when high surface area carbon support materials are used. (Mayrhofer, et al., 2008)

### 2.6.3. Rotating (ring) Disk Electrode (RDE)

Rotating disk electrode (RDE) test is a commonly used method for electrochemical analysis and evaluation of the electrocatalytic properties of a highly dispersed electrocatalyst. It allows identification of mass transfer or electrode kinetics.

The electrode is typically made of noble metal or glassy carbon. The electrode is embedded in a non-conductive stagnant electrolyte solution. The reactants in the stagnant solution transport to and from the electrode through diffusion or convection. Diffusion is the dominant transport process since the effects of natural convection from external environmental vibrations or uneven temperature distribution are minimal (Qui, 2008). Forced convection is introduced to the system to increase the mass transport rate. By rotating the electrode at constant frequency a relative motion between the electrode and electrolyte will create convection. A vortex forms as shown in Figure 26 by rotation of the disk which drags the reactants in solution (known as the hydrodynamic layer) to the surface of the electrode and then flings the product away at right angles to the surface of the electrode by the resulting centrifugal force.

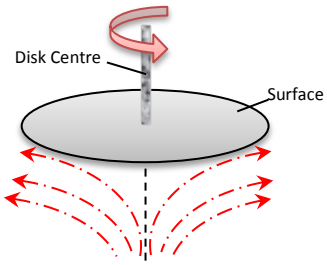


**Figure 26: The flow profile of the reactants and products at a rotating disk electrode.**

However, covering the surface of the electrode is still a stagnant reaction layer through which the reactants then transport by diffusion. Angular velocity ($s^{-1}$) of the electrode, $\omega=2\pi f$ controls the thickness of this layer. The higher the angular velocity, the thinner the diffusion layer becomes. The rotation rate is kept in the range which ensures laminar flow of the electrolyte (Qui, 2008).

By running linear sweep voltammetry under various rotation rates various electrochemical phenomenon can be observed. As mentioned before, RDE can be used to analyse the kinetics of the electrochemical system and more specifically in terms of fuel cells, it is used to study the ORR activity and kinetics. In order to do so the Kouthecky-Levich equation can be applied:

$$\frac{1}{i} = \frac{1}{i_k} + \frac{1}{i_d} \qquad (12)$$

Where i is the overall current produced by the system which is related to the kinetic current ($i_k$) and the limiting diffusion current ($i_d$).

Kinetic current is the current achieved under negligible mass transfer limitations and can be expressed as:

$$i_k = nFA_E K_f C \qquad (13)$$

Where n is the number of electrons, F is faradays constant, $A_E$ is electrode surface area, $K_f$ is the rate constant dependent of overpotential and C is the reactant species concentration.

When the overpotential is high enough for the reaction rate to be determined by the mass transport rate of the reactant at a given electrode rotation rate then a steady state

diffusion-controlled current is achieved. Here current is limited by diffusion and the diffusion layer thickness and can be described by the Levich equation:

$$i_d = 0.620nFA_E D^{\frac{2}{3}} \omega^{\frac{1}{2}} v^{\frac{-1}{6}} C \quad (14)$$

Where D is the diffusion constant, ω is the angular rotation speed, v is the kinematic viscosity of the solution.

The plot of $i^{-1}$ vs $\omega^{-1/2}$ will generate a straight line where the slope can be used to determine the diffusion coefficient, and the intercept once the line is extrapolated till ω=0 is equal to $K_f$, the rate constant dependent of overpotential. This kinetic current can then be used to determine the catalytic activity of the reaction.

RDE can be extended by adding a coaxial ring outside the disk electrode to form a rotating ring disk electrode (RRDE). Figure 27 indicates a schematic of this system with the products and side products of the reaction on the ring and disk.

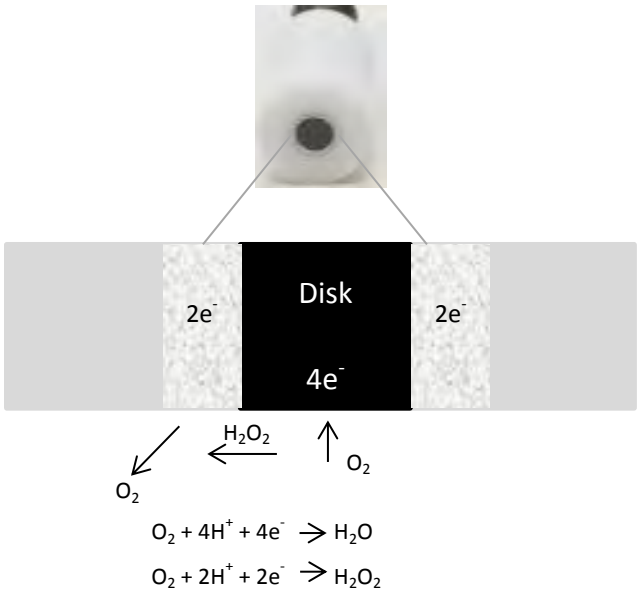


**Figure 27: RRDE mechanism of oxygen reduction at the disk and reduction of peroxide at the ring**

This ring will detect the products being swept away from the electrode. This is done by setting the potential of the ring electrode to a potential to induce immediate reaction of the

product. The product is then identified by the potential of the reaction and the amount of product formed is determined by the current observed at the ring electrode ($i_{Ring}$). Specific to the hydrogen fuel cell, the ring is used to determine the peroxide formation at the catalytic surface. The potentials are swept to allow the ORR to occur at the surface of the disk the ring potential is set to reoxidise any peroxide formed. (see equation 15 and 16 for the reaction sequence) (Qui, 2008).

$$O_2 + 4H^+ + 4e^- \rightarrow H_2O \quad (15)$$

$$O_2 + 2H^+ + 2e^- \rightarrow H_2O_2 \quad (16)$$

## 2.7.Accelerated Durability Tests (ADT)

Durability of electrocatalysts and catalyst support remains a technical barrier for commercialisation of PEM fuel cells for both stationary and transportation applications. The degradation mechanisms of these components have been explained in Section 2.2.3. Various stability testing methods have been investigated in literature for both *in-situ* and *ex-situ* (Colon-Mercado, et al., 2004) (Stevens, et al., 2005) (Yu & Ye, 2007). These testing protocols involve specific conditions and cycles designed to isolate effects and failure modes.

To test the durability of catalysts is an impractical task because it is time-consuming and costly. The lifespan of PEM fuel cell materials are for example greater than 5000h for transportation and greater than 40 000h for stationary applications (Knights, et al., 2004). For this reason accelerated durability tests (ADT) have been developed and are widely accepted as a method of catalyst durability study.

Different ADT protocols are designed for the various fuel cell components namely the electrocatalyst, support, membrane, gas diffusion layers and so forth because they suffer different degradation mechanisms under different conditions. Two ADT protocols will be addressed in this review as they focus on two specific areas of interest namely electrocatalyst and support degradation.

### 2.7.1. General catalyst/catalyst layer ADT protocols

The most commonly employed ADT stressor is potential control. In order to study cathode Pt dissolution/agglomeration and carbon/support corrosion, potential control protocols used are square or triangular wave potential control and steady-state potential control to specified voltage values (Zhang, et al., 2009).

More specifically, Pt chemical and electrochemical stability can be tested using rectangular step waves (30s/step) as shown in Figure 28 cycling between voltages from 0.6 to 0.95V vs RHE. When the potential is lower than 0.9V vs RHE , generally, the influence is limited to Pt catalyst degradation. Changes in Pt surface coverage from oxide coverage (0.9 V and above) to oxide free (0.65 V and below) occurs between these limits (Wu, et al., 2008). The rectangular step wave allows for complete overall investigation of corrosion of the catalyst as it is held at a potential for a period of time. This allows for surface defects and anchoring site of Pt to corrode.

Catalyst support stability testing requires a different set of protocols since the support degradation mechanism is different to that of the catalyst. Support corrosion can be tested using the triangular wave functions also seen in Figure 28. The symmetric triangular waves are cycled between 1.0 and 1.5V vs RHE (Mitsushima, et al., 2007)(Parks et al., 2012). At these potentials corrosion is accelerated therefore degradation is only attributed to that of the support. Another method of support degradation testing is to hold the potential of the working electrode at a potential between 1.2 and 1.5 V vs RHE for a prolonged period (24 hr or more) and measure CVs periodically.

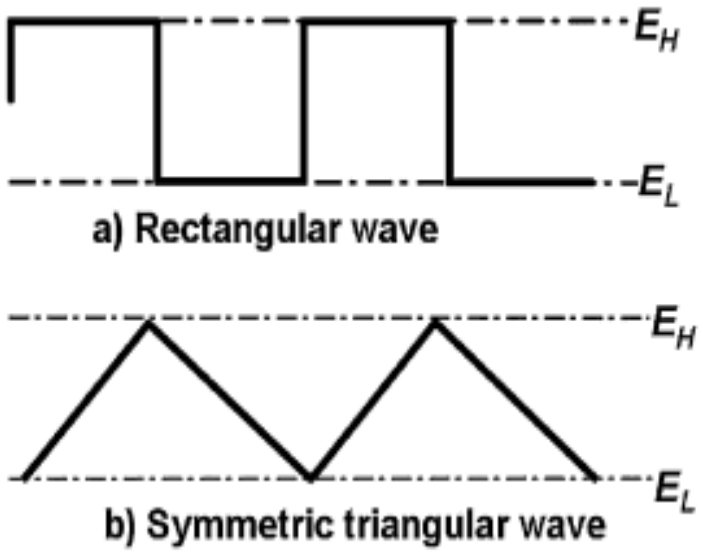


**Figure 28: Potential cycling profiles in durability studies (Charreteur et al., 2008)**

# 3. OBJECTIVES AND HYPOTHESES

Following the preceding review of the relevant literature, it can be seen that there is a need to shift away from using carbon as a support material. Alternatively various catalyst support structures also provide promising results for fuel cell performance. These structures highlight alternative methods to reduce Pt loadings while maximising the Pt utilisation and support durability over a significant amount of time. The overall aim of this study is therefore to apply existing and well-researched electrochemical and physical characterisation techniques on a novel support material. This material is electrospun $TiB_2$ nanofibers. Underneath is an overview of the detailed objectives, hypothesis and key questions guiding this study.

## 3.1.Objectives of Study

The objectives of the study are to:

1) Develop a reliable method to create a catalyst by using TICD to deposit Pt onto $TiB_2$ nanofiber mats, crushed nanofibers and powder support structures.
2) Develop a model catalyst by depositing Pt onto $TiB_2$ nanofiber mats, crushed nanofibers and powder support structures using magnetron sputter deposition.
3) Develop protocols to evaluate the activity of Pt deposited on $TiB_2$ nanofiber mats, crushed nanofiber and powder support structures using typical ex-situ electrochemical characterisation techniques.
4) Physically characterise each support structure and observe the effect of surface morphology, particle size and Pt distribution on the performance of each catalyst.
5) Observe and report the influence of introducing nanostructured support material on the activity of the catalyst through the analysis of physical, electrochemical changes of the catalyst.
6) Determine and report the influence of introducing nanostructured support material on the electrochemical stability of the catalyst through the analysis of ADT.

## 3.2.Hypotheses

Based on the literature reviewed and objectives set for this study, the following hypotheses were developed:

1) Catalyst preparation methods including TICD and DC magnetron sputtering used for $TiB_2$ powder supported Pt catalysts can be used to fabricate Pt catalysts supported by $TiB_2$ nanofibers with minimal changes to these current developed procedures.
2) The activity of a $TiB_2$ nanofiber supported Pt catalyst can be determined using the same electrochemical characterisation techniques/ methods used for $TiB_2$ powder supported Pt catalysts.
3) Inorganic $TiB_2$ nanofiber supported Pt catalysts will result in an improved activity due to the retention of platinum active sites resulting from the enhanced chemical and electrochemical stability of the structured nanofiber material.
4) Platinum supported on $TiB_2$ nanofibers will show a higher resistance to electrochemical corrosion than particle based catalysts under durability testing due to the favourable impact of the nanostructure and morphology.

## 3.3.Statement of Key Questions

This study seeks to investigate the following key questions:

1) Will current developed Pt deposition methods be effective if the support is no longer a powder but a nanofiber?
2) Will ex-situ electrochemical characterisation techniques like CV and CO stripping accurately determine the performance of a nanofiber supported catalyst?
3) How will the electrochemical stability of the structure change when an inorganic support material is used as the support structure?
4) How will the nanofibers support structures influence the electrode performance when compared to a crushed nanofiber and powder based support?
5) Can $TiB_2$ nanofiber mats replace particle based carbon catalyst support materials?

# 4. EXPERIMENTAL PROCEDURE

This section describes the preparation and characterisation of titanium diboride support structures in order to achieve the objectives set in Section 3. The discussion underneath is divided in three section namely catalyst preparation, physical characterisation and electrochemical characterisation.

## 4.1.Materials

A summary of the materials and chemicals used in these experiments are listed below.

**Table 1: Detailed list of dry chemicals used.**

| Name | Manufacturer | Purity | Information |
|---|---|---|---|
| Titanium Diboride Nanopowder ($TiB_2$) | US Research Nanomaterials, Inc | >95%<br>Ti>65.45%, B>29.55% | 58nm, Hexagonal,<br>SSA: 45 $m^2/g$<br>Bulk Density: 0.08$g/cm^3$<br>True Density: 4.52$g/cm^3$<br>Made via Plasma arc vapour-phase synthesis method |
| Carbon Black, Acetylene | Alfa Aesar | 99.9+% | Surface Area= 75$m^2/g$<br>Bulk Density = 170-230g/L |
| Platinum Acetyl Acetonate $Pt(AcAc)_2$<br>$C_{10}H_{14}O_4Pt$ | Sigma Aldrich | 97% | MW: 393.23 g/mol |
| Titanium Diboride nanofiber | Stellenbosch nanofiber Company | | Single fiber Diameter: 300-350nm |
| Alumina MicroPolish | Buehler | 1.00 µm<br>0.05 µm | |

**Table 2: Detailed list of the gases used in this study**

| Gases | Supplier | Purity |
|---|---|---|
| Argon (Ar) | Air Liquide | 99.999% |
| Oxygen ($O_2$) | Afrox | 99.998% |
| Carbon Monoxide (CO) | Afrox | 99.97% to 100% |

**Table 3 Detailed list of liquid chemicals used**

| Name | Manufacturer | Purity | Information |
|---|---|---|---|
| Nafion® | Ion Power | 5wt% | Content<br>Nafion 5wt%<br>Alcohol 75wt%<br>Water 20wt%<br>Density: 0.86 g/cm$^3$ |
| Ethanol Absolute EtOH | Merck | 99.9% | Density: 0.790-0.793<br>MW: 46.07 g/mol |
| Perchloric Acid $HClO_4$ | Sigma-Aldrich | 70% (69.0-72.0%) | MW: 100.46 g/mol |
| Deionised water | Milli-pore | 18MΩ.cm @25°C | |
| Hydrogen Peroxide $H_2O_2$ | Sigma-Aldrich | ≥35% | MW: 34.01<br>Density: 1.13g.mL @20°C<br>Vapour Pressure: 23.3mmHg (30°C) |
| Sulphuric Acid $H_2SO_4$ | Kimix | 98.% | MW: 98.08 g/mol |
| Isopropanol $(CH_3)_2CHOH$ | Kimix | 99.8% | MW 60.10 g/mol |
| Potassium ferricyanide $K_3Fe(CN)_6$ | Sigma Aldrich | 99% | |

## 4.2.Platinum metal deposition

The $TiB_2$ nanofiber supports were supplied by and prepared according to a propriety method developed by Stellenbosch Nanofiber Company. The two different catalyst deposition methods which will be investigated include Thermally Induced Chemical Deposition using a $Pt(acac)_2$ precursor and DC Magnetron Sputter Deposition.

### 4.2.1. Thermally Induced Chemical Deposition (TICD)

This procedure was conducted at the University of Cape Town. Powder catalysts weighing 250 mg was prepared with Pt loadings of 8 wt% and 16 wt%. Platinum acetyl acetonate ($Pt(acac)_2$) precursor was used as the Pt source. The powder support and precursor was placed in the graphite boat seen in Figure 29.

**Figure 29: Small and Large Sigradur® graphite boats used to place the support powder or nanofiber plus metal catalyst precursor for TICD.**

The loadings used for Pt supported by $TiB_2$ were equated to 60 and 40 wt% of Pt supported on carbon. Since $TiB_2$ has a density of 4.5 $g.cm^{-3}$ (see Table 1) compared to Vulcan carbon's density of 0.264 $g.cm^{-3}$ (Cabot Corporation, 2015), comparisons between these two materials could not be made on a weight basis since the Pt per unit surface area would be different. Figure 30 illustrates that by loading the same wt% of Pt on carbon as we would for $TiB_2$, the packing, distribution, interparticle space and degree of agglomeration of platinum

will be severely affected. For that reason the v/v% (volume of Pt / volume of total catalyst) were calculated using the mass and density of the materials and a correction factor of 0.475 for the external surface area ratio between $TiB_2$ and C. These values are supplied in Table 4.

**Table 4: Table indicating the equivalent weight% to vol/vol % pt loadings on different support materials.**

| Support material | Density ($g/cm^3$) | Pt wt% | | |
|---|---|---|---|---|
| | | 0.31v/v% | 0.82v/v% | 1.85v/v% |
| **Carbon** | 0.264 | 20 | 40 | 60 |
| **$TiB_2$** | 4.50 | 2.99 | 7.63 | 15.8 |

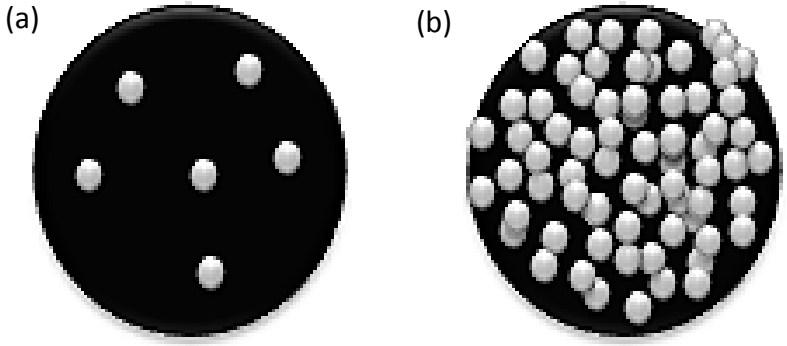


**Figure 30: Illustration of the effect the support materials (a) carbon and (b) titanium diboride have on the platinum loading and distribution for identical wt% Pt loading.**

In the case of the nanofiber supports (crushed or mat), they were individually weighed out and placed in the graphite boat. $Pt(acac)_2$ precursor was added to achieve Pt loadings of 10wt% according to the wt% of Pt in $Pt(acac)_2$. The $Pt(acac)_2$ precursor was evenly scattered from a plastic vial over the nanofiber mat or crushed nanofiber support after placing it in the graphite boat.

The graphite boat was slid in the stainless steel tube of the reactor system seen in Figure 31 which was positioned inside a Labofurn furnace.

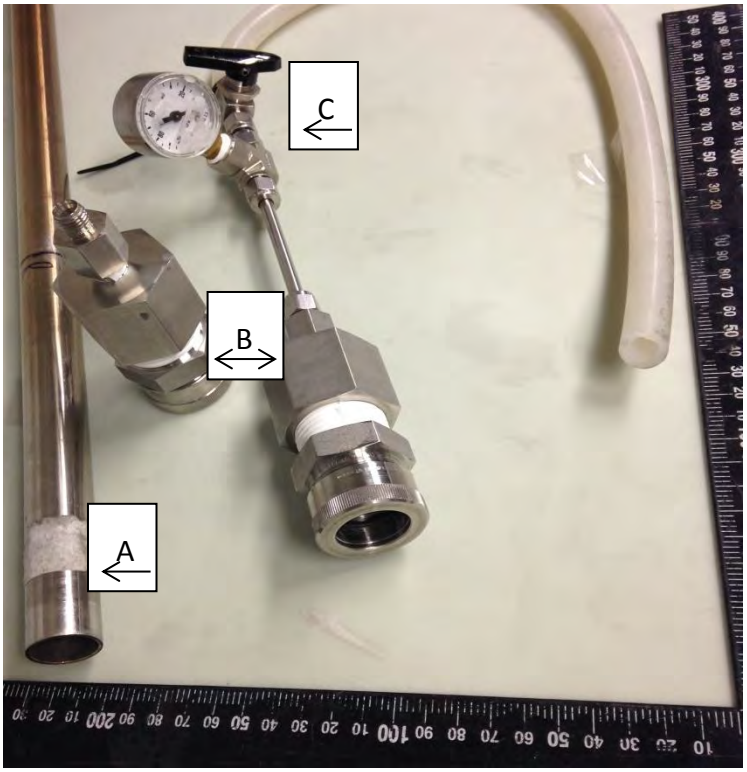


**Figure 31: Reactor system parts for TICD where A is a stainless steel tube which houses the graphite boat in the furnace, B are the two ends of the tube which are sealed to be air tight and C is the mass flow controller and indicator of the Ar gas flowing through**

The furnace was ramped up to 100 °C for 30 min while flowing argon gas through the reactor and kept there for an additional 30 min. Thereafter the gas flow in and out of the reactor was cut and the temperature was ramped to 350 °C for 1 hour and kept at that temperature for 2 hours. The reactor system was allowed to cool in the furnace to alleviate any oxidation from occurring when removing the graphite boat from the reactor and exposing it to air. Once the sample had cooled down it was placed in a glass vial and labelled.

### 4.2.2. DC Magnetron Sputter Deposition

This procedure was carried out at the North West University in Potchefstroom (Prof Cobus Kriek). This deposition technique was chosen to reliably deposit Pt onto the different support structures to create model electrode systems for comparison.

#### *4.2.2.1. Glassy Carbon Disk Preparation for DC Magnetron Sputter Deposition*

5 mm glassy carbon disks (GCs) were polished with diamond paste (6 µm) on a moistened cloth (Buehler, Verdutex) in a figure '8' pattern for two minutes. The polished electrode was then rinsed with water. The electrodes were then further polished to a mirror finish with 1.00 µm and 0.05 µm $Al_2O_3$ particle suspension respectively on Microcloth® (Buehler) for 2 minutes each. The polished electrodes were sonicated for ten minutes in Toluene followed by ten minutes in Ethanol (Merck), ten minutes in water and finally for ten minutes in isopropanol (Kimix). The mirror polished disks were dried in air at room temperature for at least 15 minutes before depositing a film of support and inserting into the sputter chamber.

Polycrystalline Pt disks were prepared with platinum thicknesses resembling the loadings applied to both C and $TiB_2$ supported electrodes. This was done to achieve a base measurement for Pt activity in the cell set-up. Refer to Table 5 for the Pt loadings and thicknesses.

**Table 5: Pt loading and thicknesses sputtered for polycrystalline tests conducted.**

| Pt Mass (µg) | Pt thickness (nm) | Sputter time (min) |
|---|---|---|
| 0.52 | 1.3 | 0.12 |
| 3.35 | 7.9 | 0.75 |
| 9.82 | 23.4 | 2.20 |
| 19.72 | 46.7 | 4.41 |

Glassy carbon disks were then prepared containing the catalyst support inks. To obtain a high quality support film the support material namely $TiB_2$ powder, crushed nanofiber and nanofiber mats were dispersed in a specific alcohol/Nafion ionomer solution to form an ink. Carbon inks were prepared as well and tested as a form of benchmarking for the inorganic support to be compared against. Carbon films were prepared by dispersing the support powder in a water/alcohol/Nation ionomer solution. The content of these inks can be found in Table 6.

**Table 6: Ink formula for the support materials deposited onto the GCs before sputter deposition took place.**

| Support type | Support mass (mg) | Ethanol (µl) | 5wt % Nafion ® (µl) |
|---|---|---|---|
| **Powder** | 10 | 960 | 20 |
| **Crushed nanofiber** | 5 | 480 | 10 |
| **Nanofiber mat** | 2 | - | 5 |

The film thickness is of great importance when doing electrochemical analysis. Thick films may result in mass transport resistance through the catalyst layer. This could hinder access to the electrochemical area of the catalyst thus resulting in a lower electrochemical activity reading. The ideal thickness of a film is of the order 0.2 µm. (Garsany, et al., 2010)

In order to achieve identical support film thicknesses and Pt metal thicknesses for the different support materials, the densities of carbon and $TiB_2$ powder support materials were taken into account. For the nanofibers the thickness of the as prepared mat is fixed at 19 µm and therefore no changes could be made in this case.

#### *4.2.2.2. DC Magnetron Sputter Deposition Parameters*

After insertion of the substrates, the sputter chamber was pumped down to a vacuum base pressure of roughly 5 x $10^{-7}$ Torr in order for effective sputtering to take place. This was done via the combination of two pumps and required more than 12 hours to achieve. A rough pump reduced the pressure to roughly 250 mTorr thereafter the turbo pump kicked in to reduce the pressure to the final base pressure needed. The sputter system contains four water-cooled magnetron guns which sputter in a downward direction. Each gun (seen in the top view of Figure 33) houses one metal target disk. These targets were supplied by ACI Alloys (Inc), California and had fixed diameters and thicknesses of 38.1 mm and 3.2 mm respectively. Platinum targets were placed in the apertures and held at a distance of 90 mm from the substrate. (Falch, et al., 2015)

Calibration of the system with a specific metal target was conducted prior to the sputtering taking place. The parameters which influenced the composition and thickness of the sputtered film include power rating of the magnetron, deposition time, Ar pressure and Ar flowrate. The calibration was conducted by varying these parameters and employing a built-in quartz crystal microbalance (QCM Figure 33 C) to measure the change in mass deposited per unit area (determined by the change in frequency of the quartz crystal resonator). Calibration curves for each metal target, power rating, film thickness and deposition rate were generated form this data and can be seen in Figure 32.

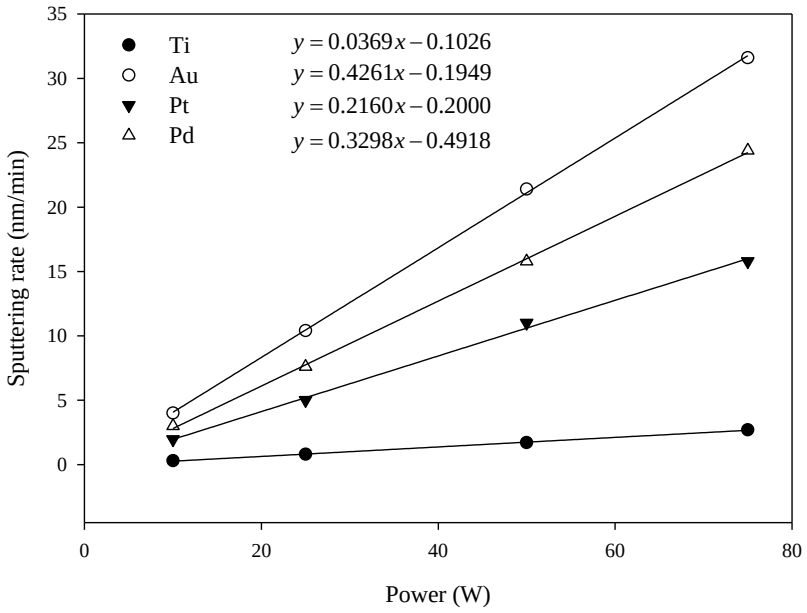


**Figure 32: The sputter system calibration curve for deposition rate (nm/min) versus power rating (W) for various target metals. Conditions: vacuum base pressure, 5 x 10-7 Torr; argon gas flow rate 0.015 L.min$^{-1}$, chamber pressure 8 mTorr. (Falch, et al., 2015)**

Platinum was sputtered onto the prepared glassy carbon electrodes at a power rating of 50 W. At this power Pt deposits according to a specific deposition rate (calculated below). The thickness of Pt metal was used to determine the time required to achieve a certain loading. Glassy carbon disks were placed in the sample holder Figure 34. One holder could house 16 GCs of which 4 loadings could be sputtered. Since the Pt thicknesses are all similar for the loadings, all the electrodes prepared for the different support structures were sputtered at once.

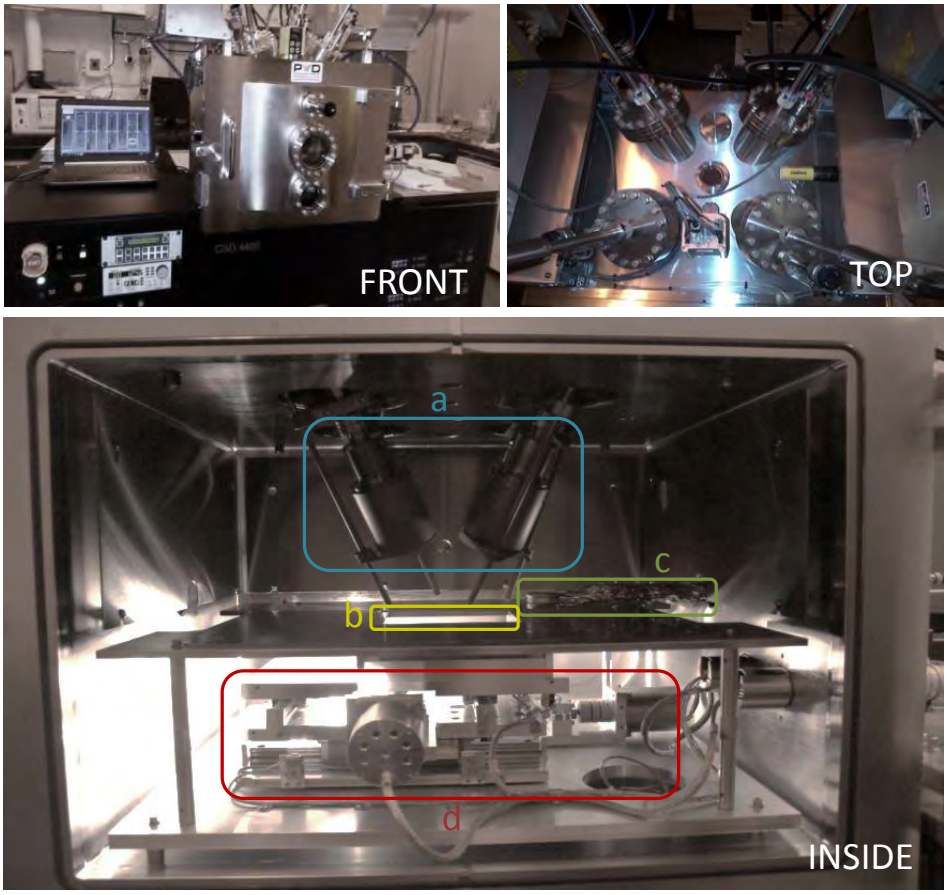


**Figure 33: Images:Different views of the combinatorial deposition system. (a) Four downward facing magnetron guns, (b) variable aperture, (c) quartz crystal microbalance (QCM), and (d) programmable x-y stage.**

**Figure 34: Holder Images e and f are holders for 16 GC electrodes which is placed on the programmable x-y stage.**

According to Figure 32, a Pt target at a power rating of 50 W followed the $y = 0.2160x - 0.2000$ trend. Therefore the sputtering rate was 10.6 nm/min for specific Pt loadings, the

film thickness and deposition time was determined according to the density of Pt and area of the GC.

**Table 7 : Pt loading, mass and deposition time required according to the calibration of the sputter system.**

| Pt mass area (µg/cm²) | Pt mass (µg) | Pt thicknesses (nm) | Sputter time (min) | Sputter time (sec) |
|---|---|---|---|---|
| 200 | 39 | 94 | 8.8 | 529 |
| 100 | 20 | 47 | 4.4 | 263 |

## 4.3.Physical Characterisation

### 4.3.1. Transmission Electron Microscopy (TEM)

Transmission electron microscopy (TEM) was used to determine platinum particle size and distribution on the support for catalysts prepared via TICD. This was carried out using a F20-FEI Tecnai™ electron microscope housed in the Electron Microscope Unit at the University of Cape Town. The samples are exposed to an electron beam of 200kV. The electrons either passes through the sample unaffected are absorbed or scattered. The scattered wave of electrons passes through electromagnetic objective lens to form the image. Denser parts of the micrograph indicate portions where the sample absorbed more electrons where lighter areas correspond to those areas which absorbed less, if any, electrons. Each catalyst sample was prepared by dispersing a small amount of catalyst in acetone inside a centrifuge vial. This mixture was sonicated in an ultrasonic bath for 10 min. Once thoroughly mixed, approximately 5 µL of the solution was deposited onto copper grids. The solution was placed under a lamp in air to ensure all the acetone evaporated from the sample. Once the acetone evaporated the sample was then analysed in the TEM. ImageJ software was used to measure and statistically analyse the particle sizes of Pt and fibers from the transmission electron micrographs.

### 4.3.2. Scanning Electron Microscopy with Energy Dispersive X-Ray Spectroscopy (SEM-EDX/S)

Another physical characterisation technique used was scanning electron microscopy with energy dispersive spectroscopy (SEM-EDS). The surface morphology of the catalyst prepared by TICD and the sputtered Pt electrodes as well as the Pt loading on supports was determined through this technique. This is a non-destructive technique which was carried out using the FEI Field Emission Nova NanoSEM 230, using an Oxford X-Max detector and INCA software, at 30kV housed in the Electron Microscope Unit at the University of Cape Town. Each catalyst was spread onto conductive carbon tape on a sample stub. These stubs

are placed in the Nova NanoSEM chamber under vacuum and irradiated with electron beams. Topographical information is obtained through the detection of secondary electrons scattered after the interaction of the electron beam with the catalyst surface.

EDX/S is used to detect the elements present in the sample and also relative quantities of these elements. Mapping was performed via the SEM with an integrated X-Max EDX system to validate homogeneous sputtering.

When the electron beam collides with the sample in SEM releasing secondary electrons, holes are left in the electron shells of the atoms. To stabilize these holes, electrons from the outer shells with drop into the inner shell. Upon this movement, energy is released in the form of an X-ray. The X-rays emitted are characteristic in energy and wavelength to the element of the parent atom which can assist with the determination of relative atomic percentages.

### 4.3.3. X-ray Diffraction (XRD)

X-Ray diffraction (XRD) was used to determine the crystal structure, Pt crystallite size and lattice constants. A Bruker D8 Advance diffractometer was used with a Cu Kα radiation source operating at 30 kV for zero-background and 40kV for sample holders with background. The scan parameters were set from 20 to 130 2θ. The patterns produced from the XRD were matched and analysed with XRD patterns from the ICCD database. The average Pt crystallite size was determined using the Pt(111) peak and employing the Debye-Scherrer equation shown below in equation 17

$$\tau = \frac{K\lambda}{\beta cos\theta} \qquad (17)$$

Where

τ is the measure for the dimension of the particle perpendicular to the reflecting plane,

K= Dimensionless shape factor ($\approx 0.9$ for spherical particles),

λ is the X-ray wavelength,

β is the peak width,

θ is the angle between the beam and the reflected plane.

The d-spacing between planes was measured using Bragg's equation:

$$n\lambda = 2dsin\theta \,, \tag{18}$$

The lattice constant is calculated by substituting the d-spacing value in the equation below for hexagonal structures (titanium diboride), to determine 'a' which is the lattice constant

For hexagonal structure (e.g metal diborides):

$$\frac{1}{d^2} = \frac{4}{3}\frac{h^2 + hk + k^2 + l^2}{a^2} + \frac{l^2}{c^2} \tag{19}$$

### 4.3.4. Inductively Coupled Plasma Atomic Emission Spectroscopy (ICP-AES)

This analytical technique was used to detect trace metals in a liquid sample. ICP-AES was used as a diagnostic tool after degradation studies were completed to determine the concentration of metals leached into the electrolyte. A Varian ICP 730-ES Spectrophotometer was used to conduct this analysis. This analytical technique identifies trace metals by exciting atoms and ions to emit electromagnetic radiation using inductively coupled plasma. The electromagnetic radiation emitted by the atoms or ions are characteristic to a particular element and therefore elemental analysis can be conducted. The intensity of the emitted electromagnetic radiation indicates the concentration of the element in the sample analysed.

## 4.4.Electrochemical Characterisation

Ex Situ characterisation techniques will be applied in this study to determine the individual catalyst component structure and properties. Furthermore these characterisation techniques will identify the catalyst activity towards ORR and influence of the support structure on the catalyst performance.

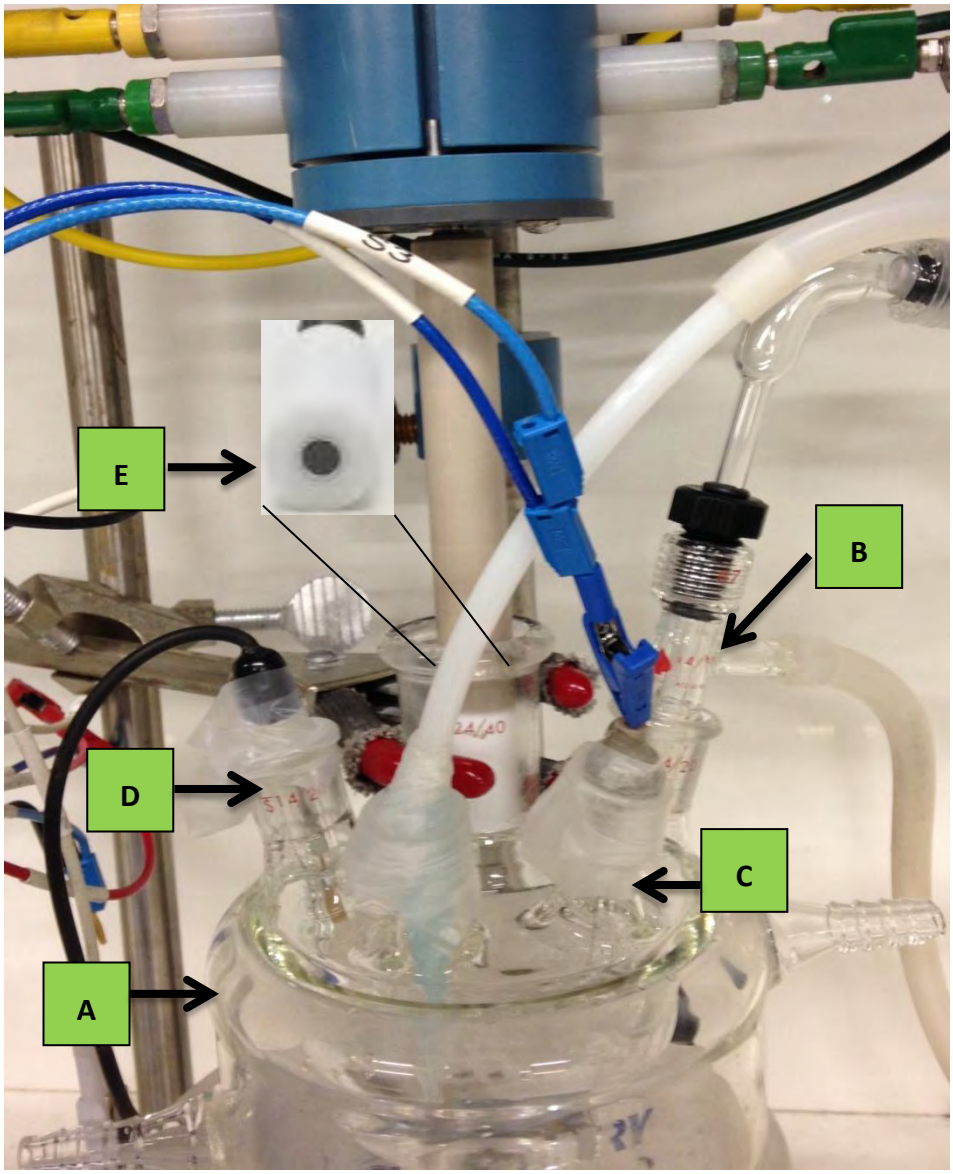


**Figure 35: The electrochemical analysis experimental setup of a three electrode cell consisting of the cell (A), a gas sparger (B), a platinum mesh counter electrode (C), a $Hg/HgSO_4$ reference electrode (saturated $K_2SO_4$) (D) and the working electrode (Pine instruments) (E).**

For all the rotating (ring) disk electrode experiments a SP-300 Bipotentiostat (Biologic Science Instruments) and RDE 710 Gamry rotating electrode was used. As Figure 35 shows, the components making up the typical three electrode cell include a platinum mesh counter electrode (Figure 35, C), a gas sparger for the gas inlet (B) to ensure even distribution of the inert inlet gas to the electrolyte and a $Hg/HgSO_4$ reference electrode (saturated $K_2SO_4$) (Figure 35, D) were used for measurements. All potentials were reported compared to the standard hydrogen electrode (SHE).

An acid electrolyte was used to conduct the electrochemical measurements. A 0.1 M $HClO_4$ electrolyte was prepared using 18.2 MΩ.cm deionised Milli-pore water and 1.256mL concentrated $HClO_4$ (Sigma Aldrich) in a 250 mL volumetric flask.

### 4.4.1. Glassware Cleaning Technique

All electrochemical tests were carried out in a three electrode glass cell in liquid electrolyte. The glassware making up the three-electrode cell (Gamry instruments), shown in Figure 34 in which the catalysts were tested were cleaned by soaking them in oxidative piranha solution. This solution is a 3:1 mixture of sulphuric acid ($H_2SO_4$) and hydrogen peroxide ($H_2O_2$). This solution is highly oxidising and therefore removed all organic residues from the surface. The glassware was left to soak overnight thereafter it was rinsed thoroughly with Milli-pore 18.2 MΩ.cm deionised water. A high degree of caution was exercised when working with the acids. Heavy duty gloves and a face shield were worn over the personal protective gear typically worn in a laboratory.

### 4.4.2. Electrode Preparation

#### *4.4.2.1. Polishing*

As described previously in section 4.2.2.1 the glassy carbon electrodes were polished with diamond paste (6 µm) on a moistened cloth (Buehler, Verdtex) in a figure ‘8’ pattern for two minutes. The polished electrode was then rinsed with water. The electrodes were then further polished to a mirror finish with 1.00 µm and 0.05 µm $Al_2O_3$ particle suspensions

respectively on Microcloth® (Buehler) for 2 minutes each. The polished electrodes were sonicated for ten minutes in water and finally for ten minutes in isopropanol. The mirror polished disks were dried in air at room temperature for at least 10 minutes before depositing a film of catalyst. In the case of TICD, the catalyst is prepared before the ink is deposited whereas in magnetron sputtering, the support is deposited onto the GC before the Pt gets deposited.

#### *4.4.2.2. Catalyst Ink and Film Preparation*

To evaluate the catalysts prepared via TICD an ink of a specific catalyst/alcohol/Nafion® ionomer ratio was prepared. The ink formula for each support structure can be found in Table 7. A catalyst/alcohol/Nafion® ratio was used since the crushed fiber and nanofiber mats have a density that is much lower than the powder catalysts. This was done to ensure that the same amount of catalyst exposed to liquid was achieved in each ink.

**Table 8: Catalyst Ink formula for each support structure**

| Support type | Catalyst (mg) | Ethanol (ml) | 5wt % Nafion ® (µL) |
|---|---|---|---|
| **Powder** | 10 | 3 | 15 |
| **Crushed nanofiber** | 1.5 | 0.5 | 3 |
| **Nanofiber mat** | 2 | - | 5 |

Once the GCs were dry, 20 µL of ink was deposited using a micro-pipette. The nanofiber mat, however, was treated differently. No ink was made for the nanofiber mat in order to preserve its structure. Instead, a disk was punched out using a round cutter which had an area of 0.196 $cm^2$. The stencil cutter can be seen in Figure 36. 5 µL of Nafion was deposited on the GC. Before the Nafion dried, the circular mat was carefully placed over the GC using tweezers. Another method used to attach the mat to the GC was by adding a strip of

conductive carbon tape to the GC then placing the cut nanofiber mat over it. These two methods were tested and the results can be seen in Section 5.

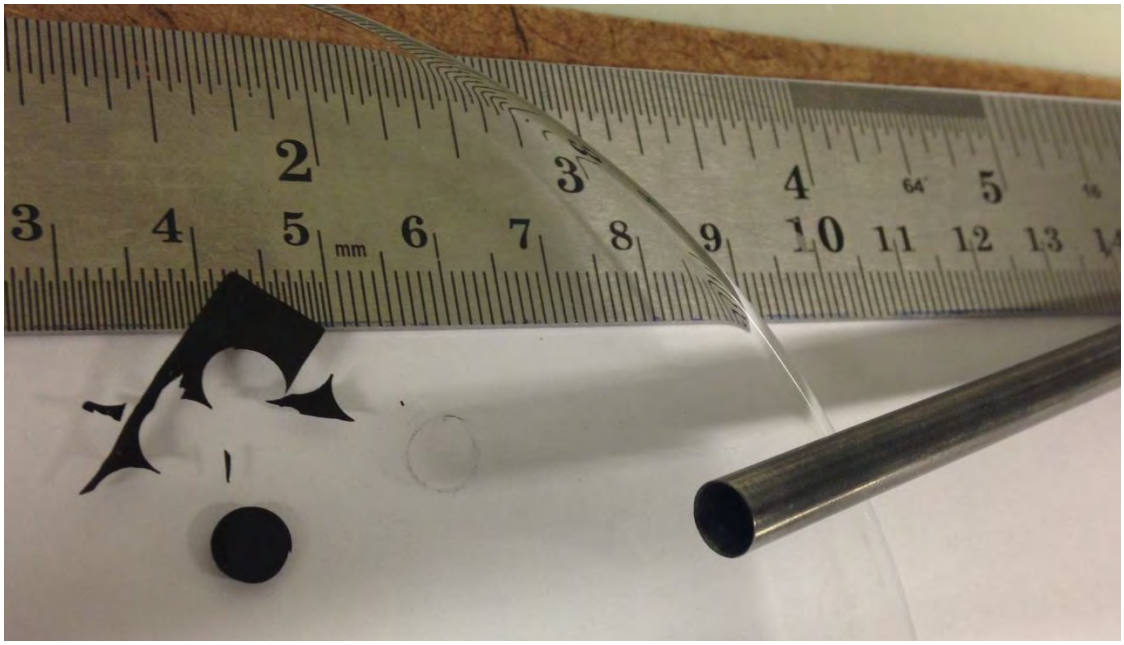


**Figure 36: Stainless steel stencil used to cut a 0.196cm$^2$ disk of nanofiber for electrochemical analysis.**

The drying methods of the ink films were tested in order to determine the optimal drying method which produces the best film. The GCs were left to dry on the counter top covered with a beaker, in a fumehood with a constant flow of air, rotated at 700 rpm and in an oven at 40°C covered with a beaker. The drying method resulting in the best film was found to be the method drying the GC on the counter covered with a beaker. This technique was used to dry all electrode prepared.

### 4.4.3. Electrochemical surface area

#### *4.4.3.1. ECSA measurements using $H_{upd}$ region*

Cyclic Voltammetry (CV) was used as a diagnostic tool to determine the electrochemical surface area (ECSA) of the catalyst. In order to do so, the prepared electrolyte was deoxygenated by purging it with inert Ar gas for 40 minutes. The electrode was pre-wetted before testing by dipping it into a small volume of the remaining 0.1 M $HClO_4$. This was done to ensure no air bubbles sat on the catalyst surface which could block the pathway for

proton flow. The electrode was then inserted into the electrolyte under potential hold 0.5 V vs SHE. Pre-conditioning of the electrode took place initially by cycling the potential of the working electrode 50 times between 0 – 1.1 V vs SHE at a scan rate of 100 mV/s to electrochemically remove any impurities on the catalyst surface. Once a stable CV was observed, the surface was then clean. Thereafter the scan rate was reduced to 20 mV/s. A total of 5 cycles were recorded at the lower scan rate. The ECSA was determined by integrating the charge under the $H_{ads}$ peak of the last cycle using the corrected baseline explained in the next section.

#### *4.4.3.2. CO stripping Baseline correction*

According to (Binninger, et al., 2014) a baseline used for titanium oxides was best generated in a CO saturated environment to avoid the effect of the support material on the baseline correction when calculating the ECSA using the $H_{ads}$ peak in CV. This was done by saturating the 0.1 M $HClO_4$ electrolyte with CO for 25 minutes. While the gas was bubbling, the working electrode in the electrolyte was held at a constant potential of 0.1 V vs SHE. At this potential the CO adsorbs onto Pt surfaces (Maillard, et al., 2005). After the electrolyte was saturated, the working electrode potential was cycled between 0.1 – 1.1 V vs SHE at a scan rate of 20mV/s vs SHE while rotating it at 1600 rpm. A total of 5 cycles were recorded with the $5^{th}$ being used as the baseline for CV correction to calculate the ECSA using the $H_{ads}$ peak.

#### *4.4.3.3. ECSA measurements using CO stripping*

Like CV, this method is also used to determine the surface area of the platinum catalyst and is used to distinguish between Pt agglomerates and isolated nanoparticles. To conduct this measurement, after the electrolyte was saturated with CO for the CO baseline determination, the gas was then changed to Ar and allowed to bubble and saturate for 30 min while holding the working electrode potential at 0.1 V. Thereafter, the working electrode was cycled between 0.1 – 1.1 V vs SHE at a scan rate of 20mV/s vs SHE. A total of 5 cycles were recorded. The first cycle was used to measure the $CO_{ads}$ peak which was oxidised from the Pt surfaces while the $2^{nd}$ cycle was used as a CO free baseline. Equation 20

was used to determine the ECSA assuming 420 μC/$cm^2_{Pt}$ per CO monolayer adsorbed on the Pt surface.

$$\text{ECSA } \left(\frac{\text{cm}^2\text{Pt}}{\text{gPt}}\right) = \frac{\text{charge } \left(\frac{\mu\text{C}}{\text{cm}^2}\right)}{420 \left(\frac{\mu\text{C}}{\text{cm}^2\text{Pt}}\right) \text{ x catalyst loading } \left(\frac{\text{gPt}}{\text{cm}^2}\right)} \quad (20)$$

### 4.4.4. Rotating Disk Electrode Measurements

Linear sweep voltammetry (LSV) was used to determine the activity of the catalysts towards the oxygen reduction reaction (ORR). This technique was carried out after CV measurements were completed. Initially a background CV was measured in an Ar saturated electrolyte by scanning between 0-1.1 V vs SHE at a scan rate of 20mV/s at rotation speeds 400, 900, 1600, and 2500 rpm. This was done in order to obtain the capacitive current associated with the Pt/TiB2 catalysts with which the ORR curves would be corrected.

The RDE measurements were carried out in an electrolyte saturated with $O_2$ for 25 min. The electrode was removed from the electrolyte in order to avoid any oxidation occurring. Once saturated the electrode was positioned back inside the electrolyte and the RDE measurements commenced. The potential was linearly swept between 1.2 – 0.1 V vs SHE and 0.1 -1.2 V vs SHE. The scan rate was set at 20 mV/s at the various rotation speeds of 400, 900, 1600 and 2500 rpm. To obtain the kinetics of the reaction, the ORR curves obtained in the $O_2$ saturated electrolyte were corrected with the background capacitive currents. The Koutecky- Levich equation given in equation 10 was used to calculate the kinetic current ($I_K$) at 0.7, 0.8 and 0.9 V vs SHE by graphically obtaining the limiting current ($I_d$) and current at each potential ($I_{0.7}$, $I_{0.8}$, or $I_{0.9}$) at 1600 rpm rotation speed on the cathodic sweep. The activity of the catalyst to ORR was determined by the mass and intrinsic activity represented as $I_{k,mass}$ and $I_{k,spec}$ respectively.

### 4.4.5. Rotating (Ring) Disk Electrode Measurements for Peroxide Formation

The average number of electrons exchanged during the ORR was determined through the rotating ring disk electrode experiments. These experiments were conducted similar to the

LSV experiments however, the ring was kept at a constant potential of 1.2 V vs SHE. The electrolyte was saturated with $O_2$ for 30 minutes and the potential was linearly swept between 1.2 – 0.1 V vs SHE and 0.1 -1.2 V vs SHE. The scan rate was set at 20 mV/s at the various rotation speeds of 400, 900, 1600 and 2500 rpm.

To calculate the number of electron exchanged, the charge and mass balance equations given in equation 21 and 22 respectively were used. The formation of $H_2O_2$ on the ring correspond with a 2 electron disk current whereas the formation of $H_2O$ corresponds to a 4 electron disk current (Antoine and Durand, 2000)

$$i_{2e^-} = \frac{i_{ring}}{N} \quad (21)$$

$$i_{Disk} = i_{2e^-} + i_{4e^-} \quad (22)$$

And

$$\frac{i_{Disk}}{N} = \frac{i_{2e^-}}{2} + \frac{i_{4e^-}}{4} \quad (23)$$

Therefore,

$$n = \frac{4\, i_{Disk}}{i_{disk} + \frac{i_{ring}}{N}} \quad (24)$$

Where n is the amount of electrons exchanged, $i_{Ring}$ is the ring current, $i_{Disk}$ is the disk current and N is the collection efficiency take as 0.37 (Pine Instruments).

In addition, the ratio of a $H_2O_2$ molecule formed per $O_2$ molecule was calculated using the following equation 25:

$$X_{H_2O_2} = \frac{\frac{2\, i_{Disk}}{N}}{i_{disk} + \frac{i_{ring}}{N}} \quad (25)$$

### 4.4.6. Accelerated Durability studies

#### *4.4.6.1. Support Corrosion*

The stability of the different support structures was measured using support corrosion accelerated durability tests. The procedure used was adapted from the method explained in Yin et al (2010) where they tested the durability of $TiB_2$ powder as alternative support structures for fuel cell application. Support structures without Pt deposited were studied first. For these tests, the support material was deposited on the mirror polished GCs as explained in Section 4.4.2.1 however, the ink did not contain a supported Pt catalyst but rather a blank support as the 'catalyst'. Inks were prepared and deposited as explained in Section 4.4.2.2. To evaluate the support durability using start-stop protocols, cyclic voltammetry was used to conduct the ADT. Electrochemical oxidation (corrosion) was induced by cycling the working electrode potential between 1.0- 1.5 V vs SHE at a scan rat of 500 mV/s for a total of 10 000 cycles. The potential was cycled in a triangular wave pattern as shown in Figure 37 according to Parrondo et.al (2014) for support corrosion tests.

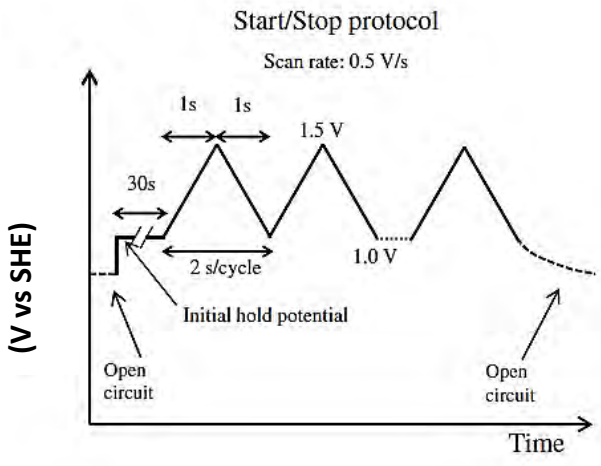


**Figure 37: Start–stop protocols used to evaluate the stability of the support material used. (Image adapted from (Parrondo, et al., 2014)**

CVs were recorded from 0 – 1.1 V vs SHE at a scan rate of 20 mV/s after100, 1000, 2000, 6000 and 10000 corrosion cycles respectively. This was done to characterise the support by estimating the electrode pseudo-capacitance (or current at 0.4 V vs SHE in the capacitance

region of the CV) (Parrondo, et al., 2014). After the tests were conducted, the amount of leached support materials (Ti and B ions) were measured in the electrolyte by ICP analysis.

Support corrosion ADTs were also conducted on Pt supported catalysts using the same protocol explained above. However, to characterise the support and evaluate its stability, the ECSA of the catalysts were calculated with the hydrogen desorption region on the CVs recoded after 100, 1000, 2000, 6000 and 10000 cycles using Equation 9. After these tests were conducted, the amount of leached support materials (Ti and B ions) and Pt were measured in the electrolyte by ICP analysis.

#### *4.4.6.2. Pt Dissolution*

Platinum dissolution ADTs were conducted using the same setup as explained in Sections 4.4.2.1 and 4.4.2.2. Beginning of life (BOL) or initial ECSA was determined via CVs measured as explained in Section 4.4.3. The electrochemical stability of the catalysts was tested using the protocols developed by the Fuel Cell Technical Team of the US Drive Partnership in collaboration with the US Department of Energy, with some minor differences to accommodate the support materials tested (Parrondo, et al., 2014). Pt catalyst stability was evaluated by cycling the working electrode potential from 0.65 - 0.9 V vs SHE in a rectangular wave profile. The scan rate was set at 100 mV/s for 10 000 cycles. The rectangular wave profile can be seen in Figure 38 where it can be seen that the potential was held at each potential for 1 s. The stability of the catalyst was evaluated by measuring the change in ECSA from the CVs recorded after 100, 1000, 2000, 6000 and 10000 cycles.

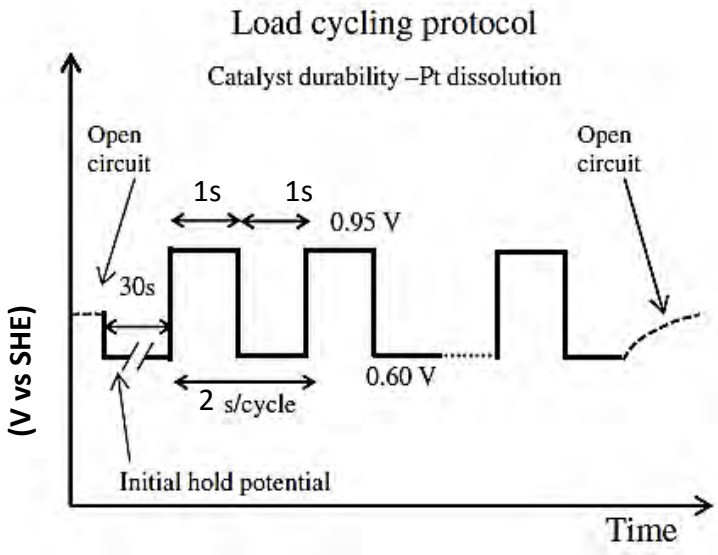


**Figure 38: Load cycling protocol (rectangular wave profile) to evaluate the stability of the Pt catalyst used adapted from Parrondo, et al. (2014).**

# 5. RESULTS AND DISCUSSION

This section details the results and findings of this study into alternative inorganic catalyst support structures. Based on the objectives and experimental plan explained in previous sections, section 5 is divided according to the Pt deposition techniques applied to each support structure. Section 5.1 details the physical and electrochemical findings for Pt deposited on the model sputtered electrode system prepared at North West University. Section 5.2 details the physical and electrochemical results for the electrodes prepared via TICD at The University of Cape Town. Section 5.3 presents the durability of the different structures. Section 5.4 summarises and compares the performance of the catalyst structures prepared by the two systems.

## 5.1.DC Sputtered model electrodes

Section 5.1 details the results found for the model electrode prepared by sputtering Pt loadings of 100 and 200 μg/cm$^2$ onto $TiB_2$ powder, crushed nanofiber and nanofiber mat thin films onto a glassy carbon disk. Model sputtered electrodes were prepared and tested to gain an understanding on the influence of altering support structures on particle size, surface morphology, ECSA and catalyst activity. This technique allowed conclusions to be made based solely on the effects of the support material as the Pt loadings were precise for each support material. Various assumptions were made regarding the model sputtered electrode based on how platinum was distributed on the surface of the support materials. Figure 39 is a schematic demonstration of platinum sputtered onto the support surface over time. A small fraction of the platinum penetrates into the support material therefore not all the support material is available for platinum deposition.

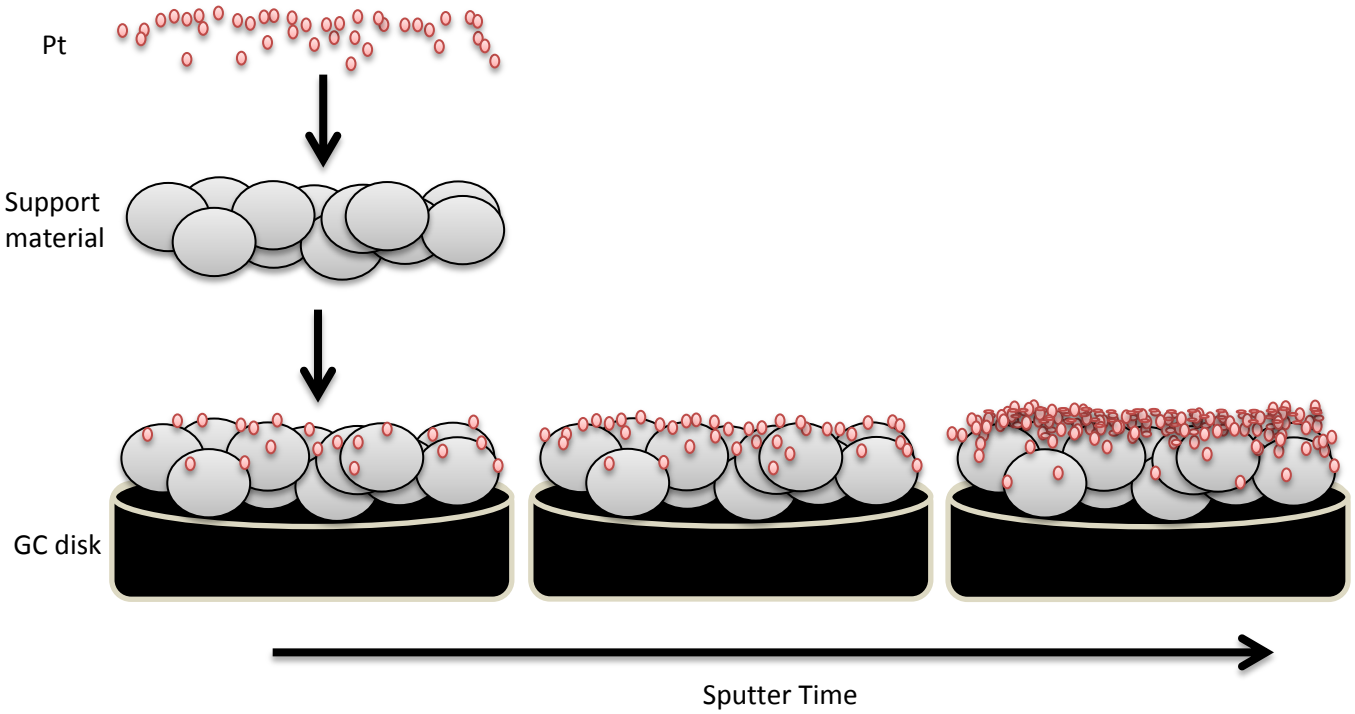


**Figure 39: Schematic illustration of the sputtering process on a MPL with increasing sputter time. (adapted from Schwanitz, et al., 2012)**

The following assumptions were made for the theoretical model sputtered electrode:

- Platinum particles are perfect spheres.
- Platinum particle size is 2 nm and density is 21.46 g/cm$^3$.
- Platinum particle size is consistent throughout the sputtering process regardless of the platinum loading.
- There is a homogenous distribution of platinum on the support surface layer only.

According to the calibration curve in Figure 32 and the assumption made above, the loadings were calculated. A continuous platinum layer with a thickness of 94 and 47 nm at a Pt loading of 200 and 100 µg/cm$^2$ respectively was calculated through this model. Platinum polycrystalline was sputtered onto a support-less GC with a loading of 100 µg/cm$^2$ as a control for the comparisons of support structures.

### 5.1.1. Physical characterisation of sputtered model electrodes via SEM-EDX

SEM-EDX was used to visualise the effects of Pt sputtered on the different support structures as well as the effects of increasing the Pt loading on each support. Figure 40 presented below indicates the morphology of the electrodes with 100 µg/cm$^2$ Pt loading on the various supports.

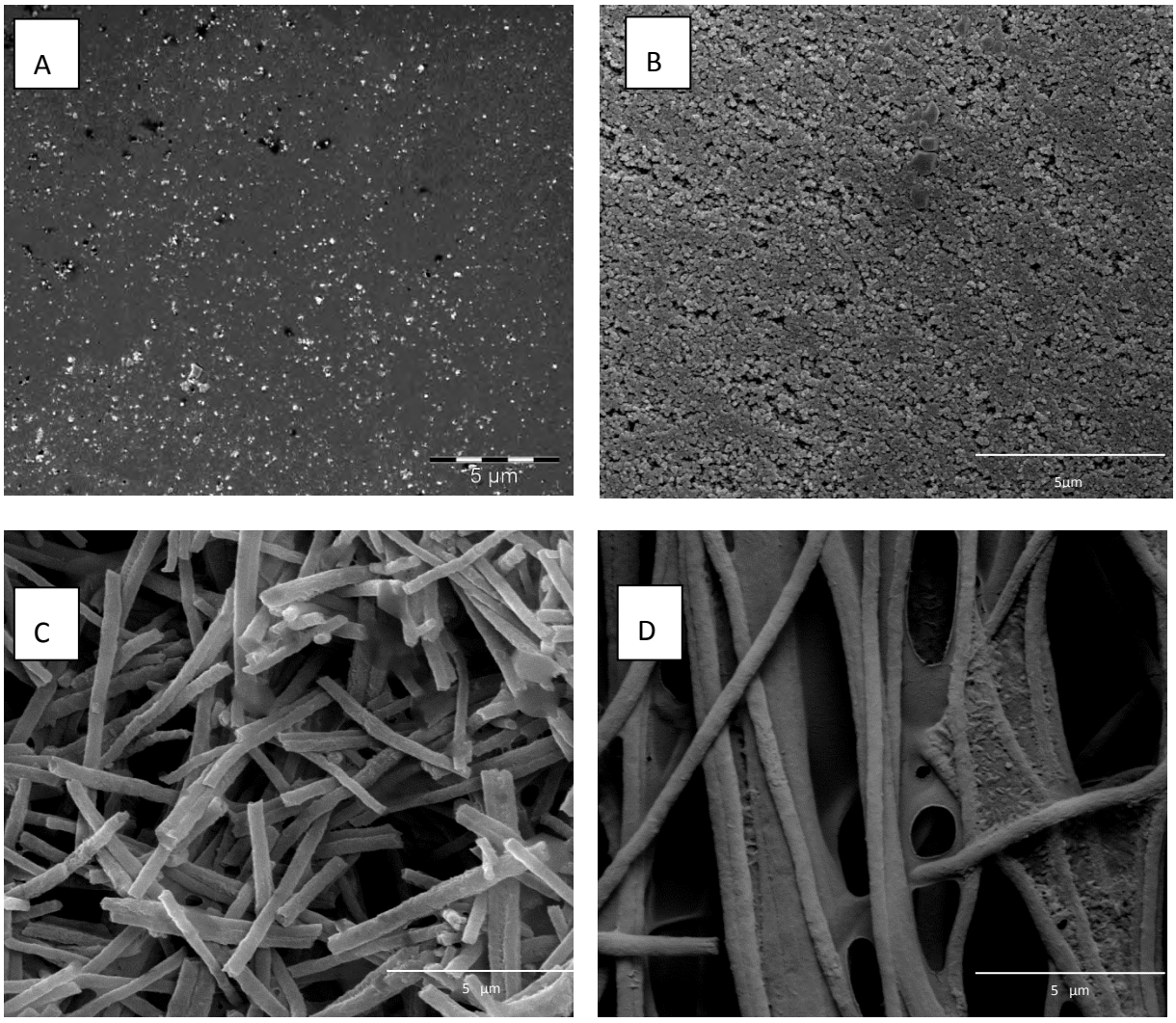


**Figure 40: SEM of 100 µm/cm$^2$ Pt sputtered on A) blank GC, B) $TiB_2$ powder, C) $TiB_2$ crushed nanofiber and D) $TiB_2$ nanofiber mat.**

Figure 40 (A) indicates the Pt sputtered onto a blank GC (no support) electrode. The platinum can be clearly distinguished on a 5 µm scale, which indicates that clusters of platinum particles are present. Figures 40 B, C and D indicate platinum sputtered on the support materials. The lighter grey areas were all identified by SEM-EDX as Pt. Figure D is the only image where an area of isolated platinum can be seen. In general the EDX analysis indicated that a film of Pt was formed on the surface of the support materials as opposed to the expected particles as predicted from the model. Figure 41 presented below illustrates the morphology of the prepared electrodes with 200 µg/cm$^2$ Pt loading.

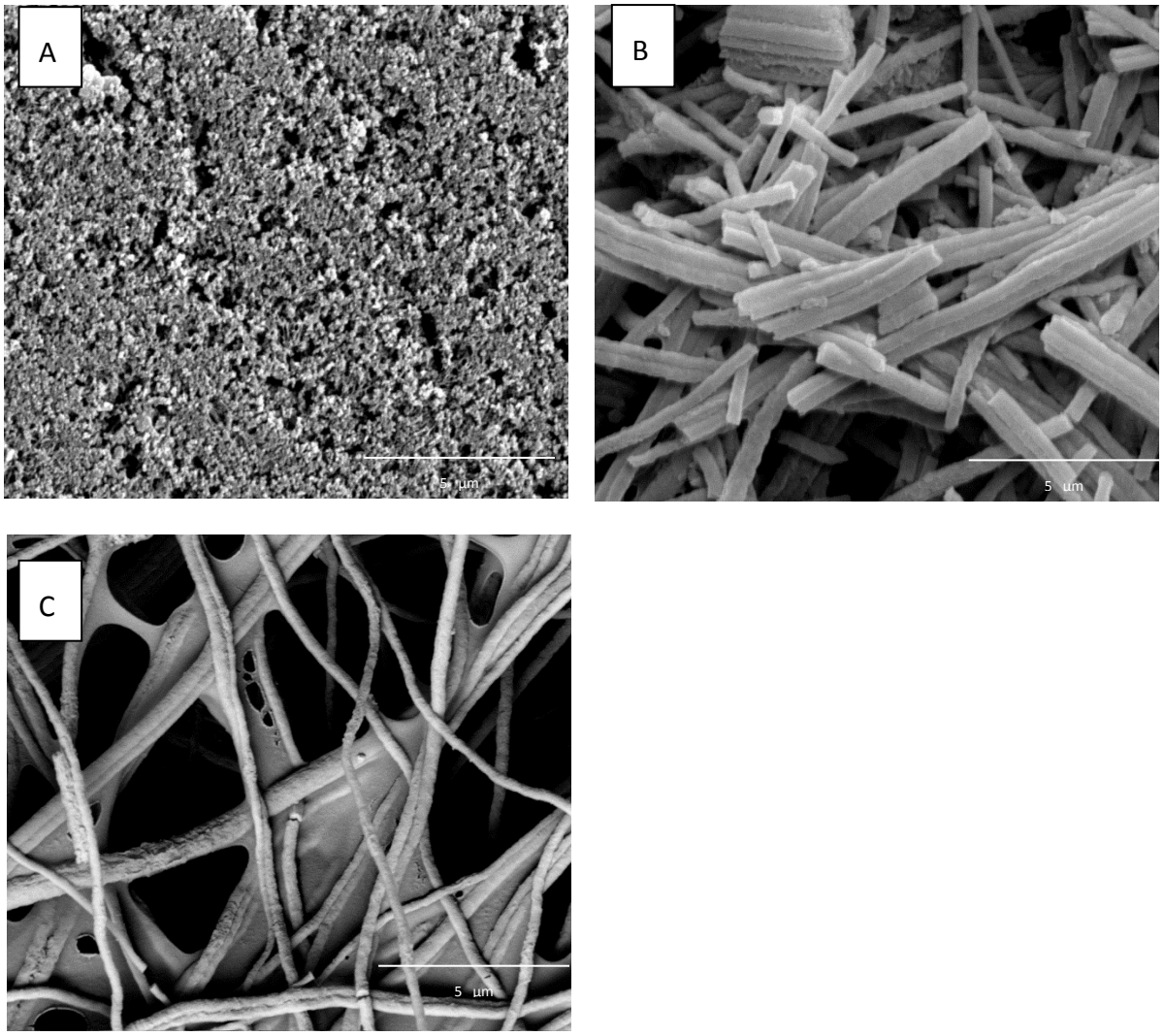


**Figure 41: SEM images of 200 µm/cm$^2$ Pt sputtered on A) $TiB_2$ powder, B) $TiB_2$ crushed nanofiber and C) $TiB_2$ nanofiber mat.**

The increase in the thickness of the white/light grey layers on the support seen from the SEM images in Figure 41 indicate the increase in the amount of Pt. Platinum agglomeration can be seen when comparing A from Figures 40 and 41 by the strong white regions in Figure 41. It can also be seen that there are no isolated Pt particles in Figure 41 B and C thus proving the formation of a thicker platinum film on the surface of the support material.

### 5.1.2. ECSA results of sputtered model electrodes

The cyclic voltammetry curves for each blank support structure are shown in Figure 42. These curves show that $TiB_2$ supports have zero charge in the redox region and no hydrogen adsorption activity at lower potentials. The thickness of the nanofiber material is a constant property therefore the support loading on the electrode is greater than for powder tested in this case.

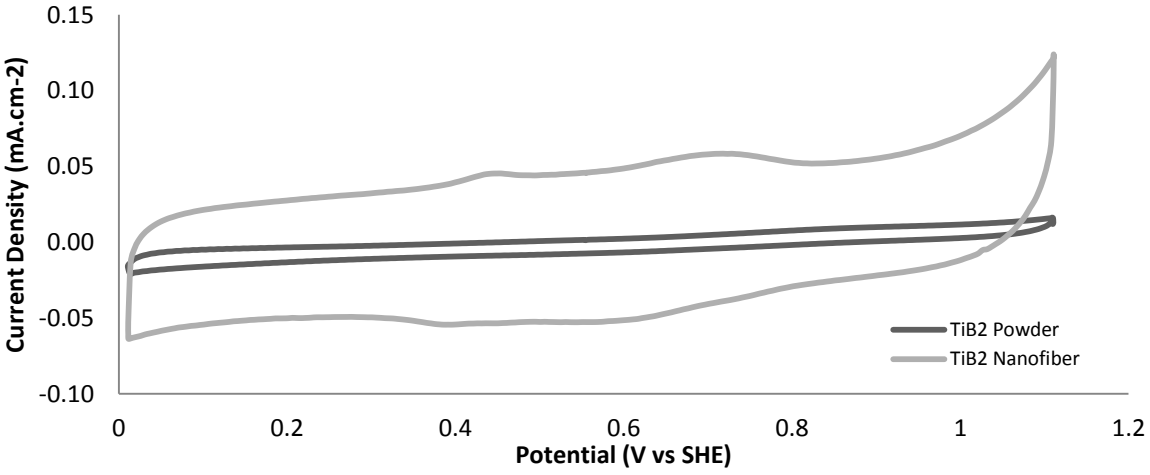


**Figure 42: Cyclic Voltammogram of blank $TiB_2$ support structured measured in Ar saturated 0.1 M $HClO_4$ electrolyte at room temperature.**

The ECSA of the Pt-$TiB_2$ catalysts obtained from $H_{upd}$ and CO stripping experiments were then investigated. These results can be found in the Figures below. The Pt sputtered GC electrode of 100 µg/cm$^2$ was used as a basis to compare the influence of the introduction of support materials on the ECSA. Furthermore ECSA for the 200 µg/cm$^2$ loaded electrodes were investigated and compared to that of the lower loading.

Initially both $H_{upd}$ and CO stripping techniques were evaluated for their suitability for ECSA calculations for these materials. It was found that both methods failed to give accurate and reliable results for the ECSA values. The reason for this was due to the lack of a correct baseline for the integration of the associated charges. This can be illustrated using Figure 43 below as a reference.

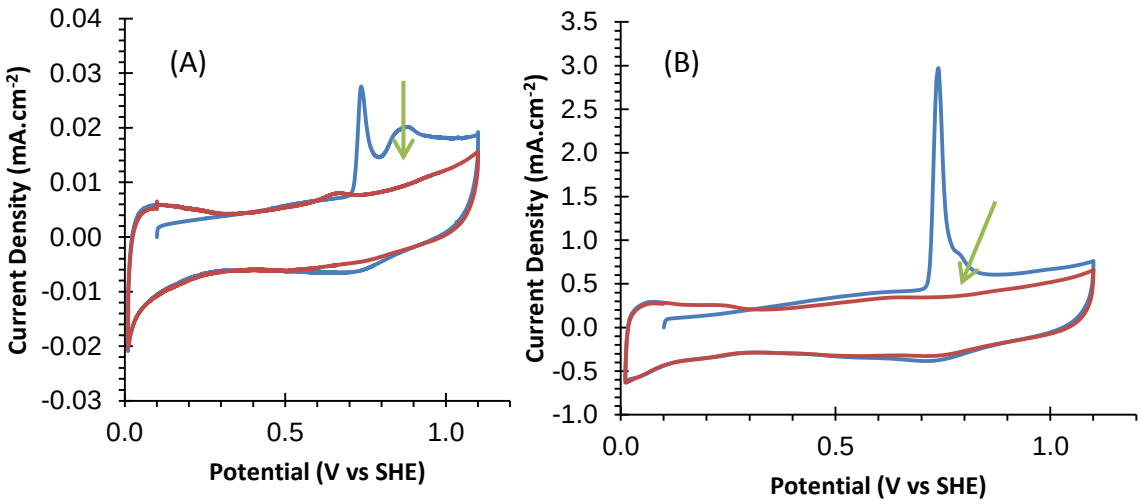


**Figure 43: CO stripping for $TiB_2$ Powder (A) and nanofiber (B) support structures indicating the shift in oxidation currents from the first cycle in blue to the second cycle in red.**

The first and second cycles of the CO stripping experiment are plotted for both powder (A) and nanofiber (B) support. It can be seen that, unlike with conventional Pt/C catalyst CO stripping procedures, the second cycle cannot be used as the baseline for the CO peak in the first cycle. A gap remains between the first and second cycle as indicated on Figure 43 with green arrows. There is an apparent positive offset of the first cycle with respect to the second cycle. Binninger et al. (2014) proposed that this was because the support material is partially reduced when the potential is held at 0.1 V vs SHE to adsorb the CO. The support then re-oxidises during the CO stripping anodic scan of the first cycle. Therefore there would be a large influence of the $TiB_2$ support material on the ECSA calculated via CO stripping. For that reason it was decided to measure ECSA using $H_{upd}$ only. A more accurate baseline was found by Binninger et al. (2014) by measuring the CV in a CO saturated electrolyte at a rotation speed of 1600 rpm. This baseline correction method subtracted the support

material current contributions. This, seen in Figure 44, coincides with the first CV and can therefore be used as a baseline correction for the integration region of the $H_{upd}$ peak.

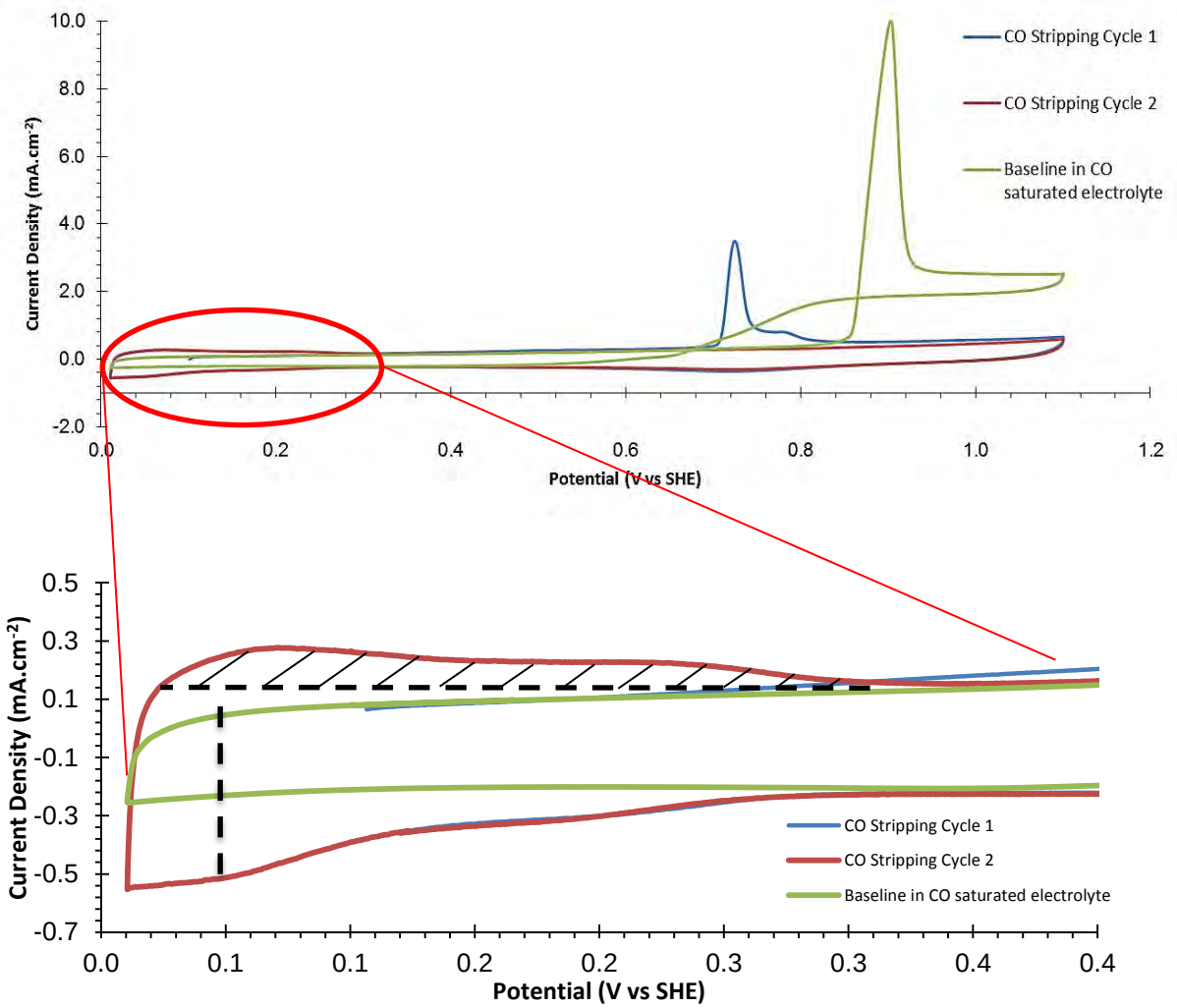


**Figure 44: CV of Pt supported on $TiB_2$ nanofiber in Ar and CO saturated 0.1 M $HClO_4$ electrolyte at 20 mV/s. The baseline indicating the integration region was measured in CO saturated 0.1 M $HClO_4$ electrolyte at 1600 rpm. Horizontal dashed line indicates the double layer currents and the vertical dashed lines indicate the limit of the $H_{upd}$ region**

The current measured for the baseline is purely as a result of the support material since there is no activity in the $H_{ads}$/ $H_{des}$ regions because the active sites are blocked by CO. Conventional $H_{upd}$ integration using the double layer currents as a baseline results in an under estimation of the active surface area as can be seen by the dashed lines. The baseline correction method shown in the Figure 44 was applied to every catalyst support and loading to calculate ECSA reliably.

Cyclic voltammograms of the various support structures with both lower (100 µg/cm$^2$) and higher (200 µg/cm$^2$) loadings are presented in Figures 45 and 46 respectively. The $H_{upd}$ peaks between potentials of 0 - 0.4 v vs SHE were integrated following the CO baseline correction method to calculate the ECSA values.

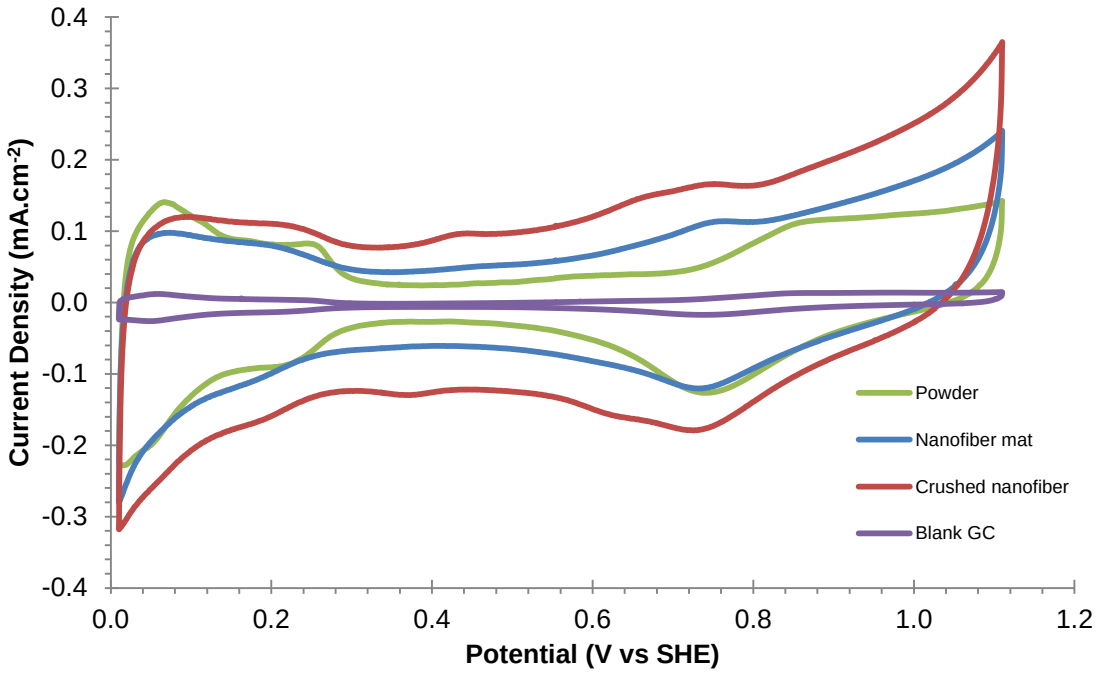


**Figure 45: Cyclic voltammograms of 100 µg/cm$^2$ Pt loaded support structures. These voltammograms were obtained in Ar saturated 0.1 M $HClO_4$ solution at room temperature and a sweep rate of 20 mV/s.**

It can be seen from Figure 45 that there is a significant increase in the double layer charges and $H_{upd}$ regions when a support is introduced to the electrode. It is further clear that the nanofiber materials show a much broader double layer region for similar loadings indicating larger available surface area on the support. The nanofiber mat and crushed nanofibers both show a peak above 1.0 V vs SHE. This indicated that there is an oxidation of the support to $Ti(OH)_3$ above 1.0 V vs SHE. Powder supports display larger $H_{upd}$ peaks and thus display higher ECSA as can be seen in Table 9. The ECSA values obtained are very low, in the range of extended surfaces or bulk platinum which corresponds with the observation from SEM that a film rather than particles were formed.

**Table 9: The experimental ECSA for each support structure Pt loading of 100 µg/cm$^2$**

| Catalyst support type | ECSA ($m^2/g_{Pt}$) |
|---|---|
| **No support (blank GC)** | 2.3 |
| **Powder** | 4.7 |
| **CNF** | 2.4 |
| **NF** | 2.3 |

Cyclic voltammograms for electrodes of a higher loading (200 µg/cm$^2$) can be seen in Figure 46. When comparing the higher loading to the lower loading for each support material there is a clear increase in the current density of the $H_{upd}$ peaks validating the increase in Pt loading.

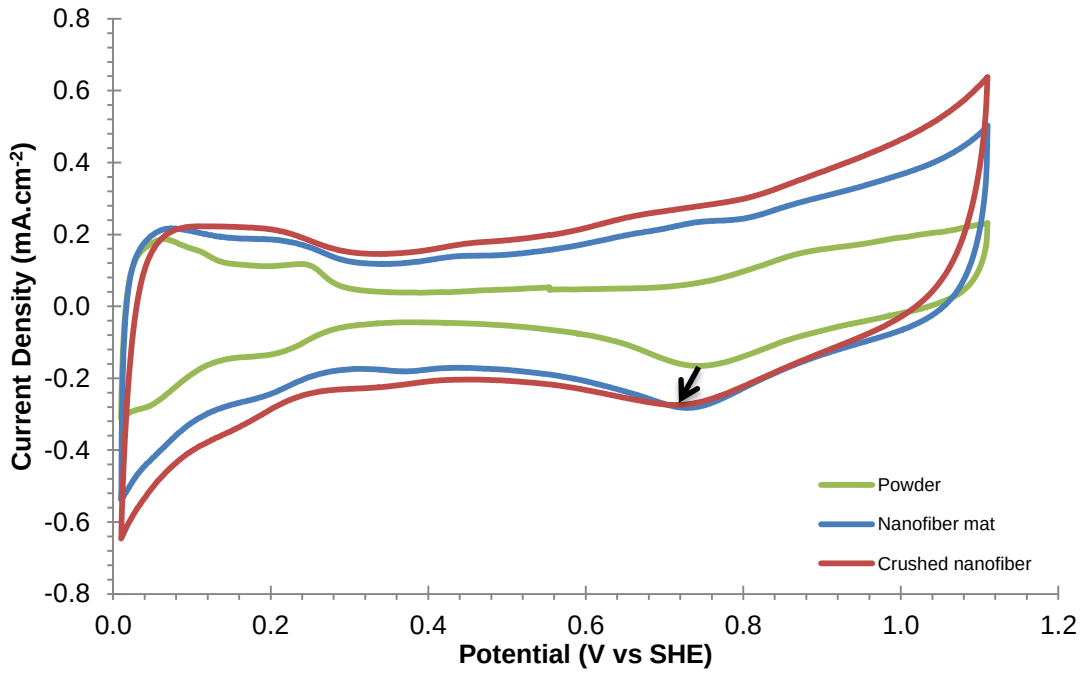


**Figure 46: Cyclic voltammograms of 200 µg/cm$^2$ Pt loaded support structures. These voltammograms were obtained in Ar saturated 0.1 M $HClO_4$ solution at room temperature and a sweep rate of 20mV/s.**

The ECSA corresponding to each $TiB_2$ support structure with the 200 µg/cm$^2$ loading can be found in Table 10. As with the lower loading the values are very low and in the range of bulk platinum. Only for the powdered support structure is there a significant change in ECSA. The

lower value obtained for the 200 μg/cm$^2$ on the powder support compared to 100 μg/cm$^2$ might be due to the fact that some of the particles or particle clusters visible on the SEM analysis agglomerate at the higher loading, thereby lowering the surface area.

**Table 10: The experimental ECSA for each support structure with Pt loading of 200 μg/cm$^2$.**

| Catalyst support type | ECSA ($m^2/g_{Pt}$) |
|---|---|
| **Powder** | 2.7 |
| **CNF** | 2.5 |
| **NF** | 2.4 |

In summary, the much more agglomerated surface leads to very low ECSA values. Therefore there is no clear differentiation between the loadings. At the same time the influence of the support material structure on the ECSA is partly masked by the formation of the Pt film.

### 5.1.3. Electrochemical activity of sputtered electrodes

Linear sweep voltammetry was conducted to determine the oxygen reduction reaction (ORR) activity of each support structure at different Pt loadings. In a first set of experiments the electrodes were prepared with $TiB_2$ materials only. In a second set of experiments carbon black was added into the film to exclude conductivity effects.

#### *5.1.3.1. Measurements on pure $TiB_2$ support*

RDE results for each support structure at Pt loading of 100 μg/cm$^2$ and 200 μg/cm$^2$ recorded at 1600 rpm are shown in Figure 47 and Figure 48 respectively. Kinetic current densities ($i_k$), intrinsic and mass activities at 0.9 V vs SHE where extracted from the data and are presented in Table 11.

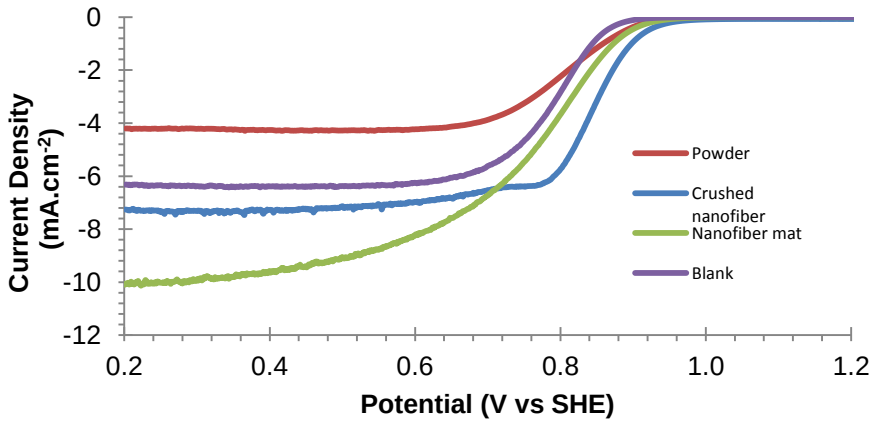


**Figure 47: Oxygen reduction current densities for the cathodic peaks of 100 µg/cm$^2$ Pt loaded support structures measured in $O_2$ saturated 0.1 M $HClO_4$ electrolyte at 1600 rpm and 20 mV/s.**

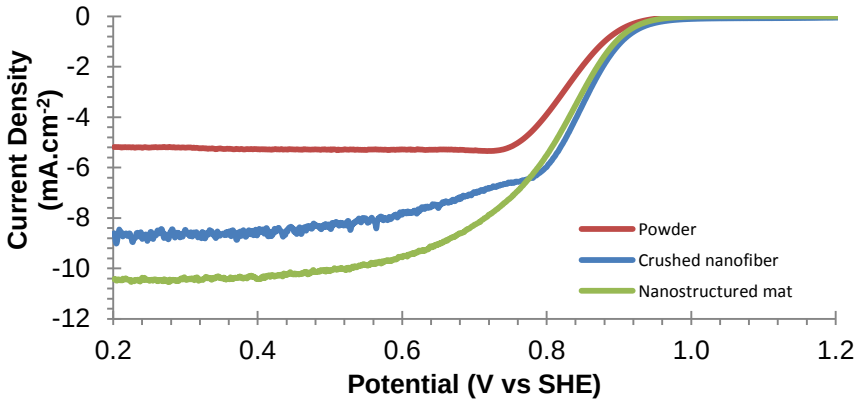


**Figure 48: Oxygen reduction current densities for the cathodic peaks of 200 µg/cm$^2$ Pt loaded support structures measured in $O_2$ saturated 0.1 M $HClO_4$ electrolyte at 1600 rpm and 20 mV/s.**

Summarised values for the Intrinsic and mass specific activities can be seen in Table 11.

**Table 11: Intrinsic and mass specific activity of $TiB_2$ powder, crushed nanofiber and nanofiber mats observed at 0.9 V vs SHE and 1600 rpm for two Pt loadings.**

| Support Type | Intrinsic Activity (mA/cm$^2_{Pt}$) | Mass Specific Activity (mA/$g_{Pt}$) |
|---|---|---|
| **200 µg/cm$^2$ Pt supported on:** | | |
| Powder | 0.11 | 3.09 |
| Crushed Nanofiber | 0.25 | 6.2 |
| Nanofiber Mat | 0.2 | 4.5 |

**Table 12: Intrinsic and mass specific activity of $TiB_2$ powder, crushed nanofiber and nanofiber mats observed at 0.9 V vs SHE and 1600 rpm for two Pt loadings (Continued from above).**

| 100 µg/cm$^2$ Pt supported on: | | |
|---|---|---|
| No support (Bulk Pt) | 0.05 | 1.10 |
| Powder | 0.09 | 3.98 |
| Crushed Nanofiber | 0.44 | 10.0 |
| Nanofiber Mat | 0.20 | 4.85 |

For both loadings the kinetic controlled region on the linear sweep voltammogram extends from about 0.7 – 1.0 V vs SHE. A potential of 0.9 V vs SHE was chosen to compare the kinetic current density, intrinsic and mass specific activities. The diffusion-limited current density, $I_{lim}$, plateaus at 0.2 V vs. SHE. Oxygen diffusion to the catalyst becomes the rate-limiting step at this point. The theoretical diffusion-limiting current density for Pt catalysts of 6.07 mA/cm$^2$ for the ORR cathodic sweep at 1600 rpm was not reached by any of the support materials used. For the powder support it is much lower than the theoretically expected value while for the fiber based ones it is much higher. The blank electrode plateaued at this value since there was no influence of support material on the reduction of oxygen at the catalyst surface, a confirmation that the deviation was not due to experimental error.

The powder support structure diffusion-limiting current density of 4.2 mA/cm$^2$ for 100 µg/cm$^2$ Pt is in the range of the literature values obtained for $TiB_2$ nanoparticle support structures (Yin, et al., 2010). The tilted shape of the LSV curve indicates severe ohmic losses and therefore this suggests that the major issue with the powder is the conductivity. The powder film effectively adds a resistive layer between the GC electrode and the sputtered film. This increased thickness of the catalyst layer results in an additional diffusion resistance thus lowering the diffusion limiting current on the electrode as seen in Figures 47 and 48. This improves slightly when considering the higher Pt loading (Figure 48) where the improvement seems to be linked to the higher degree of Pt agglomeration. The conductivity will be further discussed in the section underneath where carbon was added.

No literature has reported on the limiting current density of $TiB_2$ nanofiber materials as this is a novel support material. The limiting current density obtained is higher than what is theoretically possible for the four electron oxygen reduction. It is speculated that using the 0.196 $cm^2$ geometric surface area of the GC disk to calculate current density in this case is incorrect. One can consider the surface of the powder film to be fairly uniform as seen in Figure 50, as could also be seen from SEM. However the nanofiber and crushed nanofiber films are highly irregular and rough. With a Pt film covering the irregular support surface might lead to a geometric Pt surface that is much larger than 0.196 $cm^2$, resulting in overestimated current densities. Another explanation for the larger than expected mass transfer limited current seen on the nanofiber coated electrodes could be as a result of the laminar hydrodynamic layer on the normally smooth electrode being disrupted. As seen in Figure 50, the nanofiber electrodes have a more roughened surface causing an additional convective mass transfer component to the electrode surface and into the porous electrode layer.

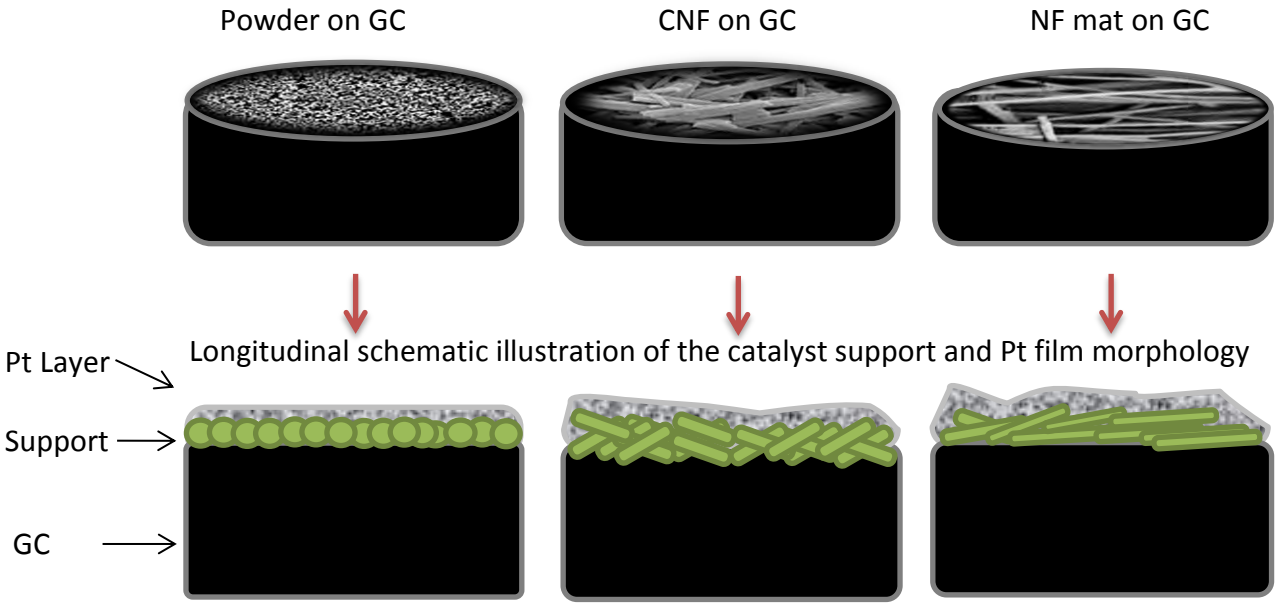


**Figure 50: Longitudinal schematic illustration of the Pt layer over different support structures**

### *5.1.3.2. Measurements with carbon black added to the electrodes*

In an attempt to improve the electron conductivity issues with the semi-conducting $TiB_2$ support material, 20wt% acetylene black (AB) carbon was added to the support ink following the research conducted by Shim et al. (2001) and Xiong & Manthiram (2004). The results of the addition for the individual support structures are shown below.

#### 5.1.3.2.1. Powder support

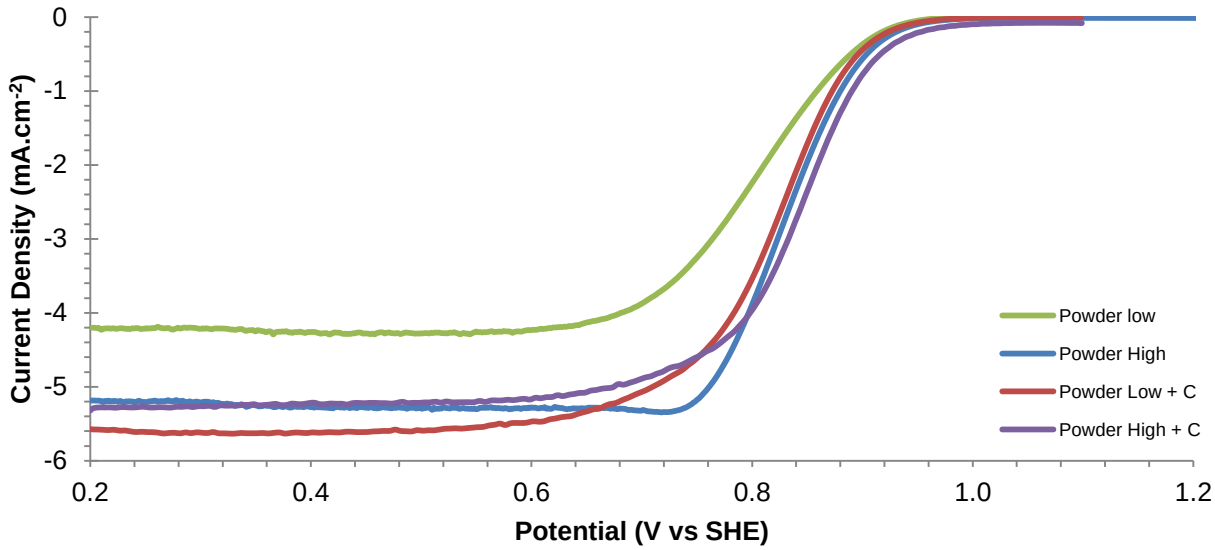


**Figure 51: Oxygen reduction current densities for the cathodic peaks of higher (200 µg/cm$^2$) and lower (100 µg/cm$^2$) Pt loaded $TiB_2$ powder support structures with AB measured in $O_2$ saturated 0.1 M $HClO_4$ electrolyte at 1600 rpm and 20 mV/s.**

There is an overall increase in the kinetic current obtained under ORR conditions as can be seen in Figure 51 and Table 12 summarising the activities of the powder support structure for each Pt loading. The addition of electron conducting AB powder to the support improves the conductivity and allows limiting current density to be reached in the case of the low Pt loaded catalyst. This is a clear confirmation that the earlier observations around poor conductivity are confirmed. For the higher loadings case, there is no clear shift in the limiting current density however the mass and intrinsic activity both increases with the addition of AB to the catalyst. This again confirms that the higher loading forms a more complete film on the support. The conductivity through this extended surface is sufficiently

high and therefore the carbon does not add additional conductivity. Noting the trends of the activity between the higher and lower Pt loading, there is an increase in intrinsic activity ($i_{K,spec}$) which is expected since there is an increase in kinetic current density as Pt loadings increase. This can be due to the fact that the conductive AB 'connects' more areas of the Pt/$TiB_2$ to the GC resulting in a greater degree of available active surface area of Pt for ORR. The mass specific activity ($i_{K,mass}$) decreases with increasing Pt loadings which is also expected since there is a decreased surface area per mass of catalyst with high Pt loadings.

#### 5.1.3.2.2. Crushed nanofiber

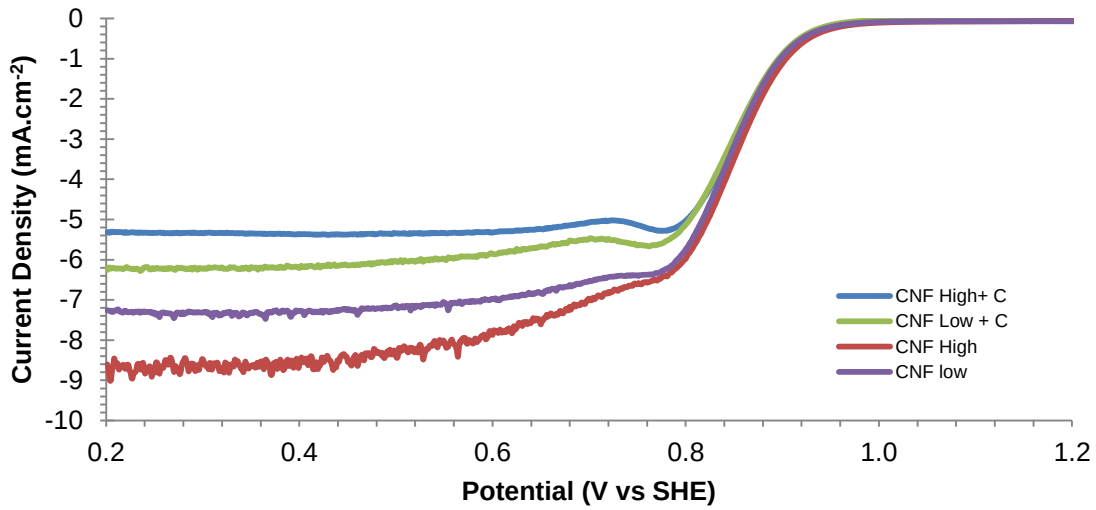


**Figure 52: Oxygen reduction current densities for the cathodic peaks of higher (200 µg/cm$^2$ ) and lower (100 µg/cm$^2$ )Pt loaded crushed $TiB_2$ nanofiber support structures with AB measured in $O_2$ saturated 0.1 M $HClO_4$ electrolyte at 1600 rpm and 20 mV/s.**

There is an overall increase in ORR kinetics and activity seen by Figure 52 and Table 12 summarising the activities of the crushed nanofiber support structure for each Pt loading with the addition of electron conducting AB. Limiting current densities were reached in the case of the lower and roughly higher Pt loaded catalyst. Extending the rationale for the too high limiting current, in this case the carbon assists in obtaining more smooth films in the GC. Once GC is sputtered the geometric surface area of Pt exposed to electrolyte is then closer to that of the GC. Noting the trends of the activity between the higher and lower Pt loadings, $i_{K,mass}$ decreases with increasing Pt loadings which is also expected since there is a

decreased surface area per mass of catalyst with high Pt loadings. The $i_{K,spec}$ does not increase as the Pt loading increases which does not follow trend. The lower Pt loading provided a higher intrinsic activity which could be as a result of the isolated Pt particles found in lower Pt loadings.

#### 5.1.3.2.3. Nanofiber mats

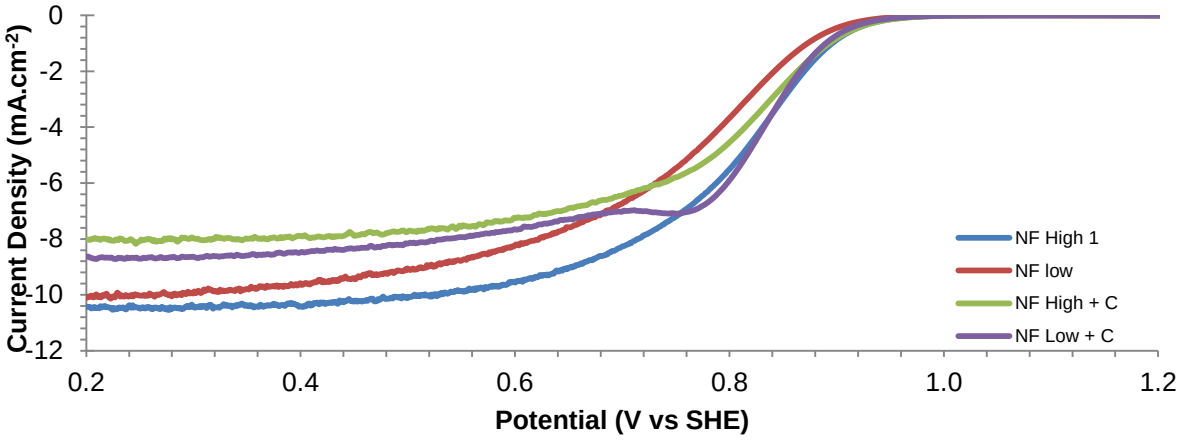


**Figure 53: Oxygen reduction current densities for the cathodic peaks of higher (200 µg/cm$^2$ ) and lower (100 µg/cm$^2$ )Pt loaded $TiB_2$ nanofiber mat support structures with AB measured in $O_2$ saturated 0.1 M $HClO_4$ electrolyte at 1600 rpm and 20 mV/s.**

There is an overall increase in ORR kinetics and activity seen by Figure 53 and Table 12 summarising the activities of the nanofiber mat support structure for each Pt loading with the addition of electron conducting AB. Limiting current densities were, however, not reached in the case of the lower and higher Pt loaded catalyst. There is still an increase in limiting current density in each case. The addition of AB does reduce the roughness of the electrode to some extent but not completely. This proves that there is a significant resistance to electron flow in these support materials. The onset potentials are relatively constant except for lower loaded NF without C. This also validates the $i_{K,spec}$ and $i_{K,mass}$ values in Table 12. Noting the trends of the activity between the higher and lower Pt loadings, $i_{K,mass}$ decreases with increasing Pt loadings which is also expected since there is a decreased surface area per mass of catalyst with high Pt loadings. There is an increase in $i_{K,spec}$ which is expected since there is an increase in kinetic current density as Pt loadings increase. This can be due to the greater degree of available active surface areas of Pt for ORR.

**Table 13: Intrinsic and mass specific activity of $TiB_2$ powder, crushed nanofiber and nanofiber mats after the addition of acetylene black observed at 0.9 V vs SHE and 1600 rpm for two Pt loadings.**

| Support Type | Intrinsic Activity ($mA/cm^2_{Pt}$) | Mass Specific Activity ($mA/g_{Pt}$) |
|---|---|---|
| **200 µg/cm² Pt loading** | | |
| Powder + AB | 0.23 | 4.13 |
| Crushed Nanofiber + AB | 0.46 | 6.30 |
| Nanofiber Mat + AB | 0.35 | 4.69 |
| **100 µg/cm² Pt loading** | | |
| Powder + AB | 0.15 | 4.45 |
| Crushed Nanofiber + AB | 0.49 | 10.5 |
| Nanofiber Mat + AB | 0.25 | 7.60 |

### 5.1.4. RRDE results for hydrogen peroxide formation

RRDE experiments were carried out to determine the extent of hydrogen peroxide ($H_2O_2$) formation of the catalyst surface of each support structure with 100 µg/cm² Pt loadings. The collection efficiency of the ring was taken as 0.37 which was found to be independent of rotation speeds. The potential of the ring caused by $H_2O_2$ oxidation and disk caused by oxygen reduction via a 2 $e^-$ or 4 $e^-$ reaction pathway were measured and the plot for the cathodic sweep at 1600 rpm are given in Figure 54 (A) for powder (B) for crushed nanofiber and (C) for nanofiber mat.

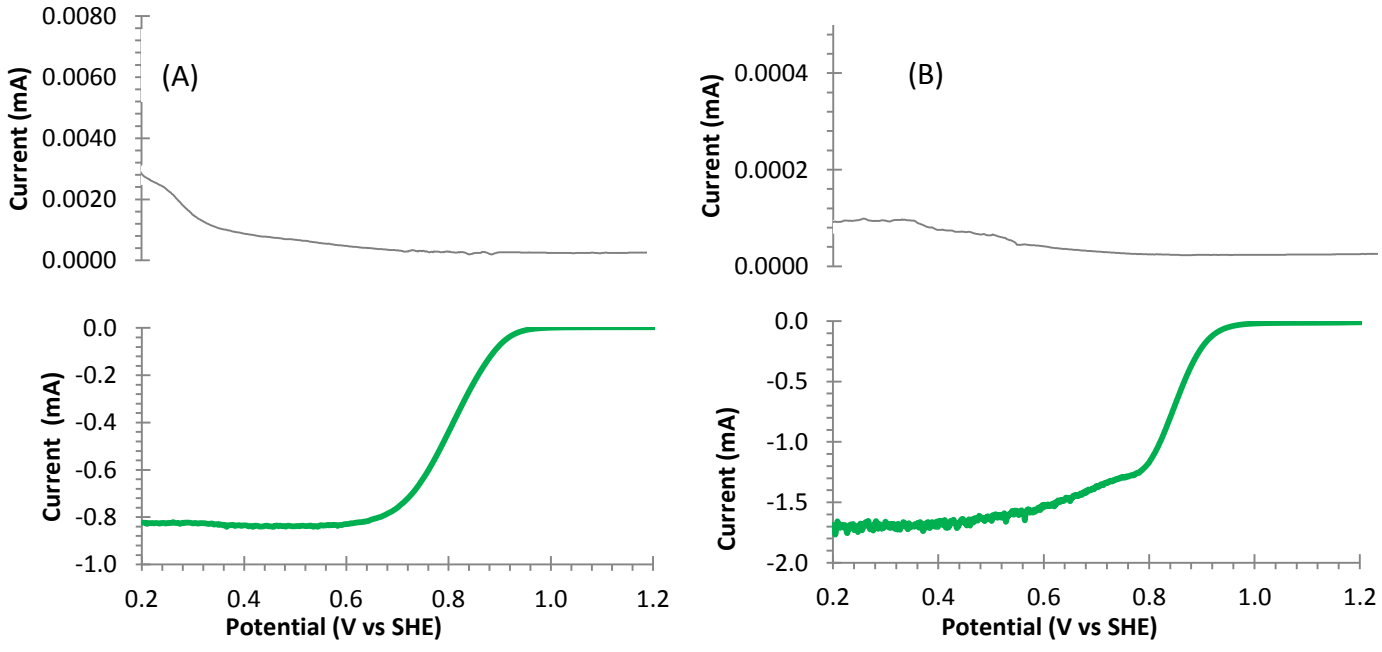

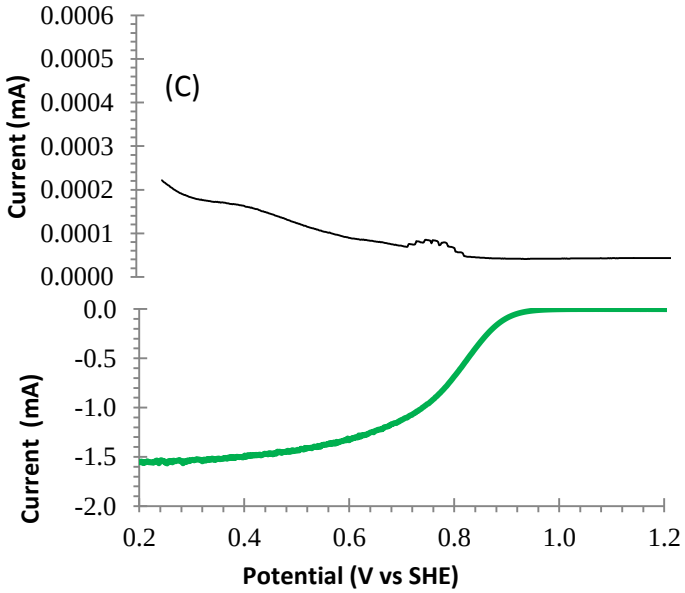


**Figure 54: RRDE hydrodynamic voltammograms for ORR of 100 µg/cm$^2$ Pt on (A) powder, (B) crushed nanofiber and (C) nanofiber mat supports in an oxygen saturated, 0.1 M $HClO_4$ electrolyte at room temperature at 1600 rpm. The Pt ring electrode was held at 1.2 V vs SHE and its current caused by $H_2O_2$ formation can be seen in the grey curve. The ORR current of the Pt sputtered disk electrode can be seen in the green curve.**

Hydrogen peroxide ($H_2O_2$) formation can be observed by the increase in ring current below potentials of 0.8 V vs SHE in the green lined in Figure 54. Despite the increase in $H_2O_2$ formation, the current of the ring in each support material remains low ranging between 0.1 - 0.3 µA indicating the insignificant amount of $H_2O_2$ production. The percentage of $H_2O_2$ formed in the cathodic down sweep on the ORR at 1600 rpm for each support material can be seen in Figure 55 below. Nanofiber mats produce the highest percentage of $H_2O_2$ between the support structures. The number of electrons for oxygen reduction was calculated using equation 24 and it was found that the ORR follows a 4 $e^-$ reaction pathway for each support structure. Fabbri et al. (2014) suggest that the insignificant $H_2O_2$ formation is as a result of a greater degree of Pt agglomerates which was validated in the SEM images for these loadings. $H_2O_2$ is more likely to reduce to $H_2O$ in the presence of nearby active Pt sites when they are packed close together.

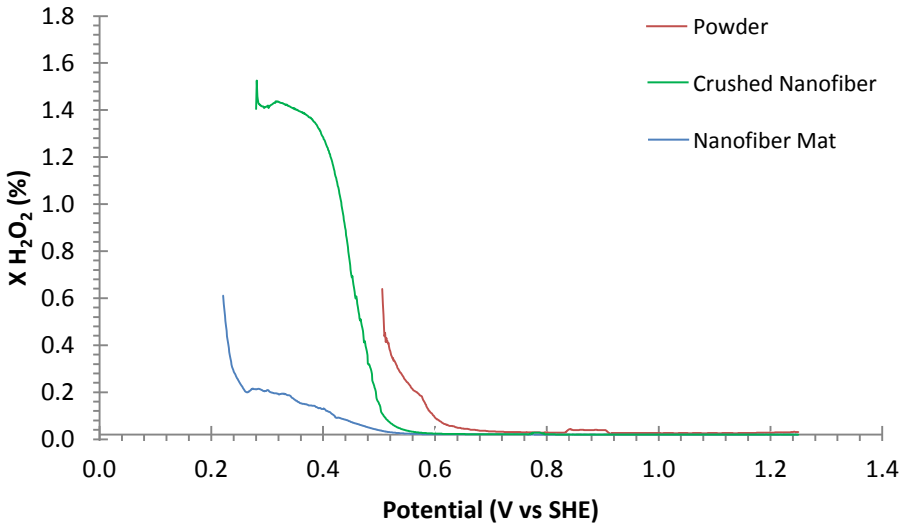


**Figure 55: Percentage formation of hydrogen peroxide for 100µg/cm$^2$ Pt loaded catalysts with different support structures measures in $O_2$ saturated 0.1 M $HClO_4$ solution at 1600 rpm.**

## 5.2.Electrodes Prepared via TICD

### 5.2.1. Physical characterisation of TICD prepared electrodes

#### *5.2.1.1. SEM-EDX for surface morphology and loading analysis*

Catalysts prepared by TICD techniques were analysed via SEM-EDX to determine the loadings of Pt and surface morphology of the catalysts supports. This method was also used to validate the reproducibility of the deposition technique for consistent Pt loadings. Pt loadings for the $TiB_2$ support materials were chosen based on the equivalent v/v% of 20 wt% Pt/C and 40 wt% Pt/C and were calculated to be 8 wt% and 16 wt% respectively.

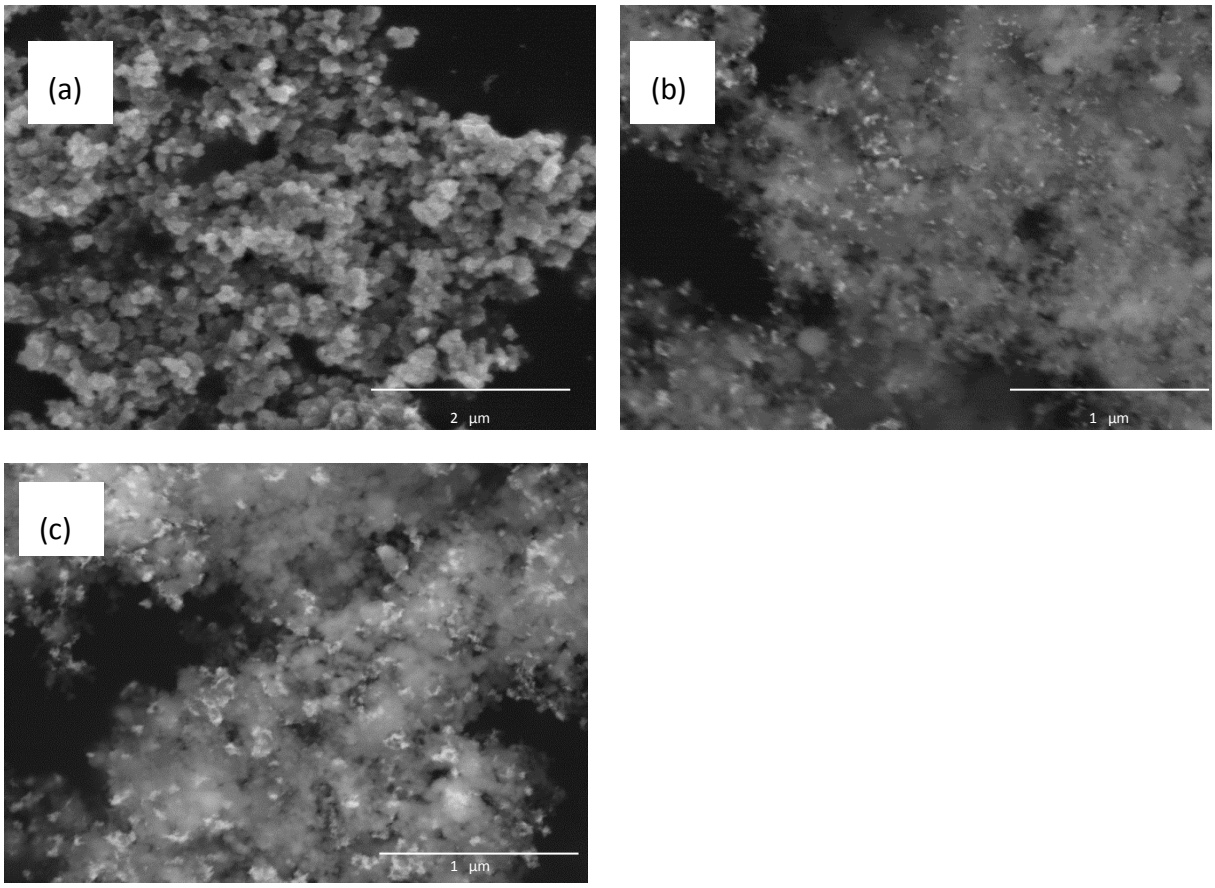


**Figure 56: SEM images of $TiB_2$ powder support structures with (a) being the blank support material and the TICD prepared powder supported catalysts with a platinum loading of (b) 8 wt% and (c) 16 wt%.**

The SEM image in Figure 56 indicates an increase in the Pt loading by the intense white/light grey areas in Figure 56 c. This initial physical characterisation technique validates the successful deposition of platinum onto the powder support structure via TICD. The relevant loadings for the powder analysed via EDX can be found in Table 13. Table 13 shows the average loadings for three samples prepared via identical methods aiming to attain samples of loadings of 8 and 16 wt%.

**Table 14: Pt loading calculations for catalysts prepared via TICD on $TiB_2$ powder supports.**

| Sample | | Loading (%) | | |
|---|---|---|---|---|
| Powder 16 wt% | 1 | 14.7 | | |
| | 2 | 12.2 | Mean | St. Dev |
| | 3 | 15.9 | 14.3 | 1.93 |
| Powder 8 wt% | 1 | 9.6 | | |
| | 2 | 8.5 | Mean | St. Dev |
| | 3 | 9.3 | 9.11 | 0.52 |

The standard deviations for these loadings are relatively low therefore it can be concluded that this method of Pt deposition is a reproducible method.

Crushed nanofiber support materials were characterised by SEM indicating the surface morphology and Pt loaded on the surface of these materials. Figure 57 shows the blank nanofiber and the crushed nanofiber supports with increased loadings.

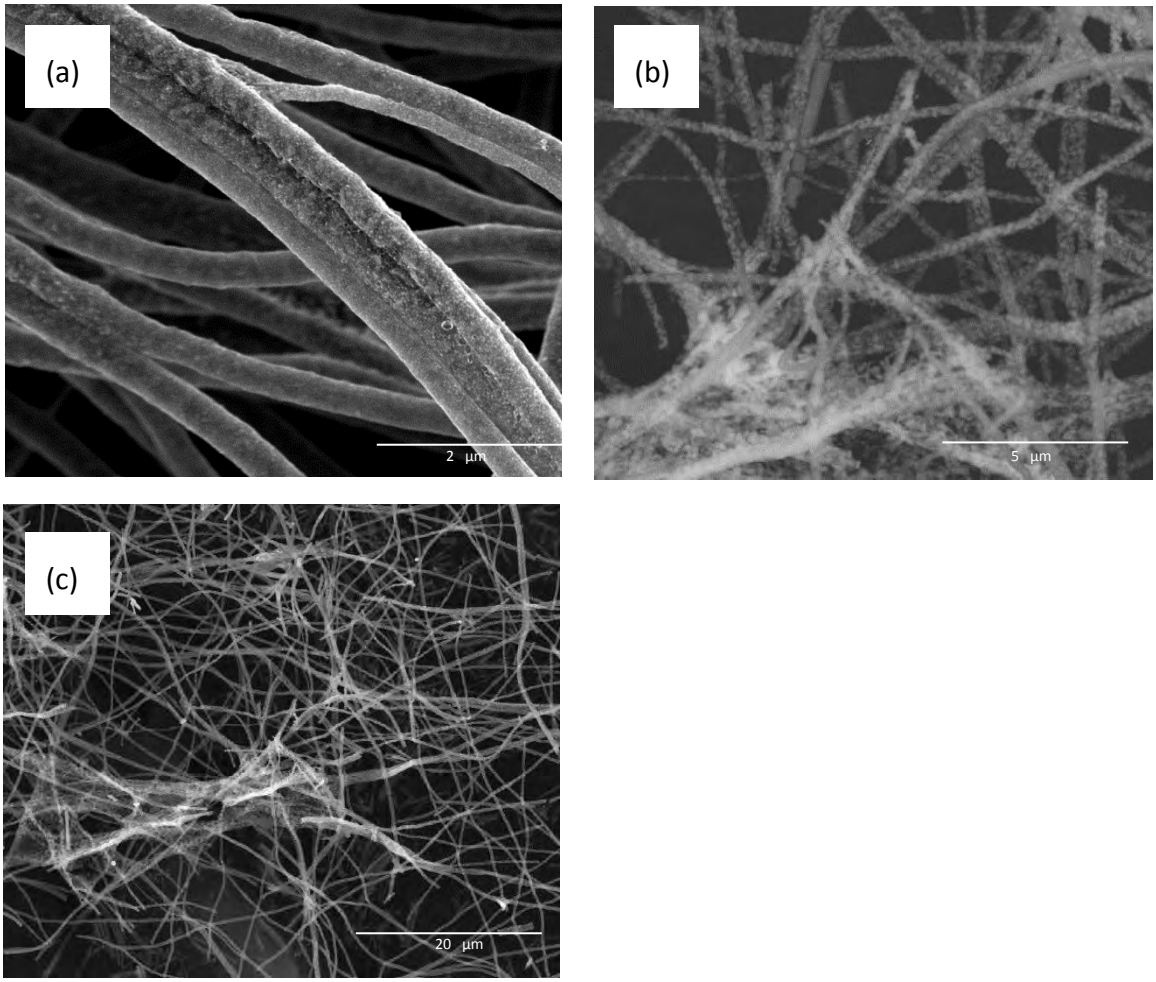


**Figure 57: SEM images of $TiB_2$ crushed nanofiber support structures with (a) being the blank support material and the TICD prepared crushed nanofiber supported catalysts with a platinum loading of (b) 8 wt% and (c) 16 wt%.**

The loadings for the crushed nanofiber were not close to the desired amount for the higher loading. This can be seen in Table 14. It was a challenge attaining the correct loading with these support materials as they are lightweight materials and therefore to achieve a loading lower than 20 wt% proved to be particularly difficult. The different samples do, however, remain within a less than 2 standard deviation which indicated that the procedure is reproducible.

**Table 15: Pt loading calculations for catalysts prepared via TICD on $TiB_2$ CNF supports**

| Sample | | Loading (%) | | |
|---|---|---|---|---|
| CNF 16 wt% | 1 | 20.9 | | |
| | 2 | 23.4 | Mean | St. Dev |
| | 3 | 22.6 | 21.7 | 1.89 |
| CNF 8 wt% | 1 | 4.46 | | |
| | 2 | 7.19 | Mean | St. Dev |
| | 3 | 7.15 | 6.27 | 1.56 |

Nanofiber mats proved to be the most challenging to attain a set Pt loading on since this material weighed 1.3 mg at most for a 2.4 $cm^2$ nanofiber mat. Consequently the corresponding Pt precursor mass was in the range of 0.08 mg which proved to be very difficult to weigh using an analytical balance. However, Figures 58 indicate successful deposition of Pt onto the surface with low Pt loadings as seen in Table 15.

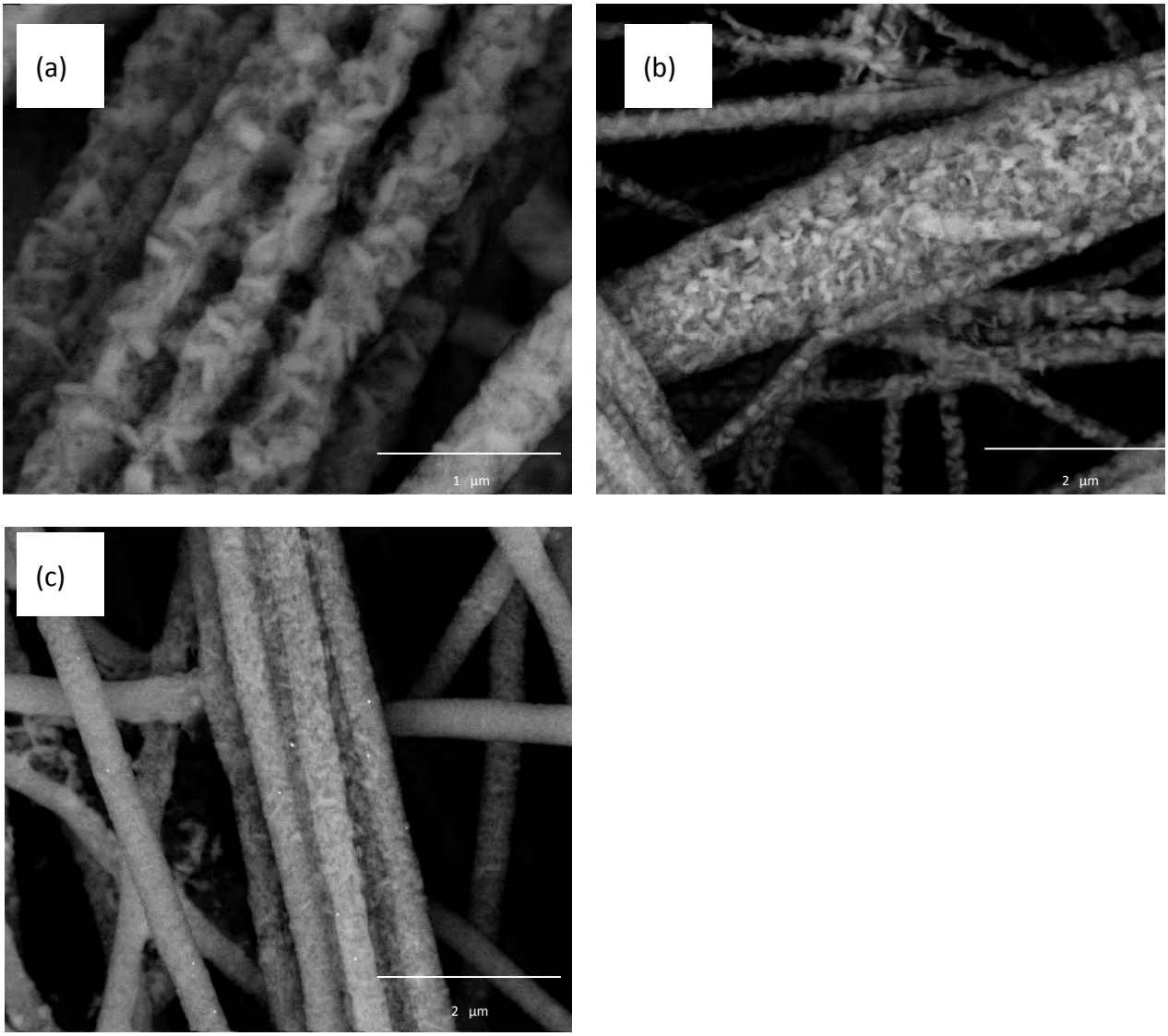


**Figure 58: SEM images of $TiB_2$ nanofiber mat support structures with (a) being the blank support material and the TICD prepared nanofiber mat supported catalysts with a desired platinum loading of (b) 8 wt% and (c) 16 wt%.**

Table 15 shows that on average the desired Pt loadings were achieved however, NF mats showed the largest standard deviation between the different samples which is as a result of the challenges experienced with the low mass of the fiber mats. A potential solution is to deposit Pt on much larger nanofibers mats. However the current cost of these mats, as they are in a development stage, is too high for that route to be feasible for this work.

**Table 16: Pt loading calculations for catalysts prepared via TICD on $TiB_2$ NF supports**

| Sample | | Loading (%) | | |
|---|---|---|---|---|
| CNF 16 wt% | 1 | 17.6 | | |
| | 2 | 13.263 | Mean | St. Dev |
| | 3 | 18.4 | 16.4 | 2.77 |
| CNF 8 wt% | 1 | 6.66 | | |
| | 2 | 10.6 | Mean | St. Dev |
| | 3 | 6.13 | 7.80 | 2.46 |

### *5.2.1.2. TEM analysis for Pt particle size and distribution*

TEM analysis of the different support structures was conducted to evaluate Pt particle size and Pt distribution on the surface of the support materials. The powder was analysed and can be seen in Figure 59 for the various Pt loadings. The corresponding Pt particle size analysis can also be seen in the image.

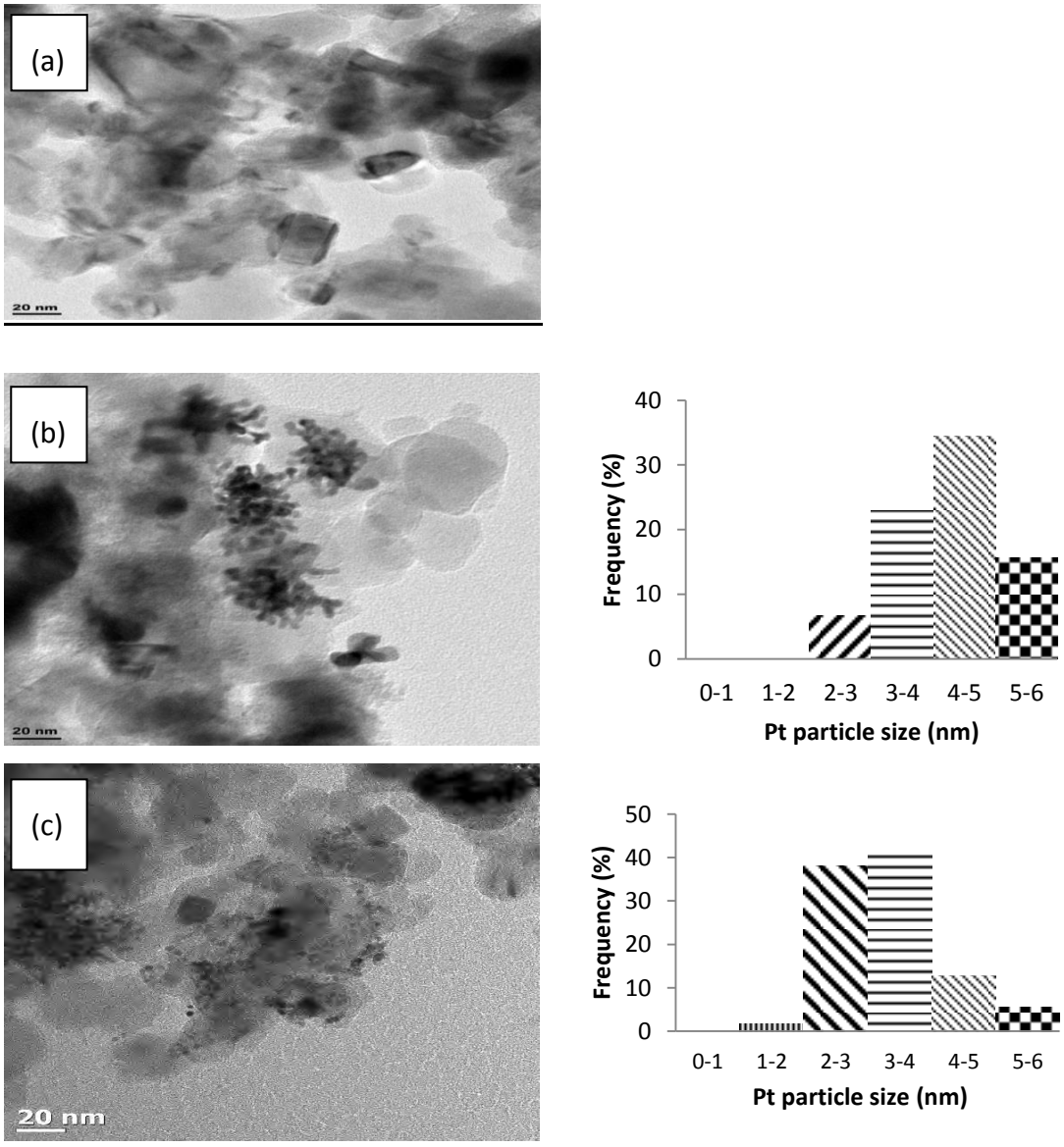


**Figure 59: TEM images of $TiB_2$ powder support structures with (a) being the blank support material and the TICD prepared powder supported catalysts with a desired platinum loading of (b) 8 wt% with its corresponding Pt particle size analysis and (c) 16wt% with its corresponding Pt particle size analysis.**

The TEM images of the powder indicate an increase in Pt density over the area as the platinum loading is increased. Figure 59 b indicates Pt agglomerates on the $TiB_2$ nanoparticles. There is not a homogenous distribution of Pt covering the surface of the support. Instead, blank areas of powder can be seen in both the 8 and 16 wt% loadings. The Pt particle size analyses validate the occurrence of larger Pt particles, most likely caused by agglomeration by an increase in the frequency of Pt particles ranging between 4 and 6 nm. The Pt clusters seem to favour certain sites/areas on the support particles. An attempt to address this by surface treatment was undertaken and is discussed further in Section 5.2.2.

Platinum deposited on the nanostructured support materials are presented in Figure 60. Since the crushed fibre, in essence, will be treated like a powder support we would expect a degree of Pt agglomeration on this surface too. However, the favourable nanostructure of this materials and its affinity towards Pt results in a better distribution of Pt on the surface.

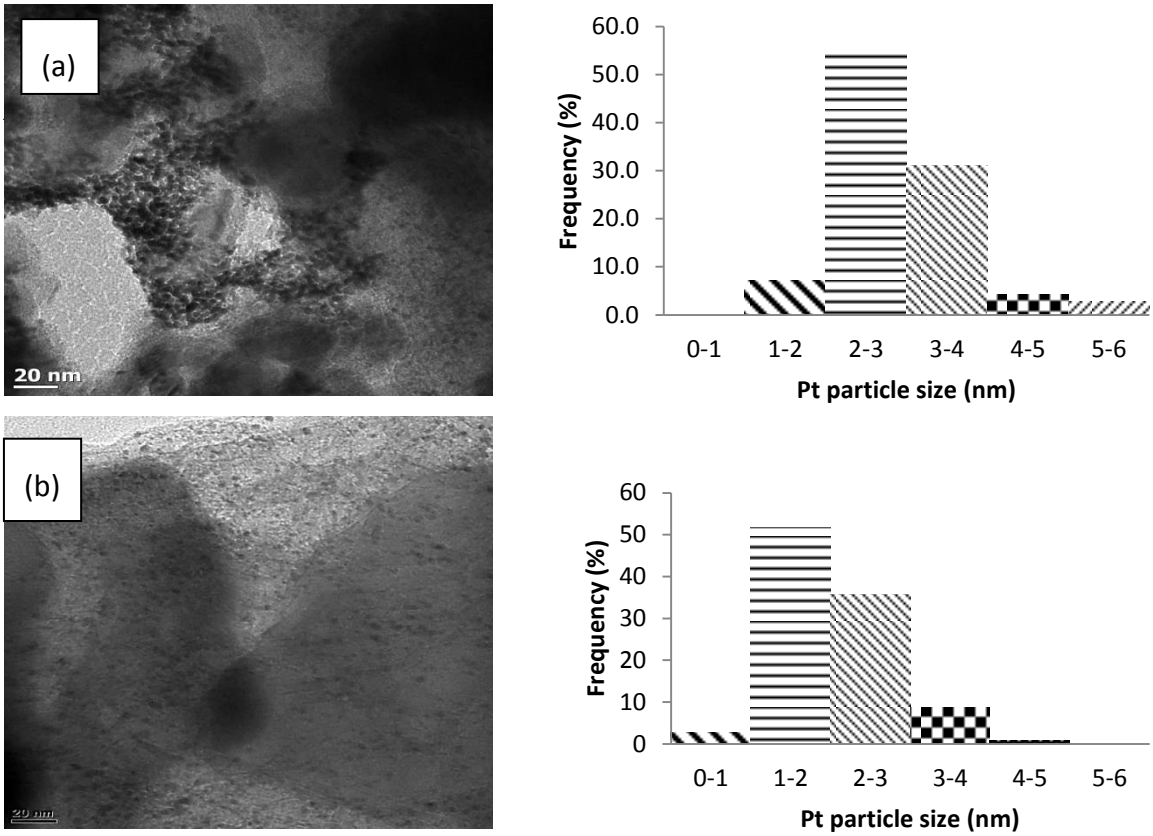


**Figure 60: TEM images of $TiB_2$ crushed nanofiber supported catalysts prepared via TICD with a desired platinum loading of (a) 8 wt% with its corresponding Pt particle size analysis and (b) 16 wt% with its corresponding Pt particle size analysis.**

In comparing the higher and lower loadings of Pt on the CNF surface, it can be seen that Pt clump together in the corners or edges of the crushed nanofibers. Because of the nanofiber structure, less of these corners and edges are present as compared to the powder therefore the degree of clumping is to a lesser extent than seen in the powder. In the crushed nanofibers case we clearly observe Pt nanoparticles in the surrounding nanofibers. Therefore there are no blank areas of the nanofibers. There is a good distribution of Pt on the surface of the CNF material with isolated Pt particles seen in Figure 60. The Pt size analysis indicated very small Pt particles in the range of 1 - 3 nm.

The blank nanofiber TEM image is the same whether it is crushed or not since the nanofiber is placed in suspension regardless. Figure 61 illustrates the blank nanofiber and the nanofiber mat supported catalysts prepared via TICD.

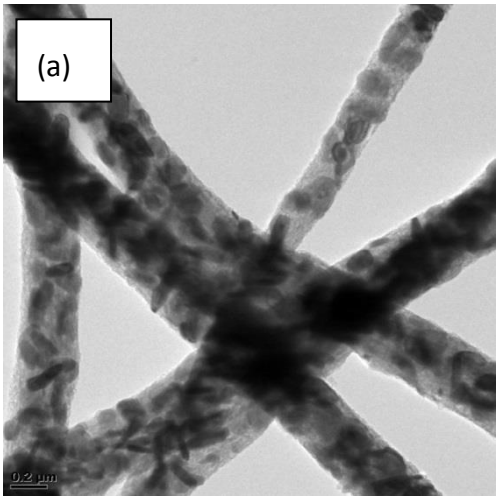


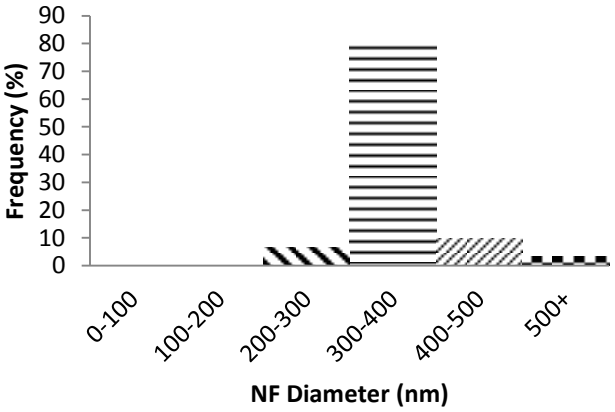


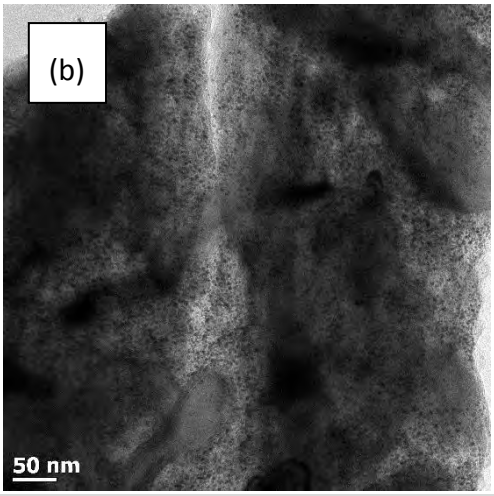


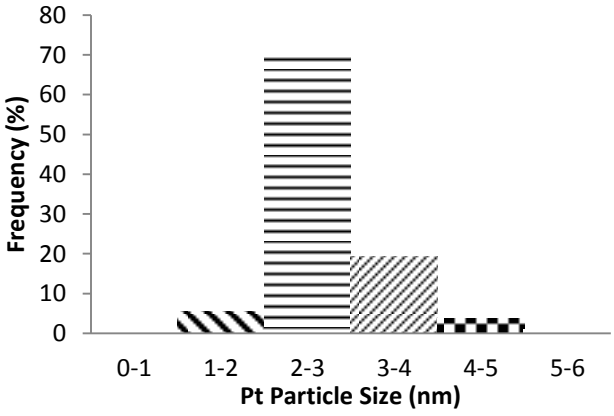

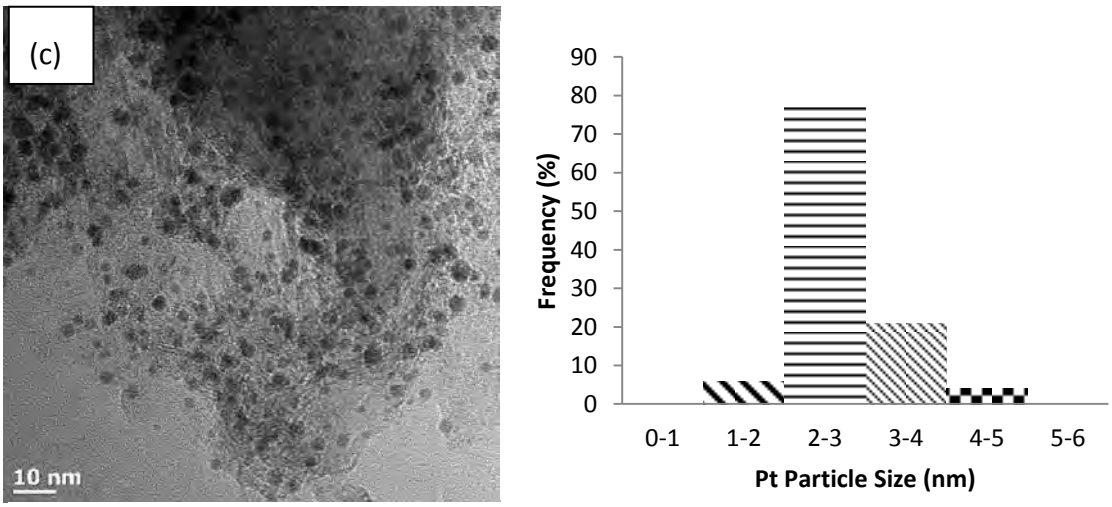


**Figure 61: TEM images of $TiB_2$ NF support structures with (a) being the blank support material and the TICD prepared NF supported catalysts with a desired platinum loading of (b) 8 wt% with its corresponding Pt particle size analysis and (c) 16 wt% with its corresponding Pt particle size analysis**

Pt is homogenously distributed on the nanofiber mat support materials even when the Pt loading is increased. This indicates that the surface of the nanofibers is fairly uniform in terms of binding sites for the Pt. Figure 61 b, shows an increase in the amount of Pt on the nanofiber surface however there are no clumps or agglomerates formed. This is also true in low Pt loadings as isolated Pt particles are also seen on the low loaded nanofiber mat of particle size range of 2-3 nm.

#### *5.2.1.3. XRD trends for the $TiB_2$ catalysts*

XRD analysis was conducted for each catalyst prepared via TICD at the various Pt loadings. The results of these analyses are given in Figure 62 for powder, Figure 63 for crushed nanofiber and Figure 64 for nanofiber mat.

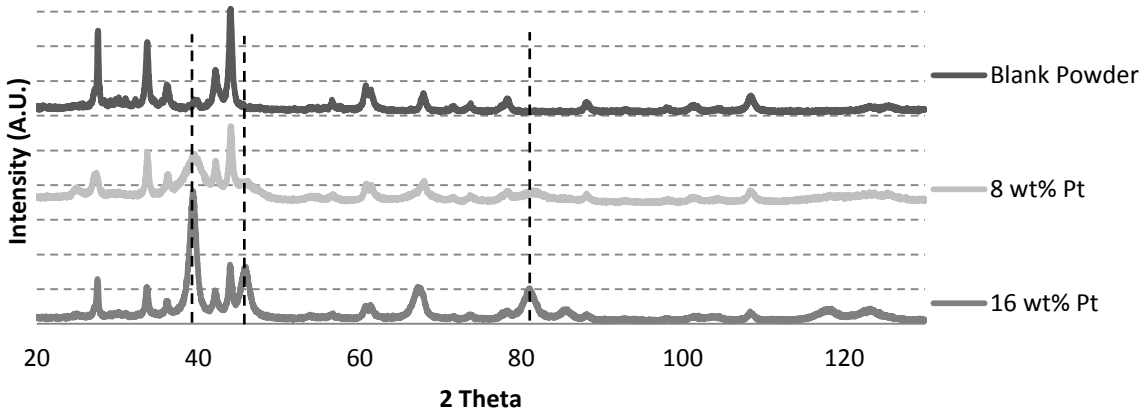


**Figure 62: XRD trends for blank $TiB_2$ powder and the catalysts prepared via TICD with a Pt loading of 8 and 16 wt%.**

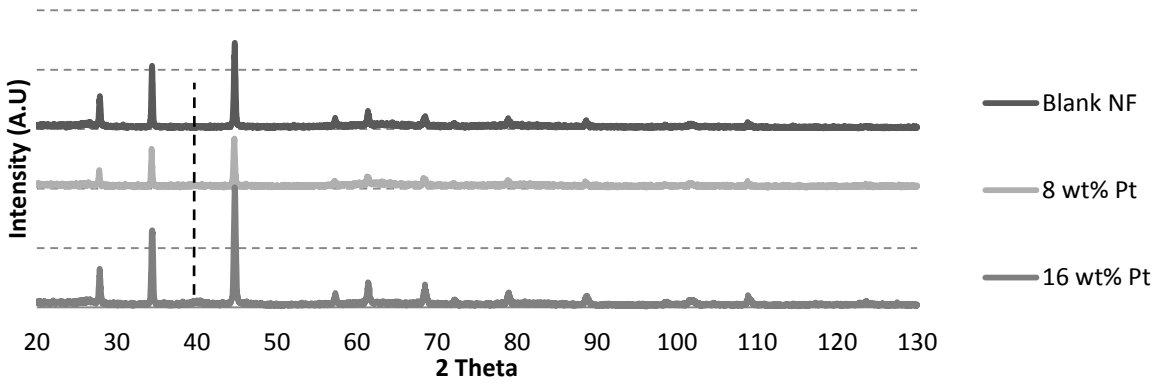


**Figure 63: XRD trends for blank $TiB_2$ CNF, and the catalysts prepared via TICD with a Pt loading of 8 and 16 wt%.**

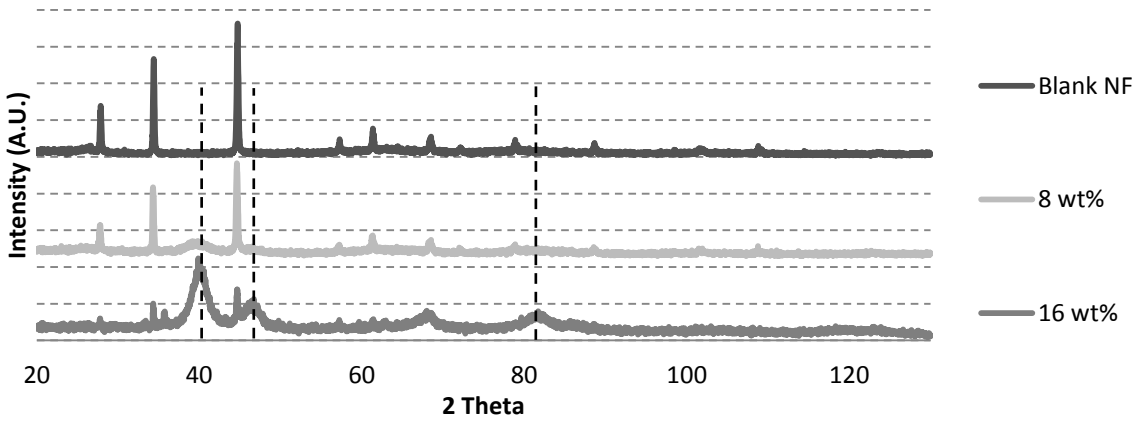


**Figure 64: XRD trends for blank $TiB_2$ NF mat, and the catalysts prepared via TICD with a Pt loading of 8 and 16 wt%.**

Figures 62 to 64 all indicate Pt (111) at roughly 40° and Pt (200) at roughly 50°. Higher Pt loadings indicate a broader and more intense peak as a result of an increase in particle size and agglomerates with increased loadings. Crushed nanofiber samples have very small Pt (111) peaks only and look almost identical to that of the base NF reading. The Scherrer Equation was used to calculate the Pt particle sizes in Table 16 are found to be in the range of the sizes found for TEM analysis.

**Table 17: Average Pt crystallite size analysis using XRD Pt peaks and the Scherrer equation for $TiB_2$ catalysts prepared by TICD.**

| $TiB_2$ support structure | Pt particle size (nm) |
|---|---|
| **Powder** | 5.7 |
| **CNF** | 3.7 |
| **NF** | 2.9 |

### 5.2.2. Improvement of Pt distribution on Powder via surface functionalisation

Surface functionalisation or treatment was applied in an attempt to reduce the severe platinum agglomeration seen via TEM and SEM on the powder support materials. Many research groups have looked into functionalisation of various carbon structures using acid treatment ($HNO_3$, $H_2SO_4$) at different concentrations, reaction times and temperatures (Chiang, et al., 2011), (Naseh, et al., 2009) and (Jiang , et al., 2007). The methods chosen were an acid treatment under reflux with hydrogen peroxide, sulphuric acid and nitric acid at 80°C. A dry method of surface treatment was also conducted via temperature programmed reduction (TPR). This was carried out by exposing the powder support material to a reducing environment of $H_2$/Ar gas flow at 500 °C for 4 hours. Both methods were found to be unsuccessful in reducing the Pt agglomeration. The acid treatment caused the $TiB_2$ to react and form a different compound of Ti-oxides. The acid and $TiB_2$ solution after

acid treatment seen in Figure 65 shows the loss in $TiB_2$ material as the solution changed from black to a yellow colour.

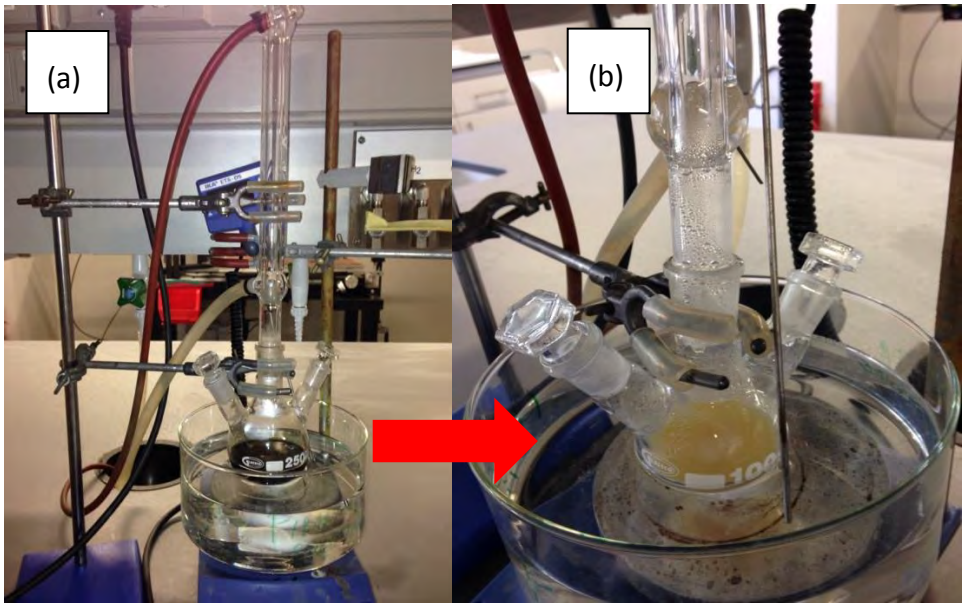


**Figure 65: $TiB_2$ in solution (a) before and (b) after acid treatment at 80 °C in an attempt to functionalise the surface with the addition of oxygen groups to the surface for Pt anchorage.**

Pt was deposited via TICD on the powder after TPR and the results can be seen in Figure 66.

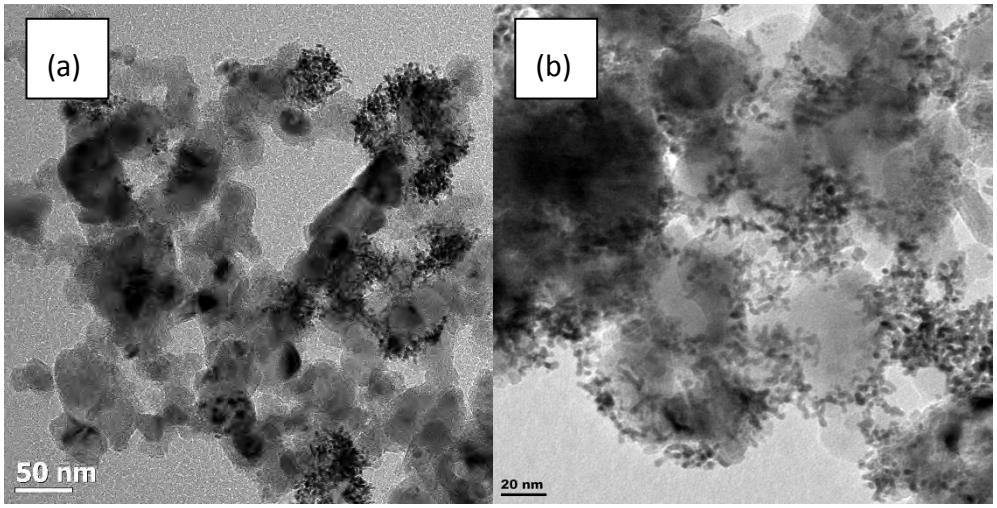


**Figure 66: TEM images of Pt deposited on $TiB_2$ powders before (a) and after (b) TGA.**

Figure 66 b shows a slight improvement in the Pt dispersion as there are fewer blank support areas, however there is still a large degree of agglomeration of the Pt and therefore

this method was not applied to the other supports. Further investigation into this could be done into a broader range of very controlled surface treatments, however this was not in the scope of my research.

### 5.2.3. Electrochemical characterisation of TICD prepared electrodes

#### *5.2.3.1. Electrochemical surface area evaluation of TICD prepared electrodes*

ECSA was determined for each catalyst prepared by the TICD method for different loadings. As discussed before in Section 3.1.2 the $H_{upd}$ with a CO baseline correction was adapted to determine the ECSA. The cyclic voltammograms for the 8 wt% and 16 wt% loadings on each support system are shown below as illustration with a summary of all ECSA values obtained in Table 17.

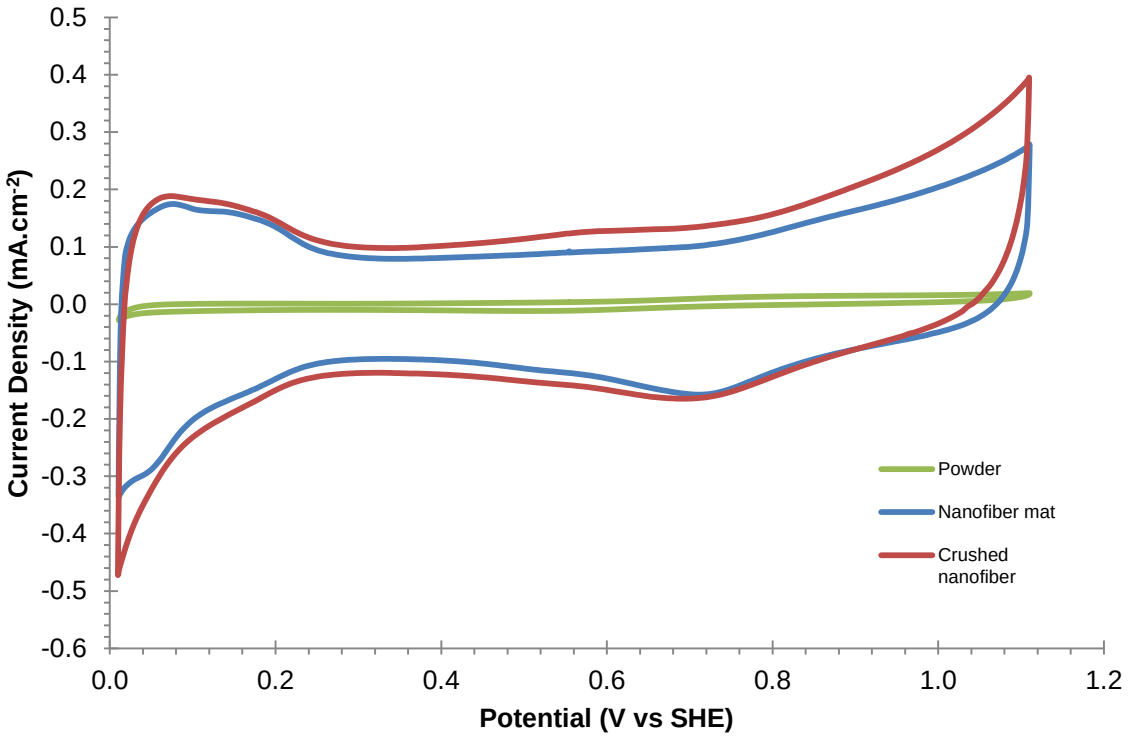


**Figure 67: Cyclic voltammogram recorded for each support structure based catalyst of Pt loading 8wt% recorded in Ar saturated 0.1 M $HClO_4$ electrolyte at room temperature.**

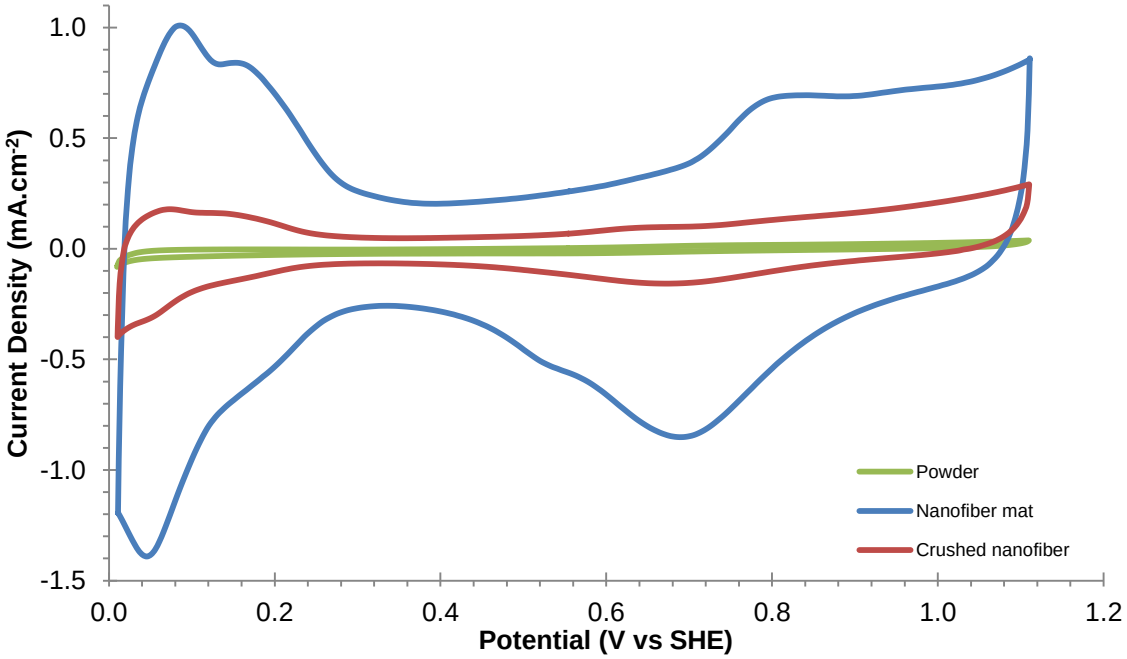


**Figure 68: Cyclic voltammogram recorded for each support structure based catalyst of Pt loading 16wt% recorded in Ar saturated 0.1 M $HClO_4$ electrolyte at room temperature.**

Figures 67 and 68 both indicate superior electrochemical surface area for the nanofiber based catalysts. Nanofiber mat loaded with 16 wt% Pt indicates clear H desorption peaks on Pt surfaces. Table 17 indicates a summary of the ECSA values for the TICD prepared catalysts with different support materials.

**Table 18: ECSA values for the Pt catalysts prepared via TICD measured using cyclic voltammetry in a 0.1 M $HClO_4$ electrolyte solution at room temperature.**

| | ECSA ($m^2/g_{Pt}$) | |
|---|---|---|
| **Catalyst support type** | **16wt% Pt Loading** | **8wt% Pt Loading** |
| **Powder** | 0.51 | 0.32 |
| **CNF** | 6.9 | 1.5 |
| **NF** | 68 | 10 |

There is a distinct increase in $H_{upd}$ and double layers of the nanofiber materials. This can be explained by the fiber morphology, inter fiber and intra fiber pores leading to greater electrochemical surface area accessible to platinum as well as excellent ionomer distribution within the fibers. The powder displayed little to no evident $H_{upd}$ under these conditions. The

ECSA of the nanofiber mat far surpasses that of the crushed nanofiber and powder supports. Since the mat is light weight, the loading of Pt on the electrode is less than both the CNF and powder samples therefore when calculating ECSA, the large charge under the integrated area is caused by a fraction of the Pt in the CNF sample. There is a peak in the oxidation region indicating that there could be an oxidation of the support material occurring in this environment.

When considering the ECSA values obtained for the different support systems it is clear that the nanofiber mat is in all cases the superior structure. We also observed that the ECSA values are higher for the higher loadings which are, when comparing to typical Pt/C catalysts, unexpected. It is speculated that on these less conductive support materials a certain minimum metal loading needs to be present to compensate for the low conductivity.

The very low surface area measured for the powder support could be due to the low conductivity of the $TiB_2$ in powder form. To verify this, 20wt% acetylene black was added to the inks of these support materials in an attempt to improve the overall conductivity. The cyclic voltammograms for each support structure are presented below. Herein the comparison of the Pt loading and C addition can be seen.

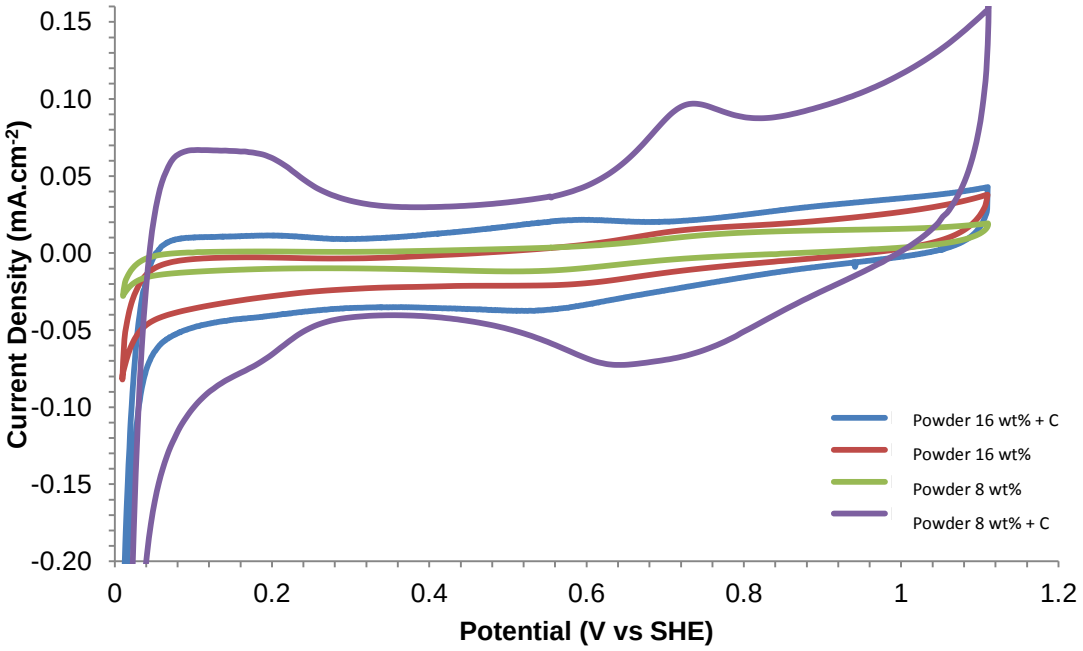


**Figure 69: Cyclic Voltammogram of Pt deposited on $TiB_2$ powder support with a high loading (16 wt%) and a low loading (8 wt%) recorded in an Ar saturated 0.1 M $HClO_4$ electrolyte solution at room temperature. Curves for the catalyst ink prepared with an additional 20 wt% AB are also indicated for each Pt loading.**

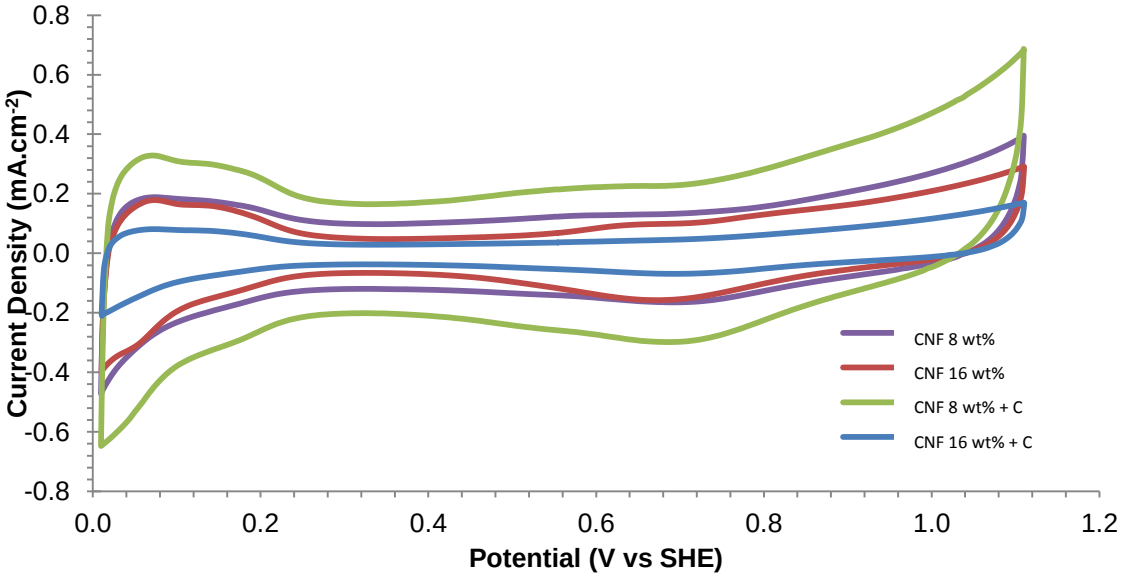


**Figure 70: Cyclic Voltammogram of Pt deposited on $TiB_2$ CNF support with a high loading (16wt%) and a low loading (8wt%) recorded in an Ar saturated 0.1 M $HClO_4$ electrolyte solution at room temperature. Curves for the catalyst ink prepared with an additional 20wt % AB are also indicated for each Pt loading.**

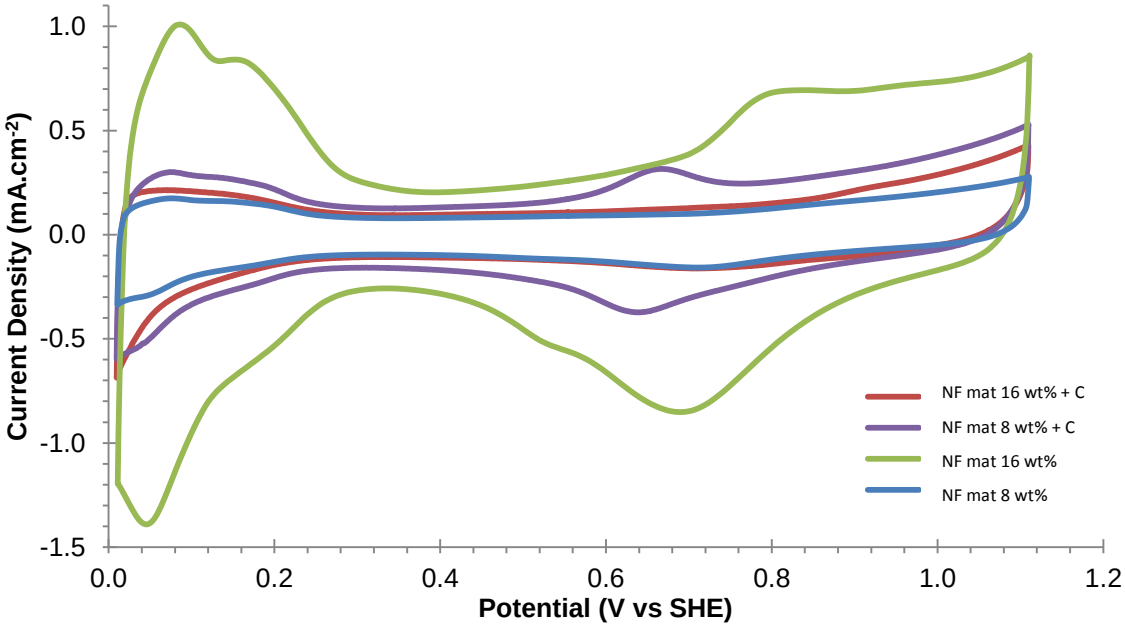


**Figure 71: Cyclic Voltammogram of Pt deposited on TiB2 NF mat support with a high loading (16wt%) and a low loading (8wt%) recorded in an Ar saturated 0.1 M $HClO_4$ electrolyte solution at room temperature. Curves for the catalyst ink prepared with an additional 20wt % AB are also indicated for each Pt loading.**

The addition of carbon has vastly improved the performance and conductivity of the powdered material. ECSA improved by a factor of 10 for the 8 wt% Pt loading. Table 18 shows the ECSA normalised for the mass of Pt on each catalyst.

**Table 19: ECSA values for the Pt catalysts prepared via TICD with the addition of AB measured using cyclic voltammetry in a 0.1 M $HClO_4$ electrolyte solution at room temperature.**

| | ECSA ($m^2/g_{Pt}$) | |
|---|---|---|
| **Catalyst support type** | **16wt% Pt Loading** | **8wt% Pt Loading** |
| **Powder + AB** | 0.5 | 1.7 |
| **CNF + AB** | 1.5 | 14.8 |
| **NF + AB** | 38 | 41 |

The addition of AB improves the conduction of electrons in the powder supported catalyst which can be seen by the improved $H_{upd}$ peaks. The low loaded support shows greater ECSA which could be as a result of the higher degree of isolated Pt particle than in the higher loading. Through the addition of AB, more active Pt sites are reached. The curves for the crushed nanofibers and Tables 17 and 18 indicate that the addition of carbon does not

entirely improve its ECSA. In fact, 16wt% Pt loaded CNF displays the smallest curve and lowest ECSA. When carbon is added to the catalyst ink, it takes the place of the Pt catalyst when deposited on the electrode. The CNF has a lower density and therefore will cover a smaller surface area when mixed in an ink. Therefore by adding the AB one is effectively reducing the amount of catalyst deposited on the electrode.

The nanofiber support materials display a larger ECSA when compared to the other support structures. This is as a result of the continuous nanofiber strands available for Pt deposition. The isolated Pt particles shown in TEM indicate that there are more available active sites of Pt. There is no observed increase in the ECSA with the addition of C which could be because C might block the active Pt sites on the nanofiber materials.

### 5.2.4. Electrochemical activity of TICD prepared electrodes

Linear sweep voltammetry was conducted to determine the oxygen reduction reaction (ORR) activity of each support structure at different Pt loadings. In a first set the electrodes were prepared with $TiB_2$ materials only. In a second set of experiments carbon black was added into the film to exclude conductivity effects.

#### *5.2.4.1. Measurements on pure $TiB_2$ support*

RDE results for each support structure at Pt loading of 8 wt% and 16 wt% recorded at 1600 rpm are shown in Figure 72 and Figure 73 respectively. Kinetic current densities ($i_k$), intrinsic and mass activities at 0.9 V vs SHE where extracted from the data and are presented in Table 19.

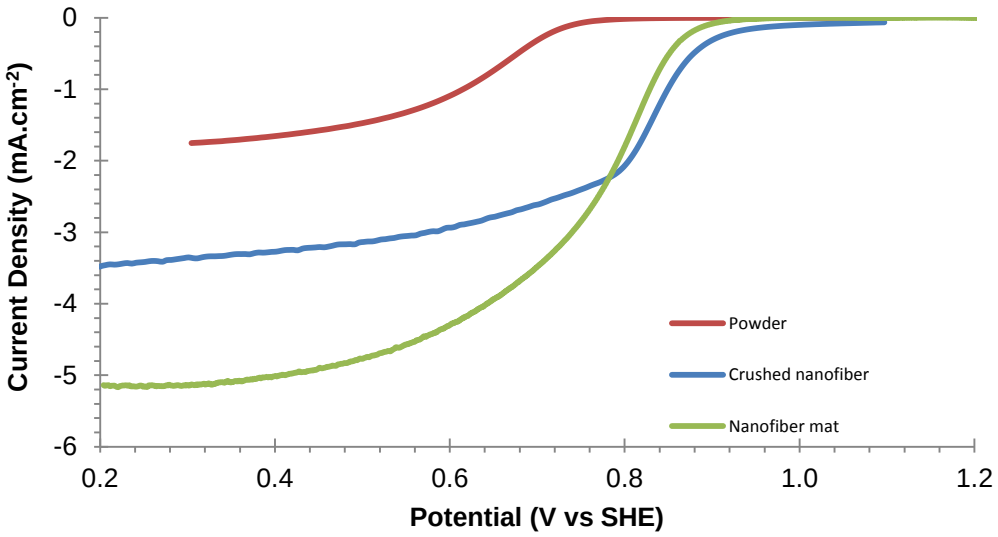


**Figure 72: Oxygen reduction current densities for the cathodic peaks of 8 wt% loaded support structures measures in $O_2$ saturated 0.1 M $HClO_4$ electrolyte at 1600 rpm and 20 mV/s.**

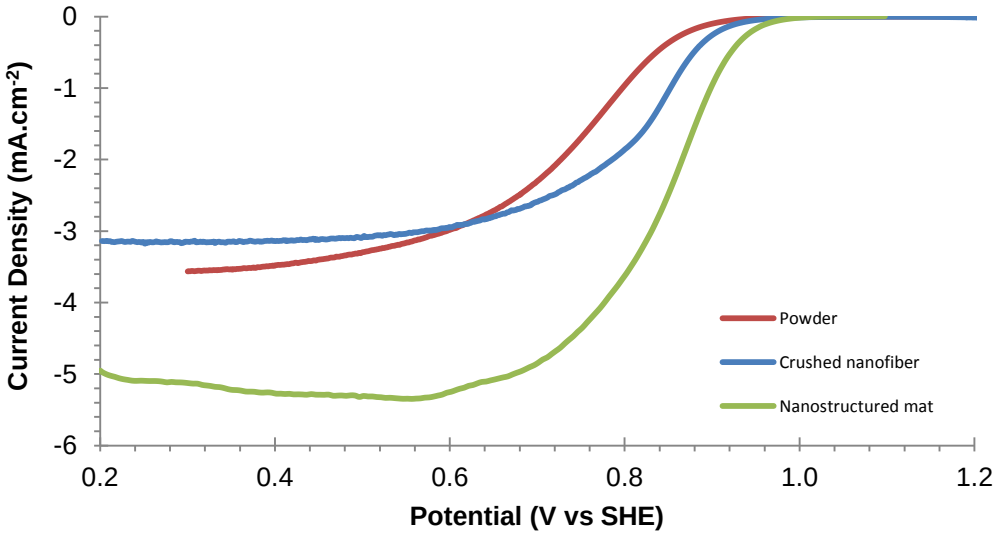


**Figure 73: Oxygen reduction current densities for the cathodic peaks of 16 wt% loaded support structures measures in $O_2$ saturated 0.1 M $HClO_4$ electrolyte at 1600 rpm and 20 mV/s.**

Nanofiber mats show a higher onset potential indicating its higher reaction kinetics. This support also reaches close to the theoretical limiting current. Both crushed nanofiber and powder do not reach this theoretical value which from the slope in the mixed region seems

to stem from severe ohmic losses due to high resistance in the electrode. The intrinsic and mas specific activity for the catalysts prepared are summarised in Table 19 below.

**Table 20: Intrinsic and mass specific activity of $TiB_2$ powder, crushed nanofiber and nanofiber mats observed at 0.9 V vs SHE and 1600 rpm for two Pt loadings.**

| Support Type | Intrinsic Activity ($mA/cm^2_{Pt}$) | Mass Specific Activity ($mA/g_{Pt}$) |
|---|---|---|
| **16 wt% Pt supported on:** | | |
| Powder | 0.61 | 3.15 |
| Crushed Nanofiber | 0.01 | 0.90 |
| Nanofiber Mat | 0.01 | 8.50 |
| **8 wt% Pt supported on:** | | |
| Powder | 0.03 | 0.12 |
| Crushed Nanofiber | 0.14 | 2.02 |
| Nanofiber Mat | 0.04 | 13.5 |

$TiB_2$ nanofibers display higher mass specific activities than the other support materials. In the case of the 16 wt% Pt loaded powder catalysts, higher intrinsic activity was observed, with no change in the intrinsic activity of this nanofiber materials. These values are normalised for the electrochemical surface area of the material per mass of Pt on the surface. With the powdered samples displaying very low ECSA, this high activity is expected.

In order to compensate the resistance and analyse the data reliably, acetylene black was added to the catalysts with the aim of improving the overall conductivity of these supports. The results for each support structure with 8 wt% and 16 wt% Pt with and without carbon follow.

### *5.2.4.2. Studies with carbon added to the electrode*

#### 5.2.4.2.1. Powder

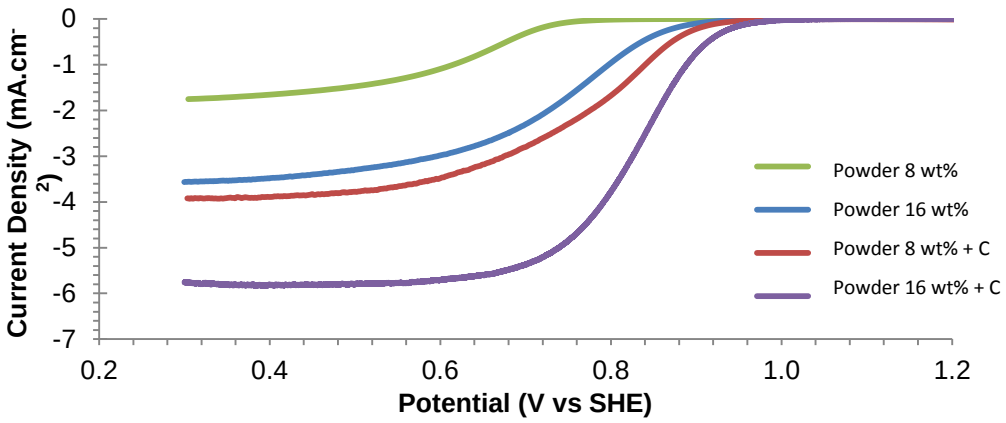


**Figure 74: Oxygen reduction current densities for the cathodic peaks of high (16wt%) and low (8wt%) Pt loaded $TiB_2$ powder support structures with AB measured in $O_2$ saturated 0.1 M $HClO_4$ electrolyte at 1600 rpm and 20 mV/s.**

The addition of carbon to the powder catalyst vastly improves the results obtained for the onset potential and the general profile of the LSV curves. The conductivity of the catalysts was improved. The mass specific and intrinsic activity results are summarised in Table 20.

#### 5.2.4.2.2. Crushed nanofiber

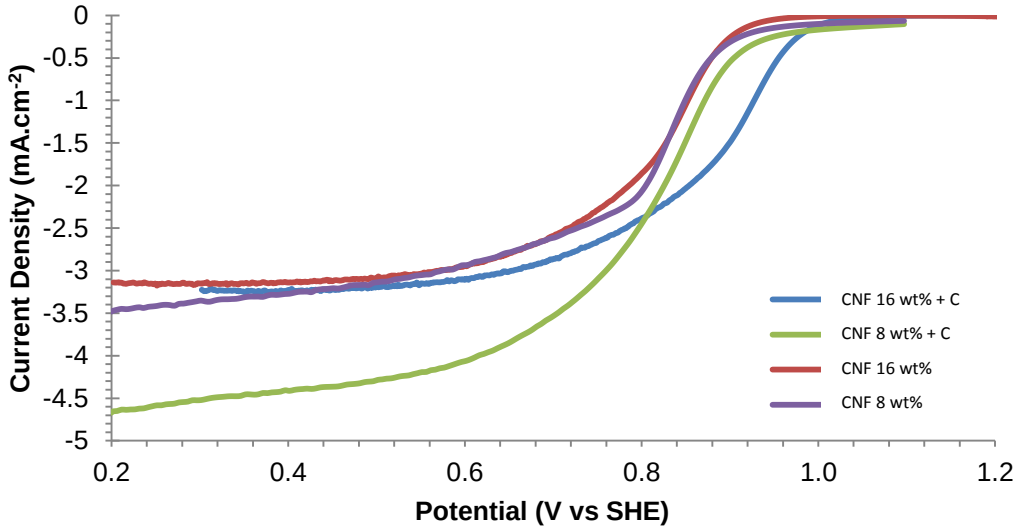


**Figure 75: Oxygen reduction current densities for the cathodic peaks of high (16 wt%) and low (8wt%) Pt loaded $TiB_2$ powder support structures with AB measured in $O_2$ saturated 0.1 M $HClO_4$ electrolyte at 1600 rpm and 20 mV/s**

There is no significant change in the diffusion limiting current density between the 16 wt% Pt/crushed nanofiber with or without carbon. Some improvement is seen for the 8 wt% loaded CNF catalyst, however the diffusion limited current is still far of the theoretical value. This is also apparent from the low activity values listed in the Table 20.

#### 5.2.4.2.3. Nanofiber mat

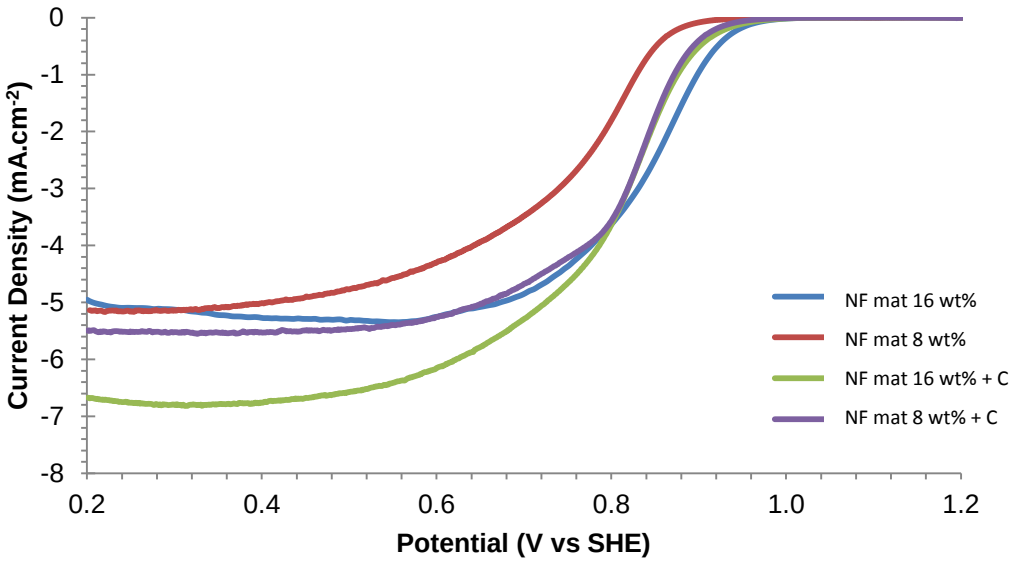


**Figure 76: Oxygen reduction current densities for the cathodic peaks of high (16 wt%) and low (8 wt%) Pt loaded $TiB_2$ NF mat support structures with AB measured in $O_2$ saturated 0.1 M $HClO_4$ electrolyte at 1600 rpm and 20 mV/s**

The nanofiber catalysts all reach close to theoretical diffusion limiting currents. The 16 wt% loaded NF with carbon has a slightly higher limiting current than the theoretical value. The reason for this could not be fully determined but it might be related to the normalisation to current density not being entirely accurate for these more complex nanostructures as discussed earlier (section 5.1.3). The summary for the overall activity with increasing Pt loading and carbon addition are given in Table 20.

Carbon addition to the nanofiber mats shows a clear improvement for the 16 wt% catalyst but not for the 8 wt% system. As with the other structures this results seems to confirm that there is a clear difference in the active surface present at the two loadings.

#### 5.2.4.2.4. Summary of activity testing

Table 20 below summarises the intrinsic and mass specific activities for the catalysts prepared via TICD for the different support structures.

**Table 21: Intrinsic and mass specific activity of $TiB_2$ powder, crushed nanofiber and nanofiber mats plus the addition of acetylene black observed at 0.9 V vs SHE and 1600 rpm for two Pt loadings.**

| Support Type | Intrinsic Activity ($mA/cm^2_{Pt}$) | Mass Specific Activity ($mA/g_{Pt}$) |
|---|---|---|
| **16 wt% Pt supported on:** | | |
| Powder + AB | 5.88 | 26.7 |
| Crushed Nanofiber + AB | 0.29 | 8.90 |
| Nanofiber Mat + AB | 0.06 | 42.0 |
| **8 wt% Pt supported on:** | | |
| Powder + AB | 0.12 | 2.03 |
| Crushed Nanofiber + AB | 0.25 | 3.90 |
| Nanofiber Mat + AB | 0.11 | 10.7 |

Overall both mass and intrinsic activities increase with the addition of C proving the high resistance of the $TiB_2$ material. The intrinsic activity increases with an increase in Pt loading indicating a change in surface properties as the loading increases. The mass activities do not follow trend as they increase with increasing Pt loading. This proves that the higher Pt loadings have greater overall kinetics than the low Pt loadings.

Overall the results for the CNF system with and without carbon added seem to suggest that compared to the powdered system the particular structure of the crushed nanofibers does not lead to intimate contact with the carbon when added as it does do in case of the powder.

Nanofiber supported catalysts display superior performance with and without the addition of carbon. With an increase in loading and carbon addition the mass specific activity reached 42 $mA/g_{Pt}$ which is the highest performing catalyst investigated in this study. The ECSA of this material had also proven to be superior to the other supported catalysts with the maximum value attained being 68 $m^2/g_{Pt}$. These values are comparable to Pt/C catalysts.

### *5.2.4.3. RRDE results for hydrogen peroxide formation*

Figure 77 illustrates the RRDE results for hydrogen peroxide formation obtained for the TICD catalysts with different support structures and a Pt loading of 16 wt%. The curves provide both detail on the current of the Pt ring and disk over the same time. The ring is held at 1.2 V vs SHE and the change in current over time is the contribution of hydrogen peroxide formation.

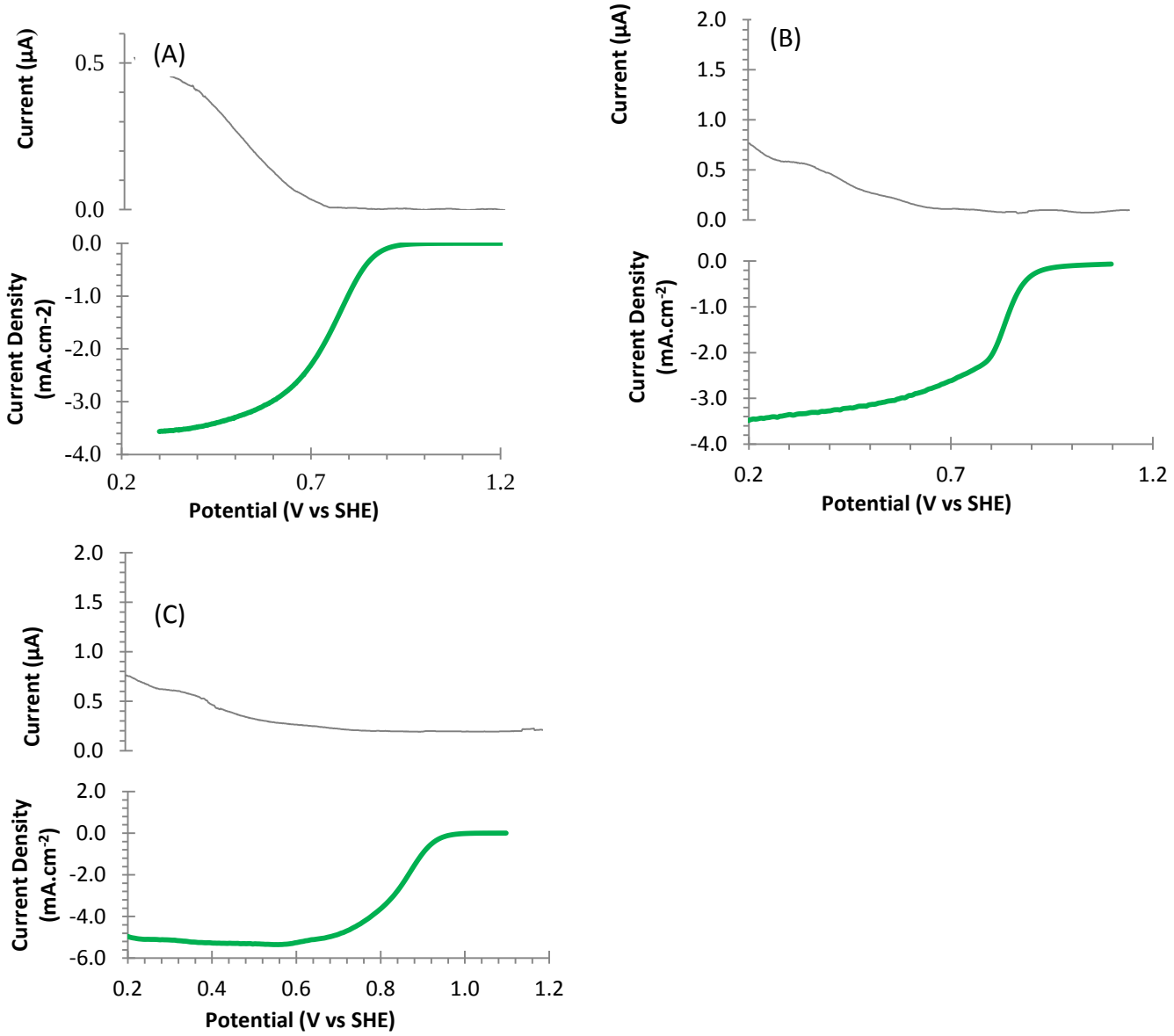


**Figure 77: RRDE hydrodynamic voltammograms for ORR of 16 wt% Pt on (A) powder, (B) crushed nanofiber and (C) nanofiber mat supports in an oxygen saturated, 0.1 M $HClO_4$ electrolyte at room temperature at 1600 rpm. The Pt ring electrode was held at 1.2 V vs SHE and its current caused by $H_2O_2$ formation can be seen in the grey curve. The ORR current of the Pt sputtered disk electrode can be seen in the green curve.**

$H_2O_2$ formation can be observed through the increase in ring current below potential of 0.8 V. The nanostructured supports show an increase in ring potential at a lower potential than for the powder material however, it reaches a higher max than seen for the powder. This shows that more $H_2O_2$ is formed on the nanofiber support catalyst. This is validated by the higher percentage of $H_2O_2$ formation seen in Figure 78. Nanofiber mats produce the highest percentage of peroxide. The number of electrons was calculated to gain an idea of the reaction pathway for each catalyst formed and all supports result in a 4 electron reaction pathway. This is true as the $H_2O_2$ production is insignificant therefore the overall reaction pathway cannot be a 2 electron pathway.

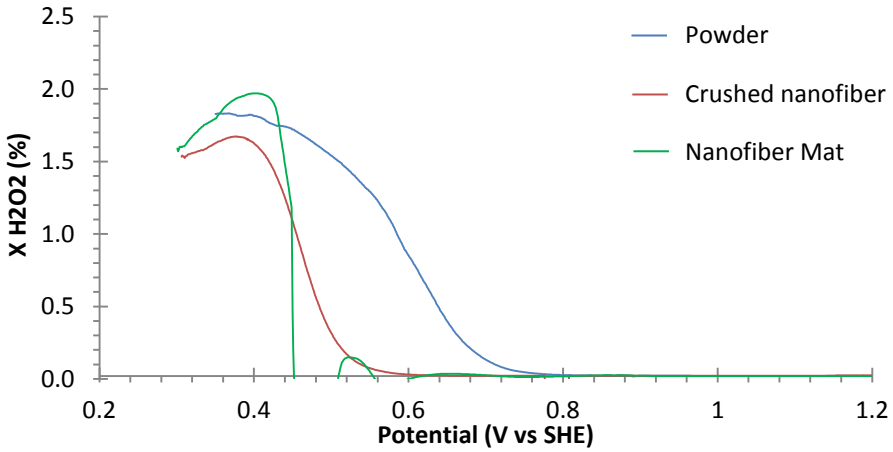


**Figure 78: Percentage formation of hydrogen peroxide of 16 wt% Pt loaded catalysts with different support structures measures in $O_2$ saturated 0.1 M $HClO_4$ solution at 1600 rpm.**

### 5.2.5. ADT for catalyst support structures

ADTs were conducted on the different support structures to determine their electrochemical stability under fuel cell conditions. Support corrosion on both blank support materials and support materials with Pt deposited via TICD was conducted. Pt dissolution was conducted on the Pt loaded catalysts of each support structure.

#### *5.2.5.1. Catalyst support corrosion*

The electrochemical stability of the various support structures were determined through cyclic voltammetry conducted in 0.1 M perchloric acid. Each support was subjected to 10 000 potential cycles between 1.0-1.5 V vs SHE as an accelerated support durability protocol. The results are shown below.

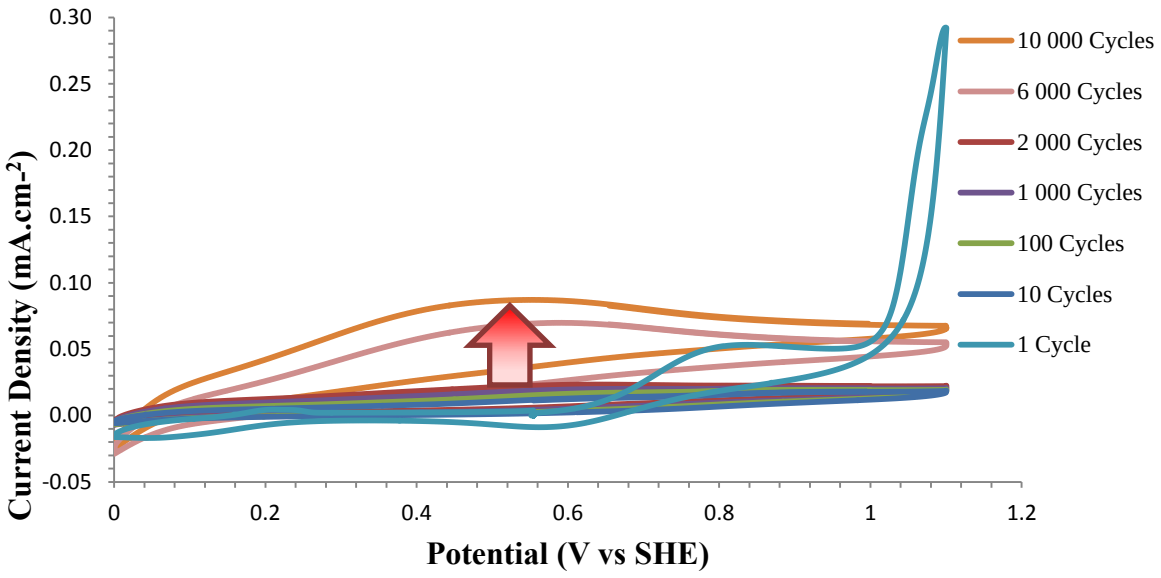


**Figure 79: Cyclic Voltammetry of blank $TiB_2$ powder supports after 1 – 10000 cycles of the support corrosion ADT tests.**

As seen in Figure 79 $TiB_2$ powder displays a steep peak in the oxidation region between ca. 0.8- 1.2 V vs SHE in the first cycle. This points to the oxidation of species on the surface of $TiB_2$. We were unable to determine the exact nature of the species, however we suspect them to be borates such as $TiBO_3$ and $B_2O_3$ . This peak reduces significantly from cycle to

cycle and completely disappears by the 5$^{th}$ cycle. There is also a visible increase in the double layer redox region after oxidation treatment. The peaks are formed as a result of the surface oxides formed on the $TiB_2$ surface. This is not in agreement with the results presented in Yin et al. (2010) where no surface oxides were reported on the $TiB_2$ surface after oxidation treatment. The concentration of Ti and B ions in the electrolyte solution was determined through ICP-AES and the results are shown in Table 21. The rate of oxidation from the 10 to the 10 000 cycle is 7.6 nA.cm$^{-2}$/cycle.

**Table 22: ICP-AES results of the support ion concentration of $TiB_2$ powder support in the electrolyte leached during support corrosion ADTs.**

| | **Concentration in electrolyte (ppb)** |
|---|---|
| Ti | 667 |
| B | 863 |

The leaching of Ti and B ions into solution indicated the instability of powder supports under oxidation treatment.

Nanofiber support materials were placed under the same conditions and the resulting cyclic voltammograms can be seen in Figure 80.

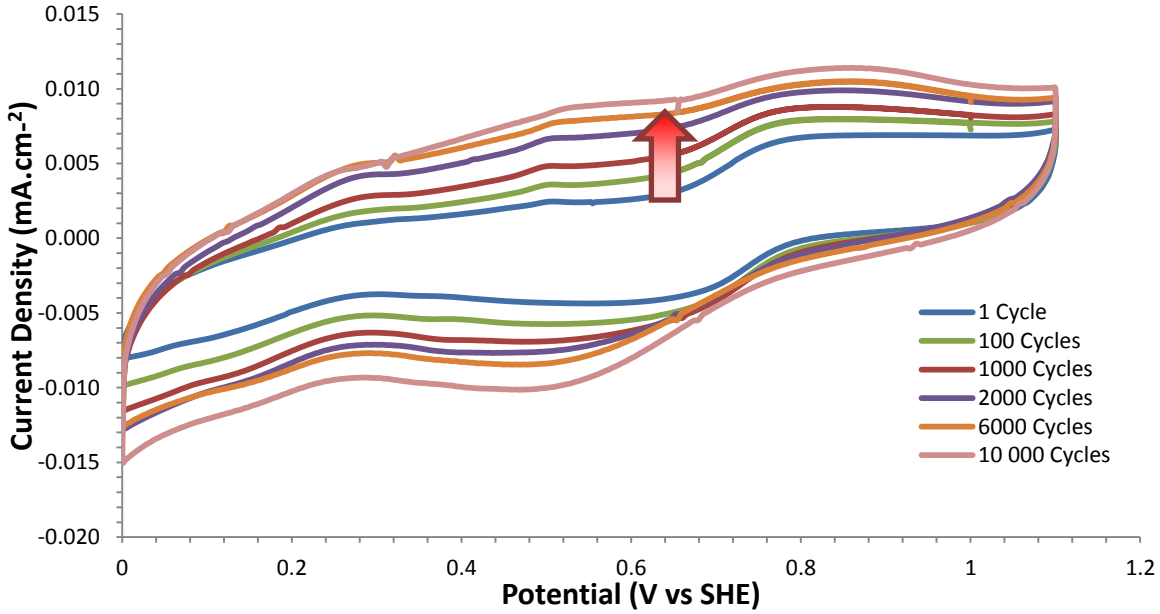


**Figure 80: Cyclic voltammetry of blank TiB2 NF supports after 1 – 10000 cycles of the support corrosion ADT tests.**

Figure 80 of the blank NF support material indicates a higher stability than in the case of Powder material. Cycle 1 does not have a peak in the oxidation region above 0.8 V vs SHE which can be attributed to the fact that the material goes through a range of steps in preparing the nanofiber mats. There is an overall increase in the redox region as seen in the case of powder material due to the formation of surface oxides after oxidation treatment. The oxidation current, however, is smaller than for powder materials after 10 000 cycles. The rate of oxidation is 0.64 $nA.cm^{-2/}$cycle which is 10 times less than the rate of oxidation for the powder material proving its higher resistance to electrochemical oxidation. The Ti and B ions leached into the electrolyte presented in Table 22 is significantly less than that leached by the powder support validating its higher stability. The detection limits for the ICP-AES was 1 ppb.

**Table 23: ICP-AES results of the support ion concentration of $TiB_2$ NF support in the electrolyte leached during support corrosion ADTs.**

| | **Concentration in electrolyte (ppb)** |
|---|---|
| Ti | 113.7 |
| B | Below Detection limits |

Support corrosion ADTs were conducted on catalysts prepared by TICD to observe the influence Pt has on the electrochemical oxidation for each support material. This investigation was conducted on the 16 wt% Pt loaded catalysts and compared against one another.

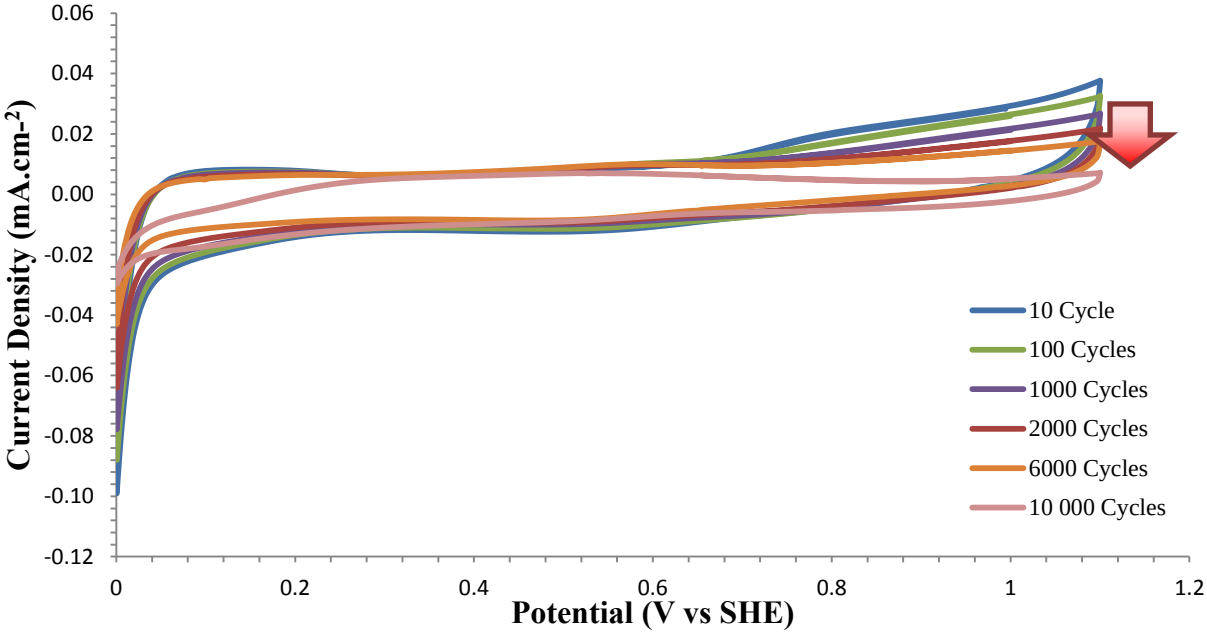


**Figure 81: Cyclic Voltammetry of 16 wt% Pt loaded $TiB_2$ powder catalysts after 1 – 10000 cycles of the support corrosion ADT tests.**

Figure 81 indicates a decrease in the current in the regions above 1.0 V vs SHE indicating the production of hydroxides. The ECSA reduces significantly from cycle 10 – 10 000 indicating the poor electrochemical stability of this material. The concentration of the ions in the electrolyte after ADT was determined and are presented in Table 23

**Table 24: Powder support material leached into electrolyte during support corrosion ADT analysed by ICP-AES**

| | **Concentration in electrolyte (ppb)** |
|---|---|
| Ti | 232.32 |
| B | Below Detection limits |
| **Pt** | 3.6 |

Crushed nanofiber was now tested under the same conditions and Pt loading and the cyclic voltammograms can be seen in Figure 82.

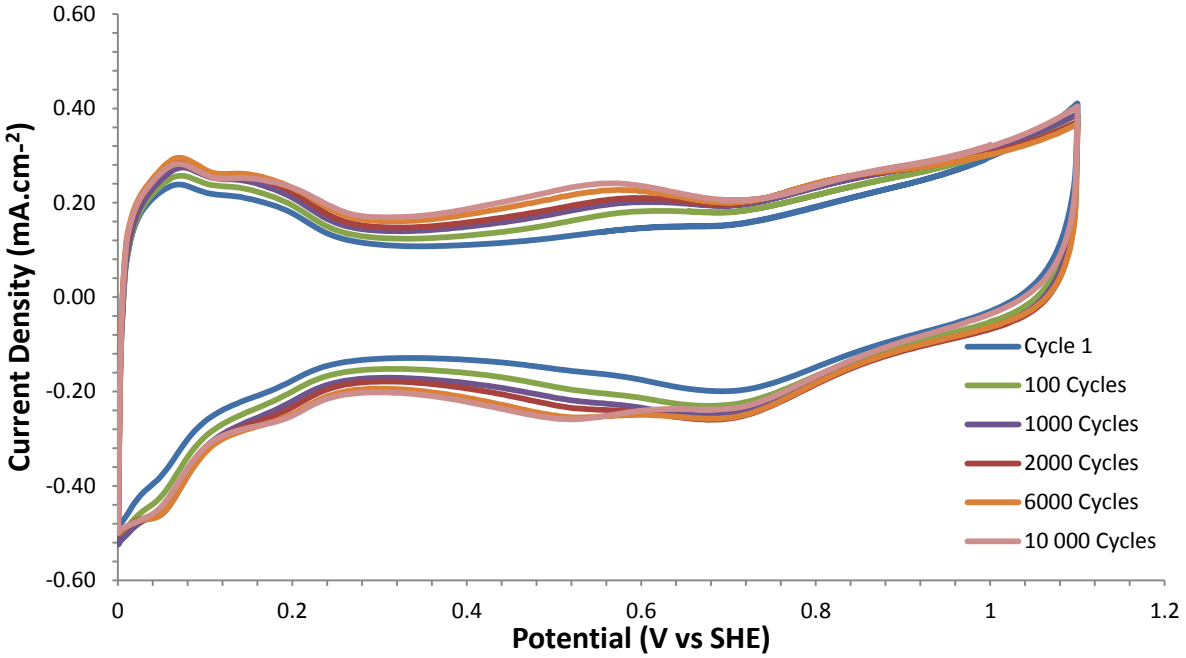


**Figure 82: Cyclic voltammetry of 16wt% Pt loaded CNF powder catalysts after 1 – 10000 cycles of the support corrosion ADT tests.**

Crushed nanofiber proves to display a more stable behaviour than powder with the oxidation peaks remaining constant over time. There is, however, an increase in the redox region of the voltammogram indicating the production of surface oxides. The ECSA increases with the number of cycles indicating the some form of surface activation as well as a strong bond between the support material and Pt metal as agglomeration seems to be very limited. ICP-AES results prove the stability of this support structure by no Pt and B ions in electrolyte after 10 000 cycles. The Ti was leached but this was less than leached in powder support.

**Table 25: CNF support material leached into electrolyte during support corrosion ADT analysed by ICP-AES**

| | Concentration in electrolyte (ppb) |
|---|---|
| Ti | 189.26 |
| B | Below detection limits |
| Pt | Below detection limits |

Support corrosion ADTs were conducted on 16wt % Pt /nanofiber mat catalysts. The resulting cyclic voltammograms can be seen in Figure 83.

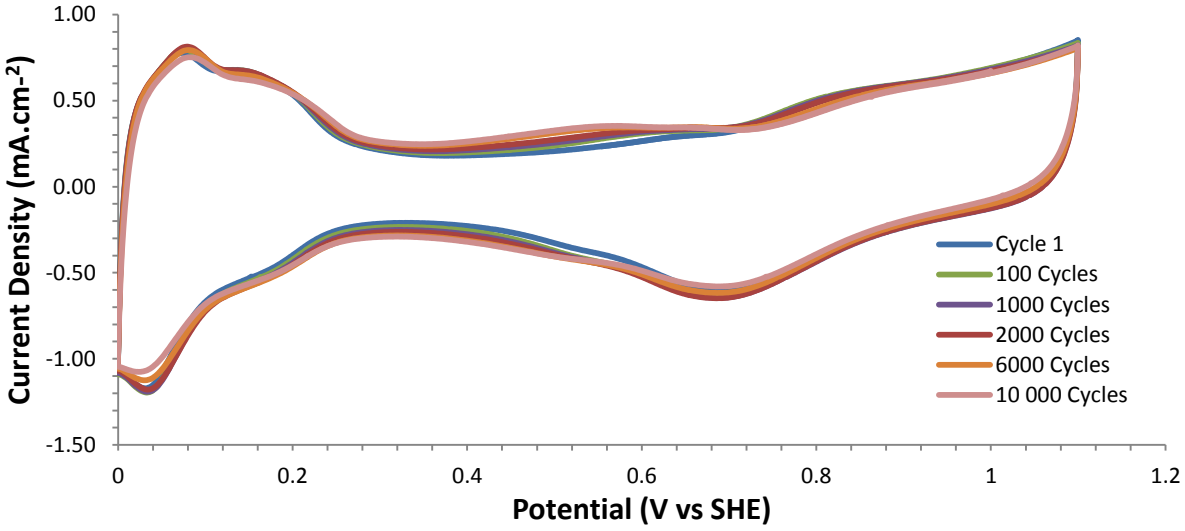


**Figure 83: Cyclic voltammetry of 16 wt% Pt loaded $TiB_2$ NF catalysts after 1 – 10000 cycles of the support corrosion ADT tests.**

Support corrosion studies on 16 wt% Pt loaded NF mat proved the superior stability of this support structure. When compared to crushed fiber, it can be said that the continuous strands of nanofiber positively influences the stability of the support and the Pt anchorage on this support is more superior to a particle or crushed fiber. This is in line with what was found above and is very likely related to less exposure of highly reactive edges and corners in the fibre case. There is a slight increase in the double layer redox region however not as significant as in the case of crushed fiber. The ECSA remains almost constant with an

increase in the number of cycles. The concentration of ions in solution proved to be too low to be detected by ICP-OES therefore no results were supplied.

The summary of all the ECSA loss for support corrosion tests can be seen in Figure 84 below.

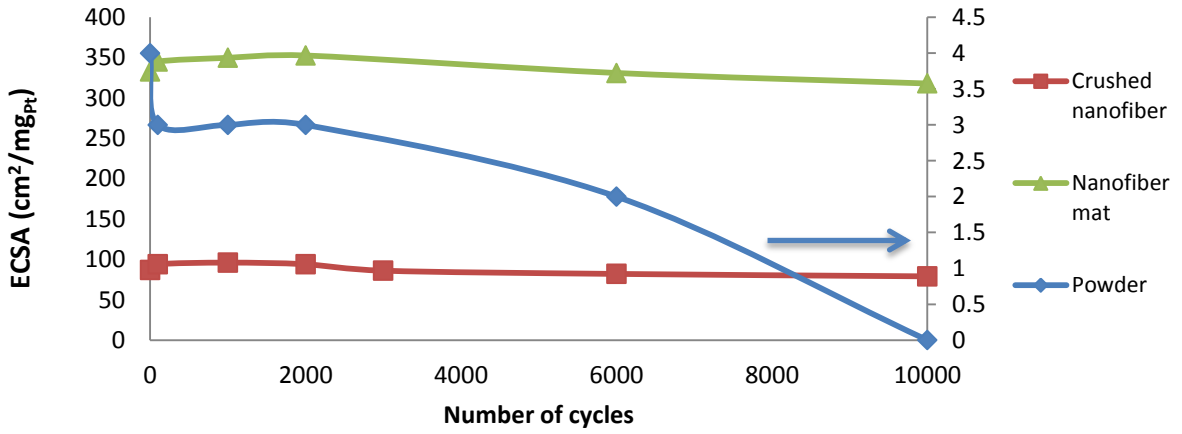


**Figure 84: Summary of loss in ECSA for each support structure with a Pt loading of 16 wt% after 0 – 10 000 cycles of support corrosion ADTs.**

Figure 84 shows that both nanofiber based support retain their ECSA over 10 000 cycles. The percentage loss of ECSA for the NF mat is 9.1%, crushed nanofiber is 17.7% and powder almost 100%. The issue with powder was the low conductivity displayed by the material therefore, the Pt $H_{upd}$ peaks were very low and dwarfed by the redox region after 10 000 cycles making it almost impossible to determine the ECSA. It was decided to not add carbon in this durability study so as to minimise the influence carbon would have on the stability studies of the support materials.

#### *5.2.5.2. Pt dissolution*

The support materials were subjected to Pt dissolution ADT and the corresponding cyclic voltammograms after 10 000 rectangular wave cycling was recorded.

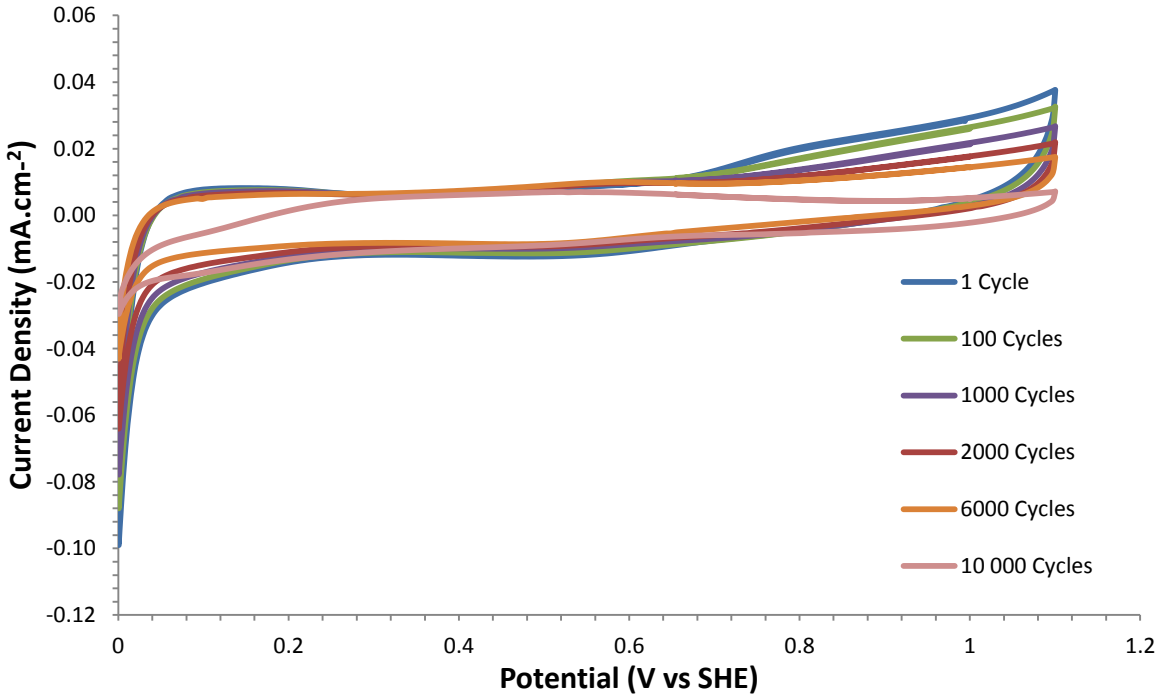


**Figure 85: Cyclic voltammetry of 16wt% Pt loaded $TiB_2$ powder catalysts after 1 – 10000 cycles of the Pt dissolution ADT tests.**

Figure 85 shows a reduction in the oxidation peaks after potentials of 1.0 V vs SHE. This indicates the production of hydroxides on the Pt surface. After 10 000 cycles there is an increase in the oxidation peak. This is linked to the reduction in $H_{upd}$ below 0.3 V vs SHE. The loss in the ECSA after ADT can be found in Figure 88.Table 25 shows the concentration of leached ions in electrolyte after Pt dissolution ADTs.

**Table 26: Powder supported catalyst material leached into electrolyte during Pt dissolution ADT analysed by ICP-AES**

| | Concentration in electrolyte (ppb) |
|---|---|
| Ti | 627 |
| B | 483 |
| Pt | 47.7 |

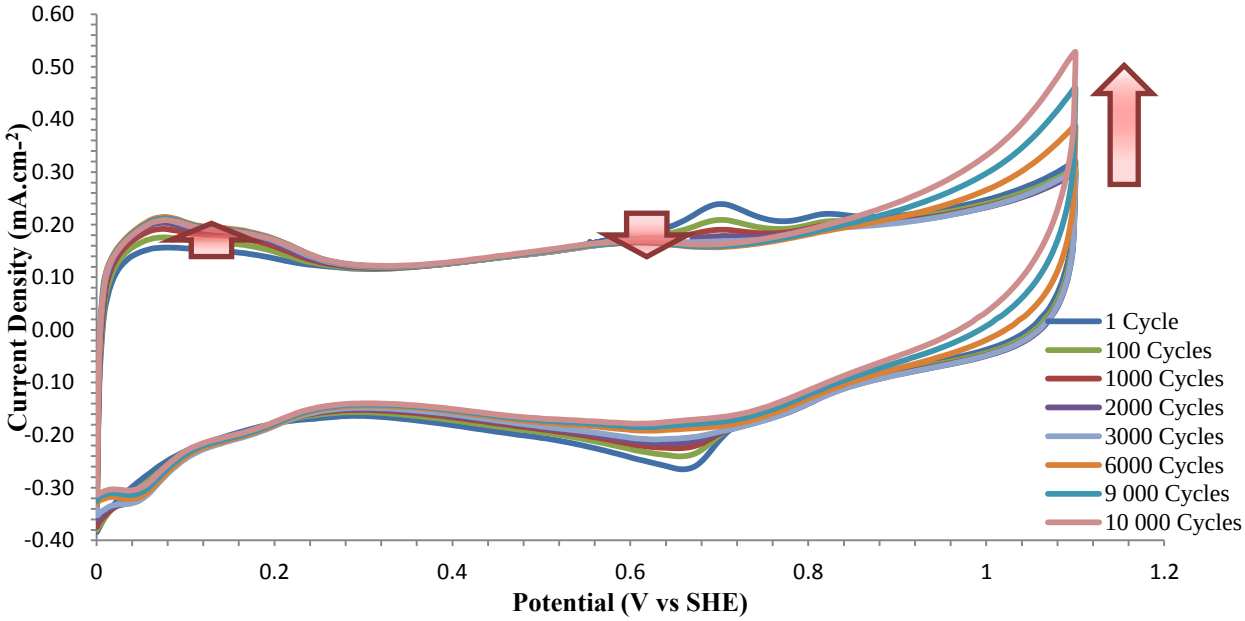


**Figure 86: Cyclic Voltammetry of 16wt% Pt loaded $TiB_2$ CNF catalysts after 1 – 10000 cycles of the Pt dissolution ADT tests.**

The overall ECSA increases for the crushed nanofiber support over the number of cycles. This indicates surface activation and a strong anchoring of the Pt to the nanofiber surface. There is an increase in the oxidation currents over the number of cycles with a subsequent drop in the double layer redox region. This points towards fewer surface oxides present after oxidation treatment. The trend for the increase in ECSA can be found in Figure 88. Table 26 shows the concentration of leached ions in electrolyte after Pt dissolution ADTs

**Table 27: CNF supported catalyst material leached into electrolyte during Pt dissolution ADT analysed by ICP-AES**

| | Concentration in electrolyte (ppb) |
|---|---|
| Ti | 334 |
| B | 246 |
| Pt | 20.8 |

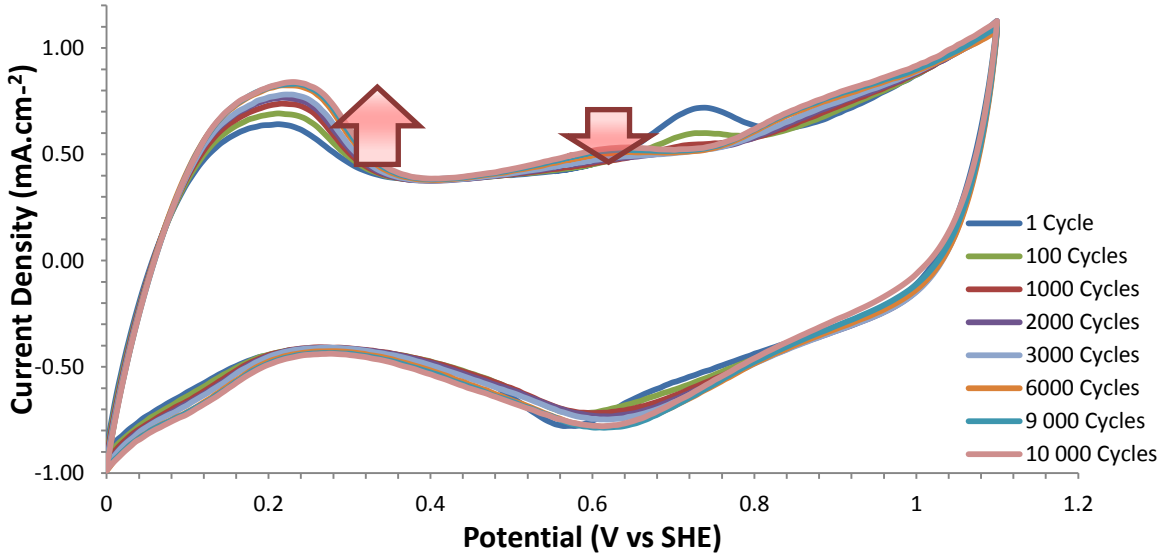


**Figure 87: Cyclic voltammetry of 16wt% Pt loaded $TiB_2$ NF catalysts after 1 – 10000 cycles of the Pt dissolution ADT tests**

Nanofiber mats show the highest electrochemical stability after 10 000 cycles with a reduction in the surface oxides over time. The oxidation currents remain constant while there is an overall increase in ECSA. Table 27 shows the concentration of leached ions in electrolyte after Pt dissolution ADTs

**Table 28: NF supported catalyst material leached into electrolyte during Pt dissolution ADT analysed by ICP-AES**

| | Concentration in electrolyte (ppb) |
|---|---|
| Ti | 263 |
| B | 39.9 |
| Pt | Below Detection Limits |

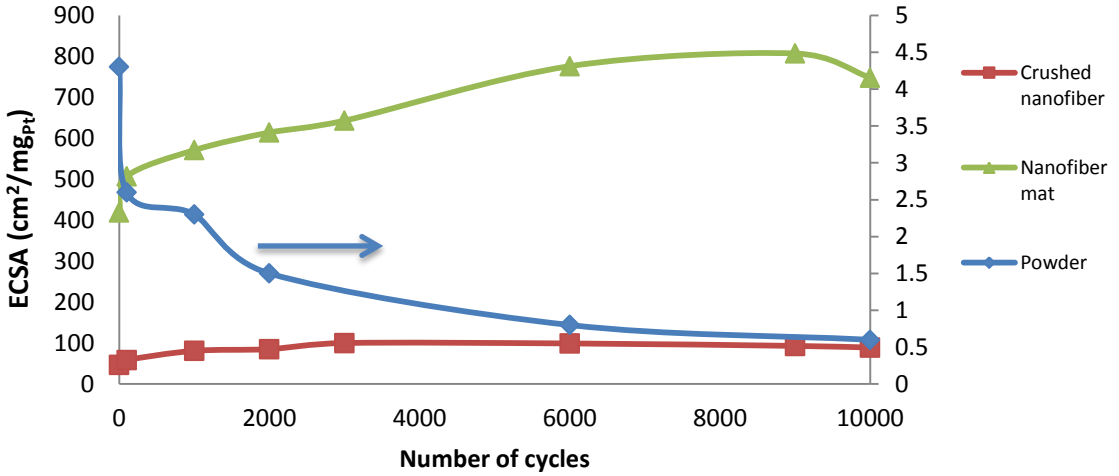


**Figure 88: Summary of the ECSA trends for each support structure with a Pt loading of 16wt% after 0 – 10 000 cycles of Pt dissolution ADTs.**

Figure 88 indicates that nanofibers have a strong Pt anchoring as the ECSA increase over Pt dissolution ADTs. Powder supports cause an overall decrease in ECSA over 10 000 cycles. This proves that the nano-structuring of the support materials are favourable for long-term electrochemical stability of the catalysts.

# 6. CONCLUSION

This study has been directed towards the development of an alternative catalyst support material and structure to commonly used carbon powder. The poor durability of carbon powder has been identified as one of the key issues in PEFCs. It is for this reason that the focus of this study has been to steer away from this material and conduct an in-depth analysis of a new material and structure. In particular, a systematic investigation on the influence of the nanostructure of $TiB_2$ supports on the overall electrocatalyst performance has been undertaken. $TiB_2$ Powder, crushed nanofiber and nanofiber mats were evaluated and compared as alternative PEFC support materials. This is the first study considering $TiB_2$ nanofiber mats as support materials for PEFC and therefore aims to contribute the development of a new generation of fuel cell catalysts.

Physical characterisation of the three support structures prepared using both magnetron sputtering and TICD validated these techniques as reliable methods for platinum deposition. However, in the case of the model electrode prepared by magnetron sputtering, the Pt loadings of 100 and 200 $\mu g/cm^2$ proved to be too high forming a platinum film on the surface of the support. Therefore no clear correlation or differentiation between the ECSA trends and loadings can be made.

TICD prepared catalysts displayed a more realistic system to identify the influence of the support structure and morphology on the Pt deposition. TEM and SEM analysis indicated Pt loadings of close to 8 wt% and 16 wt% have been achieved validating the reproducibility of this method of Pt deposition for $TiB_2$ powder, crushed nanofiber and nanofiber mat catalysts. A large degree of Pt agglomeration was found on the $TiB_2$ powder however, Pt homogenously distributed over the nanofiber based support materials with little to no agglomeration indicating the uniform binding sites available on nanofibers for Pt.

Surface functionalization via $HNO_3$ and $H_2SO_4$ acid treatment and temperature programmed reduction was conducted on the $TiB_2$ powder and was found to not resolve the Pt agglomeration found at lower and higher Pt loadings. It can be concluded that further

investigation into broader, more controlled surface treatments could be done to improve Pt anchorage and distribution on $TiB_2$ powder.

Electrochemical characterisation was conducted on the catalysts prepared and it can be concluded that the support properties play an important role to the electrochemical performance of the electrocatalysts. An interesting finding was the failure in general $H_{upd}$ and CO stripping techniques to accurately and reliably evaluate the ECSA for the $Pt/TiB_2$ catalysts. These techniques lacked a correct baseline for integration of the associated charges. This result was confirmed in previous studies performed by Binninger et al. (2014) to be the contribution of the support material on the overall CV currents and therefore the calculated ECSA of the catalyst. An alternative route for ECSA calculation was established and applied in this study. A baseline correction method was applied using a CV recorded in a CO saturated electrolyte at 1600 rpm as the baseline for the general $H_{upd}$ technique. This method proved to be a more accurate and reproducible $H_{upd}$ analysis for ECSA determination of these $TiB_2$ supported catalysts. $Pt/TiB_2$ powder electrocatalysts had very low ECSA values.

Linear sweep voltammetry results for the support materials suggested that the low ECSA and high ohmic losses obtained for the $TiB_2$ powder materials indicates a major conductivity issue. This issue was addressed by adding highly conductive acetylene black to the catalyst ink following the research conducted by Shim et al. (2001) and Xiong & Manthiram (2004). This addition drastically improved the ECSA and ORR kinetic current of $TiB_2$. The improvement was also seen in the case of the nanofiber supports as the addition of carbon slightly improved the roughness of the nanofiber supports therefore reducing the high limiting currents. RRDE studies reveal that the $TiB_2$ electrocatalysts prepared produced minimal $H_2O_2$ confirming the $4e^-$ pathway for ORR.

Accelerated durability tests on the powder, crushed nanofiber and nanofiber mats proved that nanofiber mats display superior durability to the other support structures. Powder subjected to 10 000 cycles of support corrosion cycles resulted in a significantly larger concentration of Ti, B and Pt ions leached into the electrolyte solution. There is a large

increase in the double layer region for the powder supports as a result of the surface oxides formed. The rate of oxidation for the powder was 10 times greater than for the nanofiber support. Superior durability of the crushed nanofiber and nanofiber mat was also indicated by Pt dissolution ADT results. Nanofiber materials only displayed a reduction in ECSA after 8000 cycles. Powder supports show a near 100% reduction in ECSA over 10000 cycles. This proves that the nano-structuring of the support materials is favourable for long-term electrochemical stability of the catalysts.

In conclusion, the most interesting finding was the vast improvement in ECSA and activity measurements when replacing the catalyst support materials from nanoparticles (powder) to nanofibers. Although the support materials were the same ($TiB_2$), they differed in their structure and morphology. The crushed nanofiber and nanofiber mat proved to be a superior support for Pt catalysts. The outstanding performance of this structure can be explained by the unique fiber morphology, inter fiber and intra fiber pores leading to greater electrochemical surface area of accessible platinum, higher mass activity and better catalyst utilisation than for powder. The combination of the improved kinetics and exceptional durability of nanofiber mats proves that this material is the superior support structure when compared to powder and crushed nanofiber. This novel support material thus displays promising influences on the electrochemical performance of $TiB_2$ electrocatalysts. This study has thus shown that nanostructured supports and in particular nanostructured inorganic support materials have great potential for future fuel cell applications.

Since this study was the first of its kind, a lot of new questions and potential research avenues need to be looked into going forward. Firstly the $TiB_2$ mats investigated in this study were very brittle and therefore difficult to handle. In developing this technology further towards an actual product, they would need to be more rigid. Further $TiB_2$, even as nanofiber does not display satisfactory conductivity yet, more research is needed into more conductive materials for the nanofibers or ways to improve the $TiB_2$ nanofibers. Another avenue to be explored could be to reduce the loading of the DC sputtered electrodes to

better understand the influence of support materials on these electrodes. A greater understanding of the oxidation behaviour of the materials needs to be gained, influences of temperature and operating time since this material is a new support material to be applied in PEFC technology.

# 7. APPENDIX

**Table 7-1: Pt loading calculations for catalysts prepared via TICD on $TiB_2$ powder supports.**

| Sample | | Mass of Titanium (mg) | Mass of Pt (mg) | Total mass (mg) | Loading (%) | | |
|---|---|---|---|---|---|---|---|
| Powder 16 wt% | 1 | 80.01 | 19.99 | 136.14 | 14.68 | | |
| | 2 | 26.53 | 5.34 | 43.85 | 12.18 | Mean | St. Dev |
| | 3 | 26.39 | 7.24 | 45.55 | 15.89 | 14.25 | 1.93 |
| Powder 8 wt% | 1 | 86.71 | 13.29 | 139.16 | 9.55 | | |
| | 2 | 72.6 | 9.8 | 115.2 | 8.5 | Mean | St. Dev |
| | 3 | 87.06 | 12.94 | 139.32 | 9.29 | 9.11 | 0.52 |

**Table 7-2: Pt loading calculations for catalysts prepared via TICD on TiB2 CNF supports**

| Sample | | Mass of Titanium (mg) | Mass of Pt (mg) | Total mass (mg) | Loading (%) | | |
|---|---|---|---|---|---|---|---|
| CNF 16 wt% | 1 | 63.96 | 29.04 | 128.89 | 20.96 | | |
| | 2 | 69.24 | 30.76 | 131.27 | 23.43 | Mean | St. Dev |
| | 3 | 70.26 | 29.74 | 131.73 | 22.58 | 21.66 | 1.89 |
| CNF 8 wt% | 1 | 74.2 | 5.03 | 112.74 | 4.46 | | |
| | 2 | 71.41 | 8.03 | 111.69 | 7.19 | Mean | St. Dev |
| | 3 | 67.52 | 7.55 | 105.57 | 7.15 | 6.27 | 1.56 |

**Table 7-3: Pt loading calculations for catalysts prepared via TICD on TiB2 NF supports**

| Sample | | Mass of Titanium (mg) | Mass of Pt (mg) | Total mass (mg) | Loading (%) | | |
|---|---|---|---|---|---|---|---|
| CNF 16 wt% | 1 | 52.25 | 16.19 | 92.04 | 17.59 | | |
| | 2 | 62.77 | 13.93 | 105.05 | 13.26 | Mean | St. Dev |
| | 3 | 60.02 | 19.68 | 106.81 | 18.43 | 16.43 | 2.77 |

| | | | | | | | |
|---|---|---|---|---|---|---|---|
| **CNF 8 wt%** | 1 | 54.83 | 5.68 | 85.27 | 6.66 | | |
| | 2 | 50.66 | 8.74 | 82.28 | 10.62 | **Mean** | **St. Dev** |
| | 3 | 56.66 | 5.37 | 87.62 | 6.13 | 7.80 | 2.46 |

# 8. REFERENCES

Aksoylu, A. E; Faria, J L; Pereira, M F.R; Figueiredo, J L; Serp, P; Hierso, J C; Feurer, R; Kihn, Y; Kalck, P, 2003. Highly dispersed activated carbon supported platinum catalysts prepared by OMCVD: a comparison with wet impregnated catalysts. Applied Catalysis A: General, Volume 243, p. 357–365.

Alvisi, M; Galtieri, G; Giorgi, L; Serra, E; Signore, M A., 2005. Sputter deposition of Pt nanoclustersand thin films on PEM fuel cell electrodes. Surface & Coatings Technology, Volume 200, pp. 1325-1329.

Antolini, E., 2009. Carbon supports for low-temperature fuel cell catalysts. Applied Catalysis B: Environmental , pp. 1-24.

Avasarala, B. & Haldar, P., 2011. On the stability of TiN-based electrocatalysts for fuel cell. International Journal of Hydrogen Energy, Volume 36, pp. 3965-3974.

Babir, F. & Yazici, S., 2008. Status and development of PEM fuel cell technology. International Journal of Energy Research, 32(5), pp. 369-378.

Baker, R. & Zhang, J., 2011. Proton Exchange Membrane or Polymer Electrolyte Membrane (PEM) Fuel Cells.[Online] Available at: http://knowledge.electrochem.org/encycl/art-f04-fuel-cells-pem.htm [Accessed July 2015].

Barbir, F., 2013. Fuel Cell Diagnostics. In: PEM Fuel Cells: Theory and Practice. 2 ed. s.l.:Academic Press, pp. 265-305.

Basu, B., Raju, G. B. & Suri, A. K., 2006. Processing and properties of monolithic TiB2 based materials. International Materials Reviews, 51(6), pp. 352-374.

Binninger, T., Fabbri, E., Kotz, R. & Schmidt, T. J., 2014. Determination of the electrochemically active surface area of metal-oxide supported platinum catalyst. Journal of The Electrochemical Society, 161(3), pp. H121-H128.

Bladergroen, B., Su, H., Pasupathi, S. & Linkov, V., 2012. Overview of Membrane Electrode Assembly Preparation Methods for Solid Polymer Electrolyte Electrolyzer. In: D. J. Klaperis, ed. Electrolysis. s.l.:InTech, pp. 45-60.

Bock, C., Halvorsen, H. & MacDougall, B., 2008. Catalyst Synthesis Techniques. In: J. Zhang, ed. PEM Fuel cell electrocatalysts and catalyst layers: fundamentals and applications. Canada: Springer, pp. 447-487.

Bock, C., Halvorsen, H. & MacDougall, B., 2008. Catalyst Synthesis Techniques. In: J. Zhang, ed. PEM Fuel Cell Electrocatalysts and Catalyst Layers Fundamentals and Applications. s.l.:Springer, pp. 447-479.

Brodt, M., Wycisk, R. & Pintauro, P. N., 2013. Nanofiber Electrodes with Low Platinum Loading for High Power Hydrogen/Air PEM Ful Cells. Journal of the Electrochemical Society, 160(8), pp. 744-749.

Cabot Corporation, 2015. VULCAN® XC72 Conductive Carbon Black datasheet. [Online] Available at: http://www.cabotcorp.com/solutions/products-plus/specialty-carbon-blacks/conductive
[Accessed 30 July 2015].

Chevallier, Laure; Bauer, Alexander; Cavaliere, Sara; Hui, Rob; Roziere, Jacques; Jones, Deborah J., 2012. Mesoporous Nanostructured Nb-Doped Titanium Dioxide Microsphere Catalyst Supports for PEM Fuel Cell Electrodes. ACS Appl. Mater. Interfaces, 4(3), pp. 1752-1759.

Chhina, H., Campbell, S. & Kesler, O., 2009. Ex Situ and In Situ Stability of Platinum Supported on Niobium-Doped Titania for PEMFCs. Journal of Electrochemical Society, 156(10), pp. B1232-B1237.

Chiang, Y.C., Lin, . W.H. & Chang, Y.C., 2011. The influence of treatment duration on multi-walled carbon nanotubes functionalized by H2SO4/HNO3 oxidation. Applied Surface Science, Volume 257, pp. 2401-2410.

Colon-Mercado, H. R., Kim, H. & Popov, B. N., 2004. Durability study of Pt3Ni1 catalysts as cathode in PEM fuel cells. Electrochemistry Communications, Volume 6, pp. 795-799.

Cooper, K. R., 2014. In Situ PEM FC Electrochemical Srface Area and Catalyst Utilization Measurment, s.l.: Scribner Associates.

Corporation, Cabot, 2015. VULCAN® XC72 Conductive Carbon Black datasheet. [Online] Available at: http://www.cabotcorp.com/solutions/products-plus/specialty-carbon-blacks/conductive
[Accessed 30 July 2015].

Debe, M. K., Schmoeckel, A. K., Vernstrom, G. D. & Atanasoski, R., 2006. High voltage stability of nanostructured thin film catalysts for PEM fuel cells. Journal of Power Sources, Volume 161, pp. 1002-1011.

Di Paola, A., Bellardita, M. & Palmisano, L., 2013. Brookite, the Least Known TiO2 Photocatalyst. Catalysts 2013, 3(1), pp. 36-73.

Dicks, A., 2006. The role of carbon in fuel cells. Journal of Power Sources, pp. 128-141.

Dong, Z., Kennedy, S. J. & Wu, Y., 2011. Electrospinning materials for energy-related applications and devices. Journal of Power Sources, Volume 196, pp. 4886-4904.

Dowler, H. R. M., 2013. Preparation of catalysts on model supports using wet chemical methods and the construction of a device for the in-situ measurement of sum frequency generation spectroscopy at the solid-liquid interface, Berlin: Technischen Universiteit Berlin.

Fabbri, Emiliana; Taylor, Susan; Rabis, Annett; Levecque, Pieter; Conrad, Olaf; Kotz, Rudiger; Schmidt, Thomas J., 2014. The Effect of Platinum Nanoparticle Distribution on Oxygen Electroreduction Activity and Selectivity. ChemCatChem, 6(5), pp. 1410-1418.

Falch, A., Lates, V. & Kriek, R. J., 2015. Combinatorial plasma sputtering of PtxPdy thin film electrocatalysts for aqueous SO2 electro-oxidation, Potchefstroom: s.n.

Fang, J., Wang, X. & Lin, T., 2011. Functional Applications of Electrospun Nanofibers. In: T. Lin, ed. Nanofibers - Production, Properties and Functional Applications. China: InTech, pp. 287-326.

Franco, Alejandro A; Gerard, Mathias; Guinard, Magalie; Barthe, Benoit; Lemaire, Olivier., 2008. Carbon Catlayst-Support Corrosion in Polymer Electrolyte Fuel Cells: Mechanistic Insights. The Electrochemical Society Transactions, pp. 35-55.

Garsany, Y., Baturina, O. A., Swider-Lyons, K. E. & Kocha, S. S., 2010. Experimental Methods for Quantifying the Activity of Platinum Electrocatalysts for the Oxygen Reduction Reaction. Analytical Chemistry, 82(15), pp. 6321-6328.

Gasteiger, H. A., Kocha, S. S., Sompalli, B. & Wagner, F. T., 2005. Activity benchmarks and requirements for Pt, Pt-alloy, and non-Pt oxygen reduction catalysts for PEMFCs. Applied Catalysis B: Environmental, Volume 56, pp. 9-35.

Gates, B. C., 2008. Synthesis of oxide- and zeolite- supported catalysts form organometallic precursors. In: J. Regalbuto, ed. Catalyst Preparation: Science and Engineering. s.l.:CRC Press Taylor & Fancis Group, pp. 237-248.

Greim, J. & Schwetz, K. A., 2006. Boron Carbide, Boron Nitride, and Metal Borides. Ullmann's Encyclopedia of Industrial Chemistry, Volume 6, pp. 219-236.

Heeyeon, K. & Sang Heup, M., 2011. Chemical vapor deposition of highly dispersed Pt nanoparticles on multi-walled carbon nanotubes for use as fuel-cell electrodes. Carbon, 49(4), pp. 1491-1501.

Hierso, J.-C., Serp, P., Feu, R. & Kalck, P., 1998. MOCVD of rhodium, palladium and platinum complexes on fluidized divided substrates:Novel process for one-step preparation of noble-metal catalysts. Applied Organometalic Chemistry, Volume 12, p. 161–172.

Hishinuma, T., Chikahisa, T., Kagami, F. & Ogawa, T., 2004. The design and performance of a PEFC at a temperature below freezing. JSME International Journal Series B, 47(2), pp. 235-241.

Huang, S.-Y., Ganesan, P. & Popov, B. N., 2010. Electrocatalytic activity and stability of niobium-doped titanium oxide supported platinum catalyst for polymer electrolyte membrane fuel cells. Applied Catalysis B: Environmental, 96(1-2), p. 224–231.

Huang, S.-Y., Ganesan, P. & Popov, B. N., 2011. Titania supported platinum catalyst with high electrocatalytic activity and stability for polymer electrolyte membrane fuel cell. Applied Catalysis B: Environmental, 102(1-2), pp. 71-77.

Hughes, M., 2015. The Global Source: SemiCore. [Online] Available at: http://www.semicore.com/what-is-sputtering [Accessed 21 March 2015].

Jiang , H., Zhu , L., Moon , . K.-s. & Wong, C. P., 2007. The preparation of stable metal nanoparticles on carbon nanotubes whose surfaces were modified during production. Carbon, Volume 45, pp. 655-661.

Jiang, Z. & Jiang, Z.-J., 2011. Carbon Nanotubes Supported Metal Nanoparticles for the Applications in Proton Exchange Membrane Fuel Cells (PEMFCs). In: D. M. Naraghi, ed. Carbon Nanotubes: Growth and Application. 1 ed. s.l.:InTech, pp. 567-604.

Kim , Y. S., Jang , H. S. & Kim, W. B., 2010. An efficient composite hybrid catalyst fashioned from Pt nanoparticles and Sb-doped SnO2 nanowires for alcohol electro-oxidation. Journal of Materials Chemistry, 20(36), pp. 7859-7836.

Kim, Hyung Ju; Kim, Yong Seok; Seo, Min Ho; Choi, Sung Mook; Kim, Won Bae, 2009. Pt and PtRh nanowire electrocatalysts for cyclohexane-fueled polymer electrolyte membrane fuel cell. Electrochemistry Communications, Volume 11, pp. 446-449.

Knights, S. D., Colbow, K. M., St-Pierre, J. & Wilkinson, D. P., 2004. Aging mechanisms and lifetime of PEFC and DMFC. Journal of Power Sources, Volume 127, pp. 127-134.

Lee, K.-S.et al., 2008. Electrocatalytic activity and stability of Pt supported on Sb-doped SnO2 nanoparticles for direct alcohol fuel cells. Journal of Catalysis, 258(1), pp. 143-152.

Li, M., Han, G. & Yang, B., 2008. Fabrication of the catalytic electrodes for methanol oxidation on electrospinning-derived carbon fibrous mats. Electrochemistry Communications, Volume 10, pp. 880-883.

Litster, S. & McLean, G., 2004. PEM fuel cell electrodes. Journal of Power Sources, Volume 130, pp. 61-76.

Li, Wenzhen ; Liang, Changhai ; Qiu, Jieshan; Zhou, Weijiang ; Han, Hongmei; Wei, Zhaobin; Sun, Gongquan; Xin, Qin., 2002. Carbon nanotubes as support for cathode catalyst of a direct methanol fuel cell. Carbon, Volume 40, pp. 787-803.

Long, Qi; Cai, Mei; Li, Jinru; Rong, Huilin; Jiang, Long., 2011. Improving the electrical catalytic activity of Pt/TiO2 nanocomposites by a combination of electrospinning and microwave irradiation.. Journal Of Nanoparticle Research, 13(4), pp. 1655-1662.

Maass, S; Finsterwalder , F; Frank , G; Hartmann, R; Merten, C, 2008. Carbon support oxidation in PEM fuel cell cathodes. Journal of Power Sources, Volume 179, pp. 444-451.

Maillard, F; Schreier, S; Hanzlik, M; Savinova, E R; Weinkauf, S; Stimming, U, 2005. Influence of particle agglomeration on the catalytic activity of carbon-supported Pt nanoparticles in CO monolayer oxidation. Physical Chemistry Chemical Physics, Volume 7, pp. 385-393.

Makharia, R; Kocha, S S; Yu, P T; Sweikart, M A; Gu, W B; Wagner, F T, 2006. Durable PEM fuel cell electrode materials: requirements and benchmarking methodologies. The Electrochemical Society Transactions, 1(8), pp. 3-18.

Martin, T. P., Tripp, C. P. & DeSisto, W. J., 2005. Composite Platinum/Silicon Dioxide Films Deposited using CVD. Chemical Vapor Deposition, 11(3), pp. 170-174.

Masaoa, A; Nodaa, S; Takasakia, F; Itoa, K; Sasaki, K, 2009. Carbon-Free Pt Electrocatalysts Supported on SnO2 for Polymer Electrolyte Fuel Cells. Electrochemical and Solid-State Letters, 12(9), pp. B119-B122.

Maslyn, A., 2011. Carbon Loss in the Cathode Catalyst Support of PEMFC, Univeristy of Rochester: Department of Chemical Engineering.

Matsui, T oshiaki ; Okanishi, Takeoh ; Fujiwa, Katsuhiko; Tsutsui, Kazuki; Kikuchi, Ryuji; Takeguchi, Tatsuya ; Eguchi, Koichi, 2006. Effect of reduction–oxidation treatment on the catalytic activity over tin oxide supported platinum catalysts. Science and Technology of Advanced Materials, 7(6), pp. 524-530.

Mayrhofer, K; Stemcnik, D; Blizanac, B; Stamenkovic, V; Arenz, M; Markovic, N, 2008. Measurement of oxygen reduction activities via the rotating disc electrode method: From Pt model surfaces to carbon-supported high surface area catalysts. Electrochimica Acta, 53(7), p. 3181–3188.

Micro Magnetics, I., 2013. Magnetron Sputtering Technology. [Online] Available at: http://www.directvacuum.com/pdf/what_is_sputtering.pdf [Accessed 21 March 2015].

Mitsushima, S., Kawahara, S., Ota, K.-i. & Kamiya, N., 2007. Consumption Rate of Pt under Potential Cycling. Journal of Electrochemical Society, 154(2), pp. B153-B158.

Molla, S. & Compan, V., 2011. Polyvinyl alcohol nanofiber reinforced Nafion membranes for fuel cell applications. Journal of Membrane Science, Volume 372, pp. 191-200.

Nakada , M iou; Ishihara, Akimitsu ; Mitsushi, Shigenori; Kamiya, Nobuyuki ; Ota, Ken-ichiro, 2007. Effect of Tin Oxides on Oxide Formation and Reduction of Platinum Particles. Electrochemical and Solid-State Letters, 10(1), pp. F1-F4.

Naseh, M. V.; Khodadadi, A A; Mortazavi, Y; Sahraei, O Alizadeh ; Pourfayaz, F; Sedghi, S Mosadegh, 2009. Functionalization of Carbon Nanotubes Using Nitric Acid Oxidation and DBD Plasma. International Scholarly and Scientific Research & Innovation, 3(1), pp. 134-136.

National Research Council Canada, 2010. NRC Institute for Fuel Cell Innovation. [Online] Available at: http://archive.nrc-cnrc.gc.ca/eng/programs/ifci/low-temperature-fuel-cells/membrane-electrode-assembly.html
[Accessed 23 April 2014].

Okanishi, Takeoh; Matsui, Toshiaki ; Takeguch, Tatsuya ; Kikuchi, Ryuji; Eguchi, Koichi, 2006. Chemical interaction between Pt and SnO2 and influence on adsorptive properties of carbon monoxide. Applied Catalysis A: General, Volume 298, pp. 181-187.

Ornelas, R; Stassi, A; Modica, E; Arico, A S; Antonucci, V, 2006. Accelerated degradation tests for Pt/C catalysts in sulfuric acid. ECS Transactions, 3(1), pp. 633-641.

Oyama, S. T., 1996. Introduction to the chemistry of transition metal carbides and nitrides. The Chemistry of Transition Metal Carbides and Nitrides, pp. 1-27.

Parrondo, Javier; Han, Taehee; Niangar, Ellazar; Wang, Chunmei; Dale, Nilesh; Adjemian, Kev; Ramania, Vijay., 2014. Platinum supported on titanium–ruthenium oxide is a remarkably stable electrocatayst for hydrogen fuel cell vehicles. Proceedings of the National Academy of Sciences of the United States of America, 111(1), pp. 45-50.

Paulus , U. A., Schmidt , T. J., Gasteiger , H. A. & Behm, R. J., 2001. Oxygen reduction on a high-surface area Pt:Vulcan carbon catalyst: a thin-film rotating ring-disk electrode study. Journal of Electroanalytical Chemistry, Volume 495, pp. 134-145.

Qui, Z., 2008. Electrochemical methods for catalyst activity evaluation. In: J. Zhang, ed. PEM Fuel Cell Electrocatalysts and catalyst layers: fundametals and applications. Canada: Springer, pp. 547-604.

Rajalakshmi, N., Lakshmi, N. & Dhathathreyan, K. S., 2008. Nano titanium oxide catalyst support for proton exchange. International Journal of Hydrogen Energy, Volume 33, pp. 7521-7526.

Reiser, C. A ; Bregoli, L; Patterson, T W; Yi, J S; Yang, J D, 2005. A reverse-current decay mechanism for fuel cells. Electrochem Solid-State Letters, 8(6), pp. A273-276.

Roen, L. M., Paik, C. H. & Jarvi, T. D., 2004. Electrocatalytic Corrosion of Carbon Support in PEMFC cathodes. Electrochemcical Solid State Letters, 7(1), pp. A19-A22.

Roth, Christina; Bleith, Peter; Schwöbel, Christoph A.; Kaserer, Sebastian ; Eichler, Jens , 2014. Importance of Fuel Cell Tests for Stability Assessment—Suitability of Titanium Diboride as an Alternative Support Material. Energies, Volume 7, pp. 3642-3652.

Savych, I ; Bernard d'Arbigny, J; Subianto, S; Cavaliere, S; Jones, D J; Rozière, J, 2014. On the effect of non-carbon nanostructured supports on the stability of Pt nanoparticles during voltage cycling: A study of TiO2 nanofibres. Journal of Power Sources, Volume 257, pp. 147-155.

Schmidt, T. J.; Gasteiger, H A; Stab, G D; Urban, P M; Kolb, D M; Behm, R J., 1998. Characterization of High-Surface-Area Electrocatalysts Using a Rotating Disk Electrode Configuration. Journal of The Electrochemical Society, 145(7), pp. 2354-2358.

Schwanitz, B.; Rabis, Annett; Horisberger, Michael; Scherer, Gunther G; Schmidt, Thomas J, 2012. Sputtered Cathodes for Polymer Electrolyte Fuel Cells: Insights into Potentials, Challenges and Limitations. Chimia, 66(3), pp. 110-119.

Shao, Y., Yin, G. & Gao, Y., 2007. Understanding and approaches for the durability issues of Pt-based catalysts for PEM fuel cell. Journal of Power Sources, Volume 171, pp. 558-566.

Sharma, S. & Pollet, B. G., 2012. Support materials for PEMFC and DMFC electrocatalysts- A Review. Journal of Power Sources, pp. 96-119.

Shima, J. et al., 2001. Electrochemical characteristics of Pt–WO3/C and Pt–TiO2/C electrocatalysts in a polymer electrolyte fuel cell. Journal of Powder Sources, 102(1-2), pp. 172-177.

Slavcheva, E.; Ganske, G; Topalov, G; Mokwa, W; Schnakenberg, U, 2009. Effect of sputtering parameters on surface morphology and efficiency of thin platinum films.. Applied Surface Science, Volume 255, pp. 6479-6486.

Stevens, D. A., Hicks, M. T., Haugen, G. M. & Dahn, J. R., 2005. Ex Situ and In Situ Stability Studies of PEMFC Catalysts: Effect of Carbon Type and Humidification on Degradation of the Carbon. Journal of The Electrochemical Society, 152(12), pp. A2309-A2315.

Su, H., Zhang, B. & Chen, L., 2010. Preparation and Characterization of Platinum Supported on Carbon Nanotubes with Different Tube Diameter for Cathode Catalysts of Proton Exchange Membrane Fuel Cells. Journal of Mechanical Science and Technology, 26(6), pp. 529-534.

Tabet-Aoul, A. & Mohamedi, M., 2012. Interrelated functionalities of hierarchically CNT/CeO2/Pt nanostructured layers: synthesis, characterization, and electroactivity. Physical Chemistry Chemical Physics, Volume 14, pp. 4463-4474.

Tamura, T. & Kawakami, H., 2010. Aligned electrospun nanofiber composite membranes for fuel cell electrolytes. Nano Letters, Volume 10, pp. 1324-1328.

Tang, H., Qi, Z. G., Ramani, M. & Elter, J. F., 2006. PEM fuel cell cathode carbon corrosion due to the formation of air/fuel boundary at the anode.. Journal of Power Sources, 158(2), pp. 1306-1312.

Taniguchi, A., Akita, T., Yusuda, K. & Miyazaki, Y., 2004. Analysis of electrocatalyst degradation in PEMFC caused by cell reversal during fuel starvation. Journal of Power Sources, 130(1-2), pp. 42-49.

Teranishi, K., Kawata, K., Tsushima, S. & Hirai, S., 2006. Degradation Mechanism of PEMFC under Open Circuit Operation. Electrochemical and Solid-State Letters, 9(10), pp. A475-A477.

Thurier, C. & Doppelt, P., 2008. Platinum OMCVD processes and precursor chemistry. Coordination Chemistry Reviews , Volume 252, pp. 155-169.

U.S. DRIVE, 2013. Fue Cell Technical Team Roadmap, s.l.: U.S. Department of Energy.

Von Kraemer, Sophie; Wikander, Kjell; Lindbergh, Goran; Lundblad, Anders; Palmqvist, Anders E.C., 2008. Evaluation of TiO2 as catalyst support in Pt-TiO2/C composite cathodes for the proton exchange membrane fuel cell. Journal of Power Sources, Volume 180, pp. 185-190.

Wang, Xin; Li, Wenzhen; Chen, Zhongwei; Waje, Mahesh; Yan, Yushan, 2006. Durability investigation of carbon nanotube as catalyst support for proton exchange membrane fuel cell. Journal of Power Sources, Volume 158, pp. 154-159.

Wang, Y., Chen, W., Wang, B. & Zheng, Y., 2014. Ultrathin Ferroelectric Films: Growth, Characterisation, Physics and Application. Materials, Volume 7, pp. 6377-6485.

Wang, Y.-J., Wilkinson, D. P. & Zhang, J., 2011. Noncarbon Support Materials for Polymer Electrolyte Membrane Fuel Cell Electrocatalysts. Chemical Reviews, pp. 7625-7651.

Wani, T. A., Singh, P., Khan, A. S. & Mehra, M., 2010. A study of thermodynamic properties of transition metal diborides. Recent Research in Science and Technology, 2(5), pp. 107-113.

Wu, J. et al., 2008. A review of PEM fuel cell durability: Degradation mechanisms and mitigation strategies. Journal of Power Sources, Volume 184, pp. 104-119.

Xiong, L. & Manthiram, A., 2004. Synthesis and characterization of methanol tolerant Pt/TiOx/C nanocomposites for oxygen reduction in direct methanol fuel Cells. Electrochimica Acta, 49(24), pp. 4163-4170.

Xuyen, N. Thi; Kim, Tae Hyung ; Geng, Hong-Zhang; Lee, Il Ha ; Kim, Ki Kang ; Lee, Young Hee., 2009. Three-dimensional architecture of carbon nanotube-anchored polymer nanofiber composite. Journal of Materials Chemistry, Volume 19, pp. 7822-7825.

Yin, Shibin; Mua, Shichun; Lv, Haifeng; Cheng, Niancai; Pan, Mu; Fu, Zhengyi, 2010. A highly stable catalyst for PEM fuel cell based on durable titanium diboride support and polymer stabilization. Applied Catalysis B: Environmental, Volume 93, pp. 233-240.

Yu, X. & Ye, S., 2007. Recent advances in activity and durability enhancement of Pt/C catalytic cathode in PEMFC: Part II: Degradation mechanism and durability enhancement of carbon supported platinum catalyst. Journal of Power Sources, 172(1), pp. 145-154.

Zhang, J., 2008. PEM Fuel Cell Electrocatalysts and Catalyst Layers: Fundamentals and Applications. s.l.:Springer., pp 1-79, pp 355-372, pp 556-570

Zhang, P., Huang , . S.-Y. & Popov, B. N., 2010. Mesoporous Tin Oxide as an Oxidation-Resistant Catalyst Support for Proton Exchange Membrane Fuel Cells. Journal of Electrochemical Society, 157(8), pp. B1163-B1172.

Zhang, Shengsheng; Yuan, Xiaozi; Wang, Haijiang; Merida, Walter; Zhu, Hong; Shen, Jun; Wu, Shaohong; Zhang, Jiujun, 2009. A review of accelerated stress tests of MEA durability in PEM fuel cells. International Journal of Hydrogen Energy, Volume 34, pp. 388-404.

Zhang, W. & Pintauro, P. N., 2011. High Performance Nanofiber Fuel cell Electrodes. ChemSusChem, Volume 4, pp. 1753-1757.